Title
Small-Scale Mechanical Testing and Size Effects in Extreme Environments

Author
Prasitthipayong, Anya

Publication Date
2017

Peer reviewed|Thesis/dissertation

Small-Scale Mechanical Testing and Size Effects in Extreme Environments

By

Anya Prasitthipayong

A dissertation submitted in partial satisfaction of the

requirements for the degree of

Doctor of Philosophy

in

Engineering - Materials Science and Engineering

in the

Graduate Division

of the

University of California, Berkeley

Committee in charge:

Professor Andrew M. Minor, Chair
Professor Peter Hosemann
Professor Mark. D. Asta

Spring 2018

Small-Scale Mechanical Testing and Size Effects in Extreme Environments

Abstract

Small-Scale Mechanical Testing and Size Effects in Extreme Environments

By

Anya Prasitthipayong

Doctor of Philosophy in Engineering – Materials Science and Engineering

University of California, Berkeley

Professor Andrew M. Minor, Chair

Ion irradiation is often used to simulate the effects of neutron irradiation due to reduced activation of materials and vastly increased dose rates. Nonetheless, the low penetration depth of ions requires the development of small-scale mechanical testing techniques, such as nanoindentation and microcompression, in order to measure mechanical properties of the irradiated material. Nanoindentation is a widespread and useful method for evaluating mechanical properties at the sub-micron length scale. However, the Indentation Size Effect (ISE) where hardness increases with decreasing penetration depth remains a major obstacle to obtain meaningful macroscopic mechanical properties from small volume testing. *In situ* microcompression testing, although requires extensive sample preparation, has served as a novel small-scale testing tool for evaluating mechanical properties due to the capability to directly observe deformation mechanisms while probing well-defined volumes and producing real-time stress-strain curves. Nevertheless, Sample Size Effect (SSE), the commonly observed phenomenon where the strength of materials increases with decreasing sample size, has remained a remarkable drawback of this technique. Although ISE and SSE phenomena have been studied extensively at room temperature, the influence of temperature on both phenomena is currently not clear.

This work emphasizes the development of high temperature small-scale mechanical testing techniques and systematically addresses the independent influence of irradiation and temperature on ISE and SSE phenomena in an austenitic Fe-Cr-Ni alloy (800H) to establish the baseline for nanoindentation testing and microcompression testing for metal alloys, especially for ion-irradiated alloys in extreme environmental conditions. The 800H steel sample was irradiated with 70 MeV Fe^{9+} at 450 °C to the total dose of 20.68 dpa. Cross-sectional indents performed perpendicular to the irradiated edge confirms the SRIM calculation of 6.2 μm penetration depth. FIB-fabricated TEM foil containing the unirradiated and the irradiated areas of the sample suggests the validity of characterization studies of irradiated samples prepared by FIB procedures. All micromechanical tests were conducted up to 300 °C, which is well below the irradiation temperature, to quantify the effect of temperature on size effects without the influence of dislocation density.

EBSD was performed to search for two grains of known orientations large enough to contain all indents for ISE studies in both the unirradiated (<111> and <131>) and the irradiated (<111> and <113>) 800H at all temperatures. A <111> grain orientation was purposely chosen to be the same for direct comparisons before and after irradiation. An interesting observation is that grain orientation has a strong influence on indentation size effect. It was found that in all cases, the ISE is less pronounced at high temperatures due to the increase of the plastic zone size. For the same grain orientation, the indentation size effect is less pronounced in the irradiated 800H at all test temperatures.

In order to allow straightforward cross-comparisons between indentation and microcompression testing techniques, micro-pillars were fabricated in a <111> grain containing both the unirradiated and the irradiated volumes at room temperature and at 300 °C. *In situ* characteristics of the microcompression testing revealed the change in deformation mechanism during compression after irradiation. TEM lift-out of the compressed micro-pillars were fabricated for microstructural characterization. The influence of irradiation and temperature on sample size effect were independently investigated. The yield stress of micro-pillars increase with irradiation and with decreasing size. For the first time, the temperature dependence of sample size effect is observed in fcc metals. This implies that bulk strength rather than crystal structure determines the behavior of sample size effect at elevated temperatures.

In summary, this dissertation unravels the fundamentals behind indentation size effect and sample size effect at high temperatures and correlates microstructures with mechanical properties. It was discovered that mechanical testing methods determine how size effect behavior is influenced by temperature. Due to significantly less pronounced indentation size effect, high temperature nanoindentation has been proven to help bridge the gap between small-scale mechanical testing and bulk testing. The clear difference in the microstructures of the unirradiated and the irradiated regions in the FIB-manufactured TEM lift-out foil justifies FIB as a proper TEM preparation method. *In situ* microcompression and TEM lift-outs of the compressed micro-pillars demonstrate the change in deformation mechanisms resulting from ion irradiation.

Table of Contents

List of Figures

Figure 5.13 Bright field image (g = 200) of the room temperature compressed 2x2x4 μm irradiated micro-pillar.

List of Tables

Acknowledgements

I am extremely grateful to both of my advisors, Professor Andrew Minor and Professor Peter Hosemann. I could not have been where I am today without their continuous support and encouragement.

I would also like to thank the Minor group and the Hosemann group members who have supported me throughout my time as a PhD student.

This research was funded by DOE-NE Integrated Research Project (IRP). Work at the Molecular Foundry was supported by the Office of Science, Office of Basic Energy Sciences, of the U.S. Department of Energy under Contract No. DE-AC02-05CH11231. I would like to also acknowledge our collaborators, especially Anna Kareer for the CSM nanoindentation and Alistair Garner and Tamas Ungar for the the XRD experiments.

Last but not least, I am extremely grateful to my family. They have always been supportive and encouraging.

Chapter 1

Introduction and Background

1.1 Structural materials for nuclear applications and material selection

A major challenge in the deployment of Gen-IV nuclear reactor systems is the requirement for performance and reliability improvements of structural materials [1-7]. Gen-IV reactors are designed to operate at higher temperatures, higher neutron doses and generally more hostile environments than are experienced in current reactor systems [1-8]. Desirable characteristics of Gen-IV structural materials consist of exceptional stability against thermal creep, irradiation creep and void swelling [1-7]. In addition, resistance to irradiation hardening, embrittlement and irradiation assisted stress corrosion cracking (IASCC) is required [1-7]. Candidate structural materials for these advanced reactor designs include ferritic-martensitic steels, austenitic stainless steels and oxide dispersion strengthened (ODS) steels [7,9-11].

Ferritic-martensitic steels are being considered for Gen-IV designs due to their superior mechanical performance such as improved creep properties and irradiation resistance [12-16]. In addition, high chromium (Cr) ferritic-martensitic steels, such as T91, have high resistance to corrosion, oxidation, creep and void swelling [2,17]. However, long-term creep rupture at higher temperatures, irradiation embrittlement and radiation-induced segregation (RIS) remain a concern in ferritic-martensitic steels [18-22]. Austenitic stainless steels undergo considerable void swelling and radiation-induced segregation, limiting their performance as nuclear structural materials. However, they exhibit exceptional creep resistance and reasonable corrosion resistance [23-27]. Compared to ferritic-martensitic and austenitic stainless steels, ODS steels perform better at high temperatures due to their resistance to hardening, embrittlement and swelling [28-32]. It has been observed that small Y-rich nanoparticles impede dislocation motion and act as effective sinks for radiation-induced defects, and therefore allow better creep strength [2,33-37]. It is not the intention of this article to weigh one material over another and point towards each materials shortcoming but simply outline why there is a variety of materials being considered for Gen-IV reactors.

In this work, austenitic 800H, ferritic-martensitic T91, nanocrystalline T91 (NCT91) and ferritic oxide dispersion strengthened (ODS) 14YWT are being investigated. The alloy compositions are shown in Table 1.1. High Ni (>30wt%) austenitic steels, such as 800H, have been shown to inhibit swelling and enhance void formation resistance due to the presence of fine precipitates [38-39]. This alloy also exhibits favorable high temperature creep properties and resistance to oxidation and therefore shows promise as a candidate structural material for Gen IV reactors. 800H alloy has a coarse-grained structure with an average grain size of 204.4 μm with a standard deviation of 87.1 μm. The large grain characteristic leads to high creep resistance. The T91 alloy was selected as a candidate material due to its promising mechanical properties and resistance to stress corrosion cracking in a super critical water environment in fossil plants [40-41]. T91 has been cold rolled and has an average grain size of 6.1 μm with a standard deviation of 4.4 μm. Since significant reduction of defect clusters was shown to correlate with grain size [42-43], nanocrystalline T91

(NCT91) was also chosen to investigate grain size effects on the irradiation tolerance of T91. The NCT91 was obtained through the equal channel angular pressing (ECAP) process. The grain size after the ECAP process is approximately 320 nm [43]. Lastly, the nano-structured characteristics and sub-micron grain size (approximately 560 nm with a large standard deviation of 410 nm) of 14YWT makes it a candidate ODS alloy for Gen-IV reactors [28-32,44]. 14YWT has excellent high temperature creep properties and the Y-rich nanoparticles act as sinks to irradiation-induced defects and transmutation gases, giving 14YWT a high radiation resistance [34-38,45].

Table 1.1 Compositions of the four alloys of interest

800H		T91, NCT91		14YWT	
Element	G. O. Carlson (wt%)	Element	PNNL (wt%)	Element	ORNL (wt%)
Fe	45.53	Fe	89.52	Fe	82.5
Ni	31.59	Cr	8.6	Cr	14.3
Cr	20.42	Mo	0.89	W	2.32
Mn	0.76	Mn	0.37	Ti	0.27
Al	0.50	V	0.21	Y	0.19
Ti	0.57	Ni	0.09	O	0.177
Others	0.63	Others	0.32	Others	0.243

Measurements courtesy of PNNL (Pacific Northwest National Laboratory) and ORNL (Oak Ridge National Laboratory), collaborations of the NEUP-IRP project.

1.2 Small-scale mechanical testing

Studying the effect of neutron irradiation on potential candidate materials for Gen-IV nuclear reactors requires significant infrastructure and leads to costly PIE (Post Irradiation Examination) due to high levels of residual activity. Moreover, neutron irradiations require long timescales to simulate high doses, where ion irradiations can achieve the same dose in significantly less time. The use of ion irradiation therefore significantly reduces the time and cost required to reach the high levels of damage required of Gen IV reactor materials. Ion irradiation has previously been used to study radiation damage in austenitic stainless steels [46-54] and may be used in the future as a surrogate method. Although extremely careful control of experimental conditions and understanding of damage-rate differences is required in order to emulate the complex microstructural changes occurring under neutron irradiation [55].

Due to the low penetration depth of ion irradiations, small-scale mechanical testing is essential for examining the properties of ion-irradiated materials [55-61]. The nanoindentation technique has been widely used to assess hardness and elastic modulus utilizing the Oliver-Pharr method [62]. Nanoindentation is a very attractive method due to relatively little sample preparation and high throughput. However, the drawback of the method is the complicated data analysis due to the triaxial stress state. *In situ* microcompression testing of micron-size pillars requires extensive sample preparation using an SEM-FIB (Dual-beam) instrument. However, *in situ* microcompression testing has made qualitative and quantitative studies of mechanical properties possible [63]. Stress-strain curves and direct observations of the deformation mechanisms are key advantages of this small-scale testing method.

1.2.1 Nanoindentation

Nanoindentation methodology

Quasi-static (QS) and dynamic are the two main nanoindentation methods. In the conventional quasi-static nanoindentation testing, the load is increased over time, and the loading cycle measured generates one data point per indent (from which various mechanical properties can be calculated). Figure 1.1 (a) illustrates a sample force versus displacement curve obtained from the conventional QS test. In dynamic nanoindentation, such as the Continuous Stiffness Measurement (CSM) test, the load is increased over time with a small oscillating force (see Figure 1.1 (b). Due to the separation of the in-phase and out-of-phase components of the load vs. displacement data, the unloading cycles become unnecessary [64]. Therefore, many data points per indent can be obtained at different indentation depths.

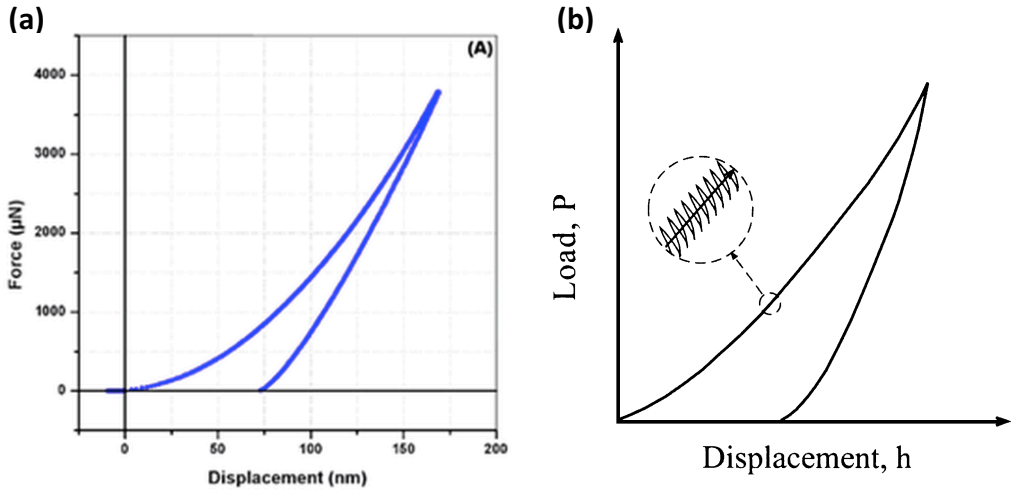

Figure 1.1 Examples of the Force or Load vs. displacement curve for (a) quasi- static method (QS) [65] and (b) dynamic method (CSM) [64].

Nanoindentation data analysis

Despite the conveniently obtained hardness and modulus data from software used in commercially available indenters, it is valuable to understand the fundamentals behind these reported values. The Oliver-Pharr method was originally developed for sharp, geometrically self-similar indenters such as a Berkovich tip [66]. It is the most widely used method to extract measurement data from nanoindentation testing. In this method, the load-displacement data obtained during an indentation (loading and unloading cycle) is used to calculate hardness and modulus of a material. A typical data set (shown in Figure 1.2 (a)) needed for the calculation includes maximum load P_{max}, maximum displacement h_{max}, elastic unloading stiffness S. The stiffness is referred to the contact stiffness, which is essentially the slope of the initial unloading curve. The major assumption is that deformation during unloading is purely elastic, i.e., plastic deformation is irreversible. The final depth h_f is the depth after unloading is complete. Hardness is a plastic property of a material of interest that can be calculated by Equation 1.1 where A is the contact area under load, which is a

function of contact depth h_c calculated and defined by Equation 1.2 and Figure 1.2 (b), respectively.

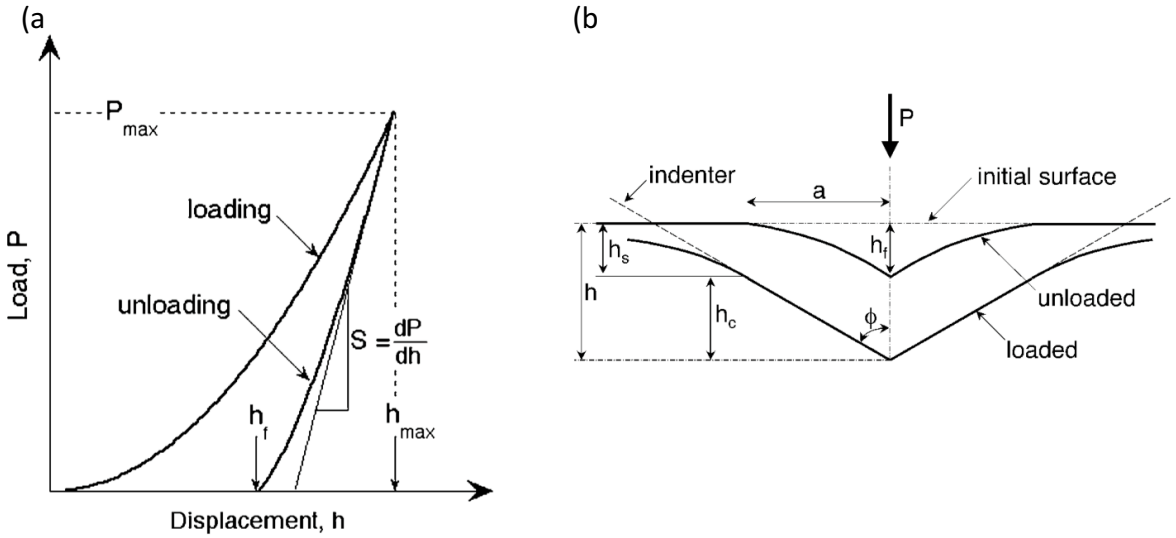

Figure 1.2 (a) Schematic of a typical indentation load–displacement curve (b) Schematic of the indentation unloading showing the origin of the sink-in h_s [62]

$$H = \frac{P_{max}}{A} \quad \text{(Eqn. 1.1)}$$

H = hardness, P_{max} = maximum load, A = contact area

$$h_c = h_{max} - \epsilon \frac{P_{max}}{S} \quad \text{(Eqn. 1.2)}$$

h_c = contact depth, h_{max} = maximum depth, ϵ = geometrical constant, S = elastic unloading stiffness

The normally reported modulus data are referred to the effective elastic modulus or the reduced modulus, which is a combination of the actual modulus of an indented material and the modulus of the indenter (see Equation 1.3). The effective modulus can be calculated using the stiffness and the contact area (see Equation 1.4).

$$\frac{1}{E_{eff}} = \frac{1-\upsilon^2}{E} + \frac{1-\upsilon_i{}^2}{E_i} \quad \text{(Eqn. 1.3)}$$

E_{eff} = effective elastic modulus, υ and E = Poisson's ratio and Young's modulus of the sample, υ_i and E_i = Poisson's ratio and Young's modulus of the indenter

$$S = \beta \frac{2}{\sqrt{\pi}} E_{eff} \sqrt{A} \quad \text{(Eqn. 1.4)}$$

β = geometrical constant

It is worth mentioning that the method for calculating hardness and modulus measurements discussed so far is only accurate when pile-ups are negligible. Corrections to the model are essential when considerable pile-ups are evident [66].

Nanoindentation testing of ion-irradiated materials

The nanoindentation technique has been commonly used to measure radiation damage and mechanical property evolution due to ion irradiation. However, depending on irradiation conditions and resulting depths of irradiated layers, there are multiple issues associated with performing nanoindentation testing on ion-irradiated materials such as the dose profile, indentation size effect and implantation and surface effects [58]. These issues unfortunately lead to complication in the data analysis. Figure 1.3 provides schematics of two major experimental geometries for performing nanoindentation testing on ion-irradiated materials: surface (on the irradiated surface where the beam hits the sample) and cross-section (perpendicular to the irradiated surface) indentation [59]. Nanoindentation measurements obtained from surface indentation experience surface effects and sample an inhomogeneously wide dose range. The wide dose range is further accentuated by the fact that the material sampled during nanoindentation testing is not the indentation depth but is rather the plastic zone size where the strain is sufficient for plastic deformation to be initiated (typically five to ten times the indentation depth, depending on the material of interest [67-69]). This also suggests that careful considerations be made since performing surface indentation can possible sample the unirradiated matrix underneath the irradiated layer, although a model to resolve this issue has been established in Ref. 58.

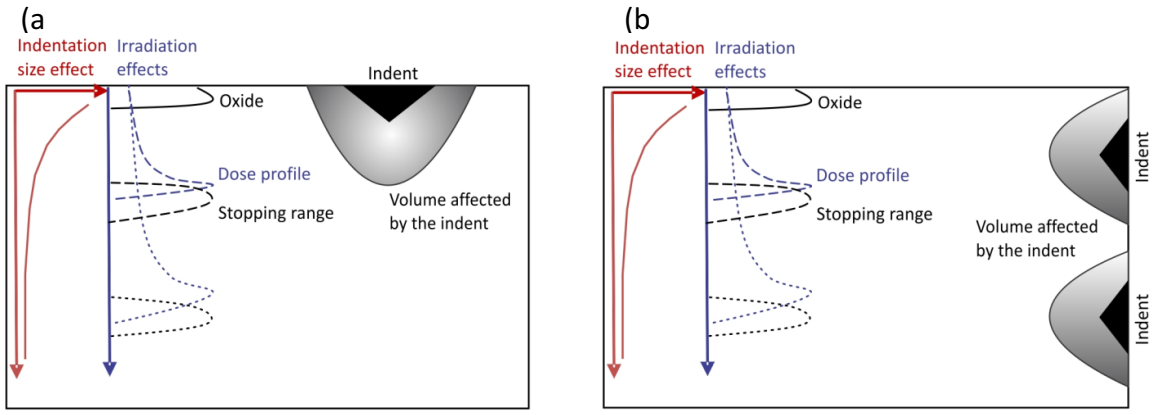

Figure 1.3. Schematic of experimental geometries during micromechanical testing for shallow (dashed line) and deep (dotted line) ion-beam- irradiated samples. (a) Surface indentation (b) Cross-section indentation [59]

It is thus generally recommended that cross-section indentation be carried out when absolute mechanical property measurements cannot be negotiated. However, due to the low penetration depths of ion irradiations, especially heavy-ion irradiations, it is sometimes difficult to avoid surface nanoindentation in studies where multiple indents are needed or specific grains are of interest. Indentation size effects are observed in both the surface and the cross-section indentation tests. Therefore, when comparing mechanical property data obtained from nanoindentation, it is necessary that the indentation depth be the same in the case where indentation size effects exist.

1.2.2 *In situ* microcompression

In situ microcompression methodology

Following the development of small-scale mechanical testing of FIB-manufactured samples with dimensions in the micrometer regime by Uchic et al. [63,70], the *in situ* characteristic and relatively uncomplicated data evaluation have allowed microcompression testing to play an immense role in the small-scale mechanical testing field. The visual control of microcompression testing experiments reduces alignment issues and allows direct observations of deformation mechanisms during testing. Figure 1.4 shows the schematic of a typical *in situ* microcompression test [71] where diamond flat punch is an indenter similar to what has been shown in nanoindentation.

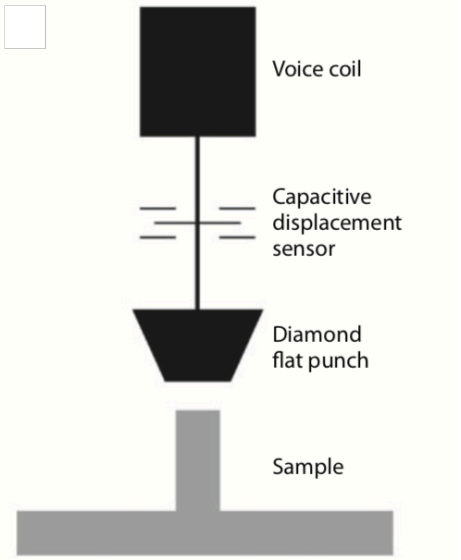

Figure 1.4 Schematic of a typical *in situ* microcompression test [71]

The most significant difference from bulk testing is that in *in situ* microcompression testing, micro-pillars are attached to the bulk substrate and therefore are not freestanding [71]. Careful considerations are essential when preparing micro-pillars for *in situ* microcompression testing. To suppress buckling deformation mode and provide sufficient accuracy, 2:1 to 3:1 aspect ratio should be considered when fabricating micro-pillars [&]. This helps reduce tapering effect which can cause nonuniform stress distribution throughout micro-pillars [71]. Moreover, micro-pillars with the aforementioned aspect ratio are not strongly affected by the fact that the seemingly uniaxial testing may in fact be in a triaxial stress state due to the bottom of micro-pillars being constrained [71].

Due to the ability to precisely control the location and size of micro-pillars and the ease of manipulation, FIB-SEM Dual-Beam has been most commonly utilized to manufacture micro-pillars [55,63,72]. Despite the advantages, there are two main drawbacks of using FIB-SEM Dual-Beam to manufacture micro-pillars. First, FIB-fabricated micro-pillars experience Ga^{+} ion

bombarding and deposition, resulting in an irradiation-damage layer covering the micro-pillars. Fortunately, this damage layer is negligible because studies have shown that the layer does not considerably strengthen micro-pillars [73-74]. Second, FIB-fabrication is a costly and time-consuming sample preparation method. Minor misalignments do not appreciably affect the yield strength measurements since surface interactions during initial contact can be taken into considerations when performing data analysis. However, misalignments can underestimate the elastic modulus measurements [75].

Microcompression testing of ion-irradiated materials

In the same manner as nanoindentation, *in situ* microcompression can be performed on the micro-pillars fabricated on the surface where the ion beam hits the sample and on the cross-section perpendicular to the irradiated surface (see Figure 1.5). Similar to surface indentation, micro-pillars manufactured on the surface experience an inhomogeneous dose profile along the length of the micro-pillars. This issue can be alleviated by fabricating micro-pillars in the cross-section manner. Since the top of micro-pillars need to be cleaned, it can be assumed that surface effects in the micro-pillars fabricated on the irradiated surface such as an oxide layer and irradiation surfactants are eliminated during the fabrication processes. Similar to indentation size effect, in the micrometer regime, sample size effect (especially in metals) is unavoidably present in both surface and cross-section *in situ* microcompression testing, emphasizing the need to compare the strengths of micro-pillars of the same dimensions.

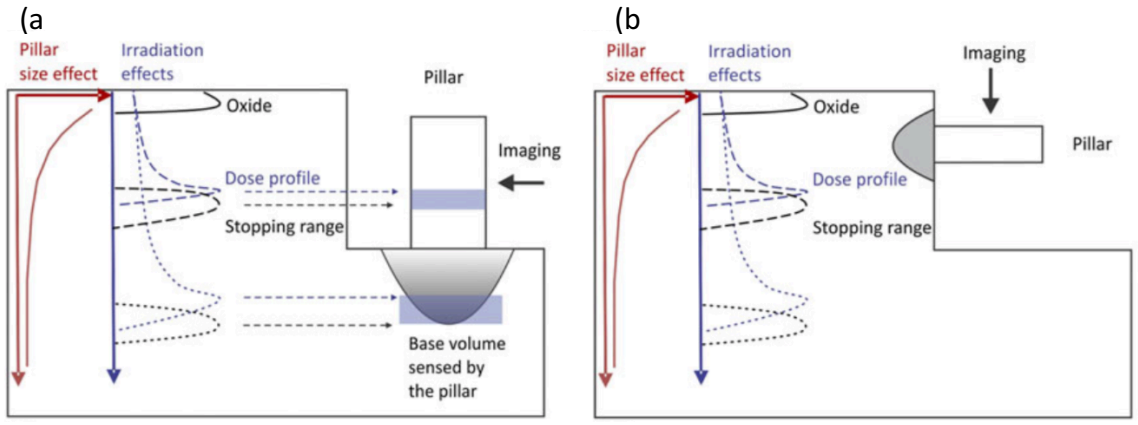

Figure 1.5 Schematic of experimental geometries during micromechanical testing for shallow (dashed line) and deep (dotted line) ion-beam- irradiated samples (a) Conventional microcompression (b) Cross-section microcompression [59]

1.3 Mechanical Size Effects

1.3.1 Indentation Size Effect (ISE)

The phenomenon known as the Indentation size effect (ISE) describes the common observation that hardness changes with the depth of indentation. This phenomenon is observed in a wide range of materials where hardness obtained from geometrically self-similar indenters increases with

decreasing penetration depth, especially in the shallow penetration depth ranges [59,76-85]. Some of the indentation size effect observed in indentation of single crystalline and polycrystalline Cu and single crystalline Ag are shown in Figure 1.6 [86]. The first and most widely used model for ISE developed by Nix and Gao (Equation 1.5) [87] is based on the concept of strain gradient plasticity [88-89] and geometrically necessary dislocations (GNDs), which are the dislocations required in excess of statistically stored dislocations (SSDs) to accommodate the material displaced by the indenter after indentation [90]. Due to the higher density of GNDs required in addition to the available SSDs for a permanent change in shape due to indentation, ISE is observed at small indentation depths where a lower density of SSDs is available [90-91]. To illustrate, SSDs refer to the existing dislocations in the material. Therefore, while the actual number of SSDs decreases with indentation depths, which scales with plastically deformed volume resulted from indentation, the density of SSDs is depth independent. The principal assumption and the major shortcoming of this model is that the radius of the hemispherical volume containing the GNDs is taken to be equal to contact radius of the indenter.

$$\frac{H}{H_0} = \sqrt{1 + \frac{h^*}{h}} \qquad \text{(Eqn. 1.5)}$$

H = hardness at indentation depth h, H_0 = hardness at infinite depth or bulk hardness, h^* = characteristic depth,

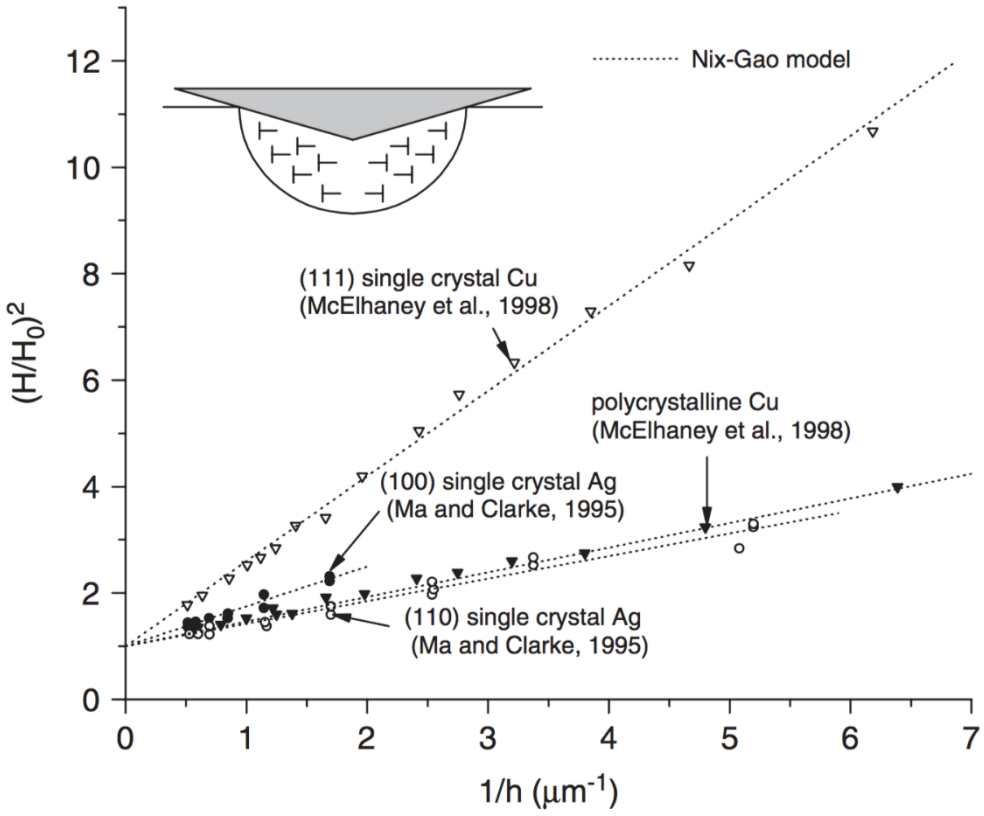

Figure 1.6 Nanoindentation hardness data for single crystal and polycrystalline copper and single crystal silver [86]

Durst et al. [92-93] proposed a correction to the Nix and Gao model by redefining the storage volume for the GNDs i.e. the plastically deformed volume underneath the indenter is considered instead of the volume given by the indenter contact radius. This approach contemplates that the GNDs reside within a plastic zone experiencing approximately 1.5% strain. The radius of the plastic zone size $a_{pz} \approx f\, a_c$ where f is the scaling factor and a_c is the contact radius of the indenter. The GNDs provide the extra hardening element that increases with decreasing size of the contact impression or depth of penetration. The density of GNDs is inversely proportional to the indentation depth, as other parameters are constant for a given indentation system (Equation 1.6), giving rise to the ISE. The characteristic length scale or characteristic depth h^*, which scales with the ISE, can be calculated from Equation 1.7. Figure 1.7 shows a schematic of the correction to the Nix and Gao model proposed by Durst et al [92].

$$\rho_{GND} = \frac{3}{2}\frac{1}{f^3}\frac{tan^2\theta}{bh} \qquad \text{(Eqn. 1.6)}$$

θ = angle between the indenter and the undeformed sample surface, b = burgers vector

$$h^* = \frac{81}{2}\frac{1}{f^3} b\alpha^2 tan^2\theta \left(\frac{G}{H_0}\right)^2 \qquad \text{(Eqn. 1.7)}$$

α = geometrical constant, G = shear modulus

$$H_0 = 3\sqrt{3}\alpha G b\sqrt{\rho_s} \qquad \text{(Eqn.1.8)}$$

ρ_s = density of SSDs

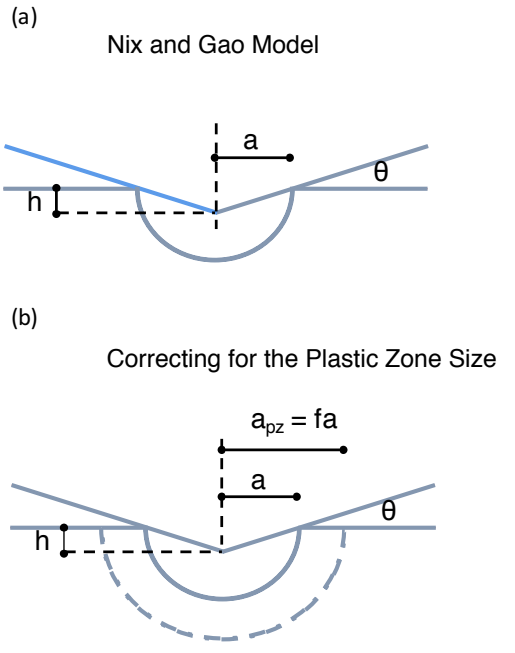

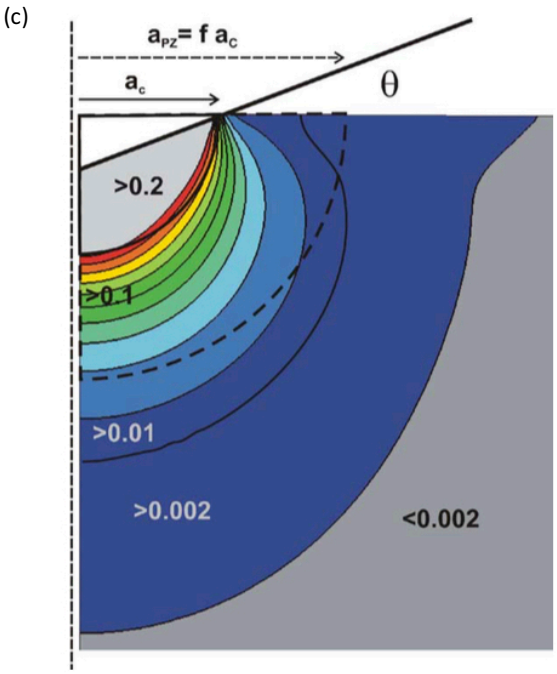

Figure 1.7 (a) Schematic of Nix and Gao model (b) Schematic of the correction to the Nix and Gao model proposed by Durst et al. (c) Schematic of the corrected Nix and Gao model showing plastic zone size and strain gradient under the indent [92]

While ISE has been studied extensively at room temperature, to date there has only been one study by Franke et al. [94] on ISE at elevated temperatures. Franke's study, performing a series of experiments on single crystal Cu of unknown orientation from ambient temperature up to 200 °C, revealed that size effect reduced considerably with increasing temperature owing to the decrease in the intrinsic plasticity length scale. Understanding the origins and the fundamentals of ISE behaviors at high temperatures can have an immense impact not only on high temperature nanomaterials and small-scale applications, but also on the improvement of the reliability of structural components used in nuclear applications occurring at high temperatures. Undoubtedly, this raises the question if the ISE changes with radiation damage, and if so how much. As Nix and Gao pointed out, cold worked material shows less of a size effect. Hosemann et al. argued that radiation damage will have the same effect [95]. However, systematic studies considering the effect of radiation damage on the ISE are rare and non-existent as a function of temperature which is what is of most interest since most nuclear related structures are not at ambient temperature in service.

1.3.2 Sample Size Effect (SSE)

Despite the advantages of *in situ* microcompression testing technique, "Sample Size Effect (SSE)" or the "smaller is stronger" phenomenon has revealed higher yield strength or critical resolved shear stress τ_{CRSS} with decreasing sample dimensions where the dimensions of the micro-pillars are of the same length scale as the microstructural features of the materials. Sample size effect in room temperature microcompression testing in BCC [96-106] and FCC [63,70,107-113] metals have been commonly observed, and the fundamentals behind the sample size effect phenomenon has been thoroughly studied. Figure 1.8 shows a normalized plot of strength as a function of dimension for microcompression testing obtained from various fcc metals where higher strengths are observed in sample of smaller dimensions [114].

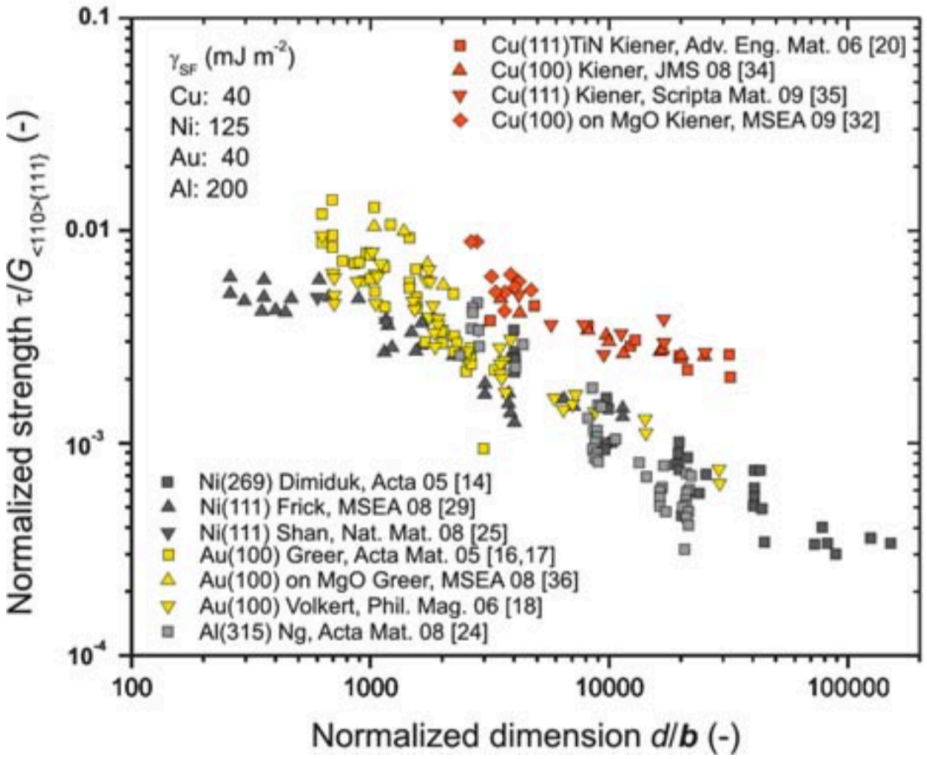

Figure 1.8 Normalized plot of strength as a function of dimension for microcompression testing obtained from various fcc metals [114]

In microcompression testing where the dimensions of micro-pillars are of the same order of magnitude as the source length, the double-ended Frank-Read sources become single-ended (one end pinned) due to the interactions with free surfaces of the finite samples [115]. The stress to operate such truncated sources takes the same form as that of double-ended Frank-Read sources (Equation 1.8), which contributes to the critical resolved shear stress (τ_{CRSS}) to initiate plastic deformation in micro-pillars (Equation 1.9), i.e. the stress required for the first percolation of a dislocation across the sample [115-116]. Equation 1.9 illustrates the different stresses that constitute the τ_{CRSS} of the micro-pillars, including the stress required to operate the weakest single-ended source $\frac{\alpha Gb}{L}$, the lattice resistance or the friction stress τ_0 and the stress from the dislocation forest hardening $0.5Gb\sqrt{\rho_{tot}}$. These stresses can be categorized as size-dependent and size-independent. The only size-dependent term is the stress to operate the weakest source due to the reverse relationship between the stress and the source length (i.e. sample dimension), giving rise to the sample size effect phenomenon. Figure 1.9 shows a schematic of size-dependent single-ended source activation [115].

$$\tau \propto \frac{Gb}{L} \qquad \text{(Eqn. 1.8)}$$

where τ is shear stress, G is shear modulus, b is the Burgers vector and L is the source length related to dislocation spacing or sample size

$$\tau_{CRSS} = \frac{\alpha G b}{L} + \tau_0 + 0.5 G b \sqrt{\rho_{tot}} \qquad \text{(Eqn. 1.9)}$$

where τ_{CRSS} is the critical resolved shear stress, α is a geometrical constant, G is shear modulus, b is the Burgers vector and L is dislocation spacing or source length related to dislocation spacing or sample size in the case where sample dimensions are of the same length scale as dislocation spacing, τ_0 is the friction stress and ρ_{tot} is the total dislocation density.

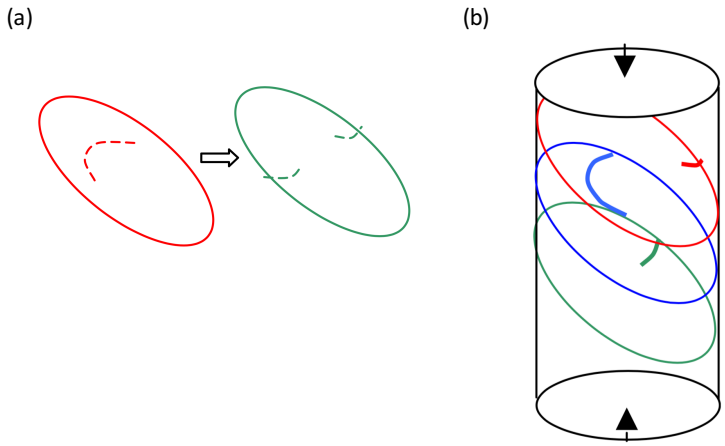

Figure 1.9 Schematic of size-dependent single-ended source activation [115]

Chapter 2

Technique Development and Comparisons

2.1 Experimental

After ion-beam irradiation, nanoindentation and *in situ* SEM uniaxial compression techniques are applied to measure the mechanical properties of T91, NCT91, 800H, and 14 YWT before and after irradiation to assess the effect of irradiation on mechanical properties. Microstructural parameters are extracted from X-ray diffraction profiles on T91, NCT91 and 14 YWT both before and after irradiation to link the observed changes in mechanical properties to microstructural evolution during irradiation.

2.2.1 Ion-beam irradiation

The alloys were sectioned into 3.5−4 mm x 3.5−4 mm-sized samples using a linear precision saw (See Figure 2.1). Note that the cross section of the T91 sample is perpendicular to the rolling direction. They were subsequently ground and polished using SiC grinding papers with water as a lubricant down to 1200 grit, followed by polishing with diamond solution down to 0.1 μm. The samples were then mounted onto the irradiation holder as depicted in Figure 2.2 (a). A gold (Au) foil was added between the samples and the mount to ensure good thermal contact. Figure 2.2 (b) illustrates a clear gap between the sample holder and the sample holder cover plate, ensuring good mounting and good mechanical contact.

The high energy ion irradiation was conducted at the Center for Accelerator Mass Spectrometry (CAMS) at Lawrence Livermore National Laboratory. The four alloys were irradiated with a rastered beam of 70 MeV Fe^{9+} bombarding ions, at 452 °C to a total dose of 20.68 displacement per atom (dpa). The dose was calculated at the depth where 5% of the peak implantation occurred. The average current was 19.47 nC/s. The irradiation process was completed in 15.55 hours while the temperature was monitored using an IR camera and a thermocouple mounted behind the sample. The beam current and profile were measured using an array of micro faraday cups. The damage layer was predicted to extend approximately 6.2 μm into the samples, according to the SRIM calculations shown in Figure 2.3. The version of the SRIM used was SRIM-2013 version in the modified Kinchin-Pease model. E_d (displacement energy) of 40 eV was used. The ion flux was 10^{15} ions/cm^2. After the irradiation experiment, each sample was sectioned into two half pieces using a low speed diamond saw (schematic provided in Figure 2.4). Surface nanoindentation and size effect studies were conducted on one half of the sample, while the other half was used for cross sectional analyses, which encompassed cross-section nanoindentation and *in situ* micro-pillars compression testing. Figure 2.5 shows a schematic of the cross section of the sample.

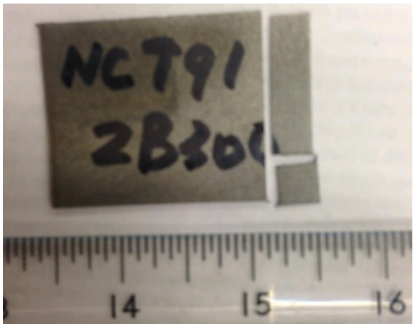

Figure 2.1. Cut sheet of a sample NCT91 representing the cutting scheme of the specimens provided. The small 4 x 4 mm piece is for the high energy ion beam irradiation and the larger strip for shear punch testing while the remaining materials will be reference for further irradiation and small scale mechanical tests.

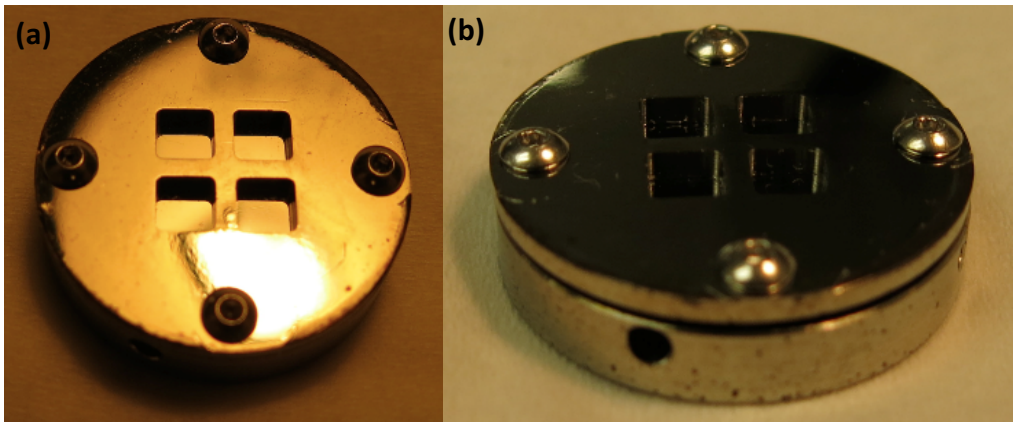

Figure 2.2. (a) Four alloys mounted in the 800H mount. (b) A clear gap exists between the sample holder and the sample holder cover plate, ensuring good mechanical contact.

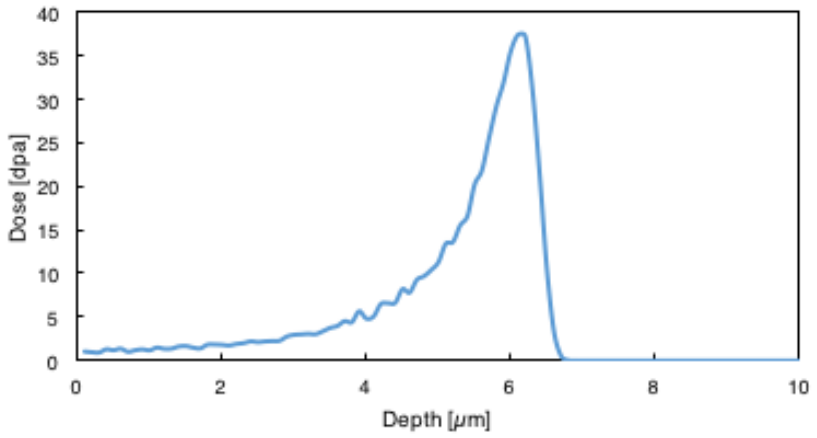

Figure 2.3 SRIM calculation of ion irradiation using 70 MeV Fe ions projectiles and Fe as target

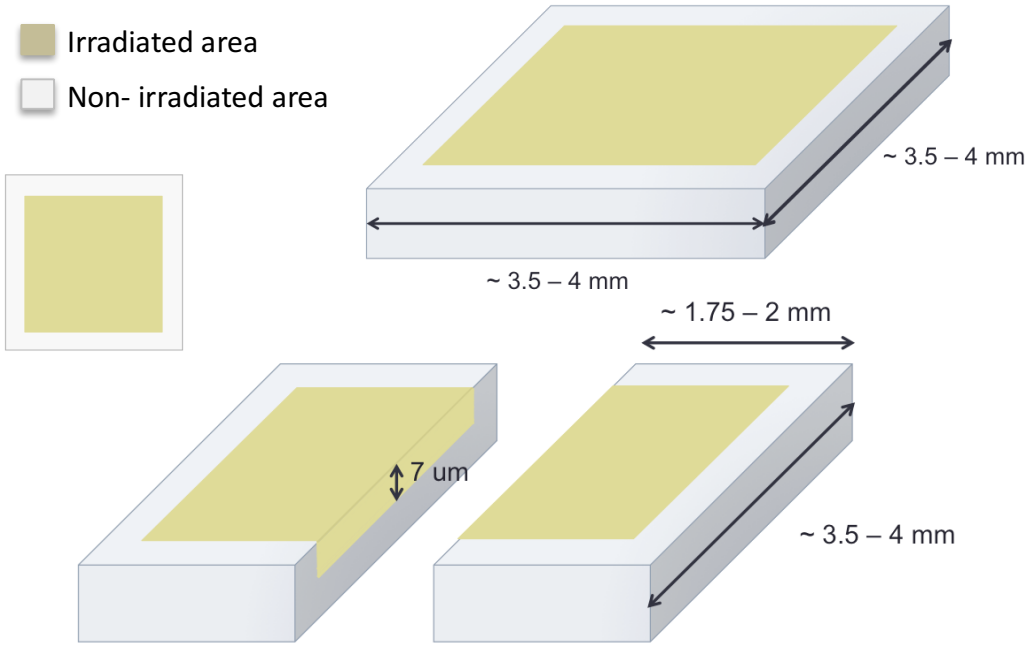

Figure 2.4 Schematic and dimensions of the ion-beam irradiated samples before and after sectioning.

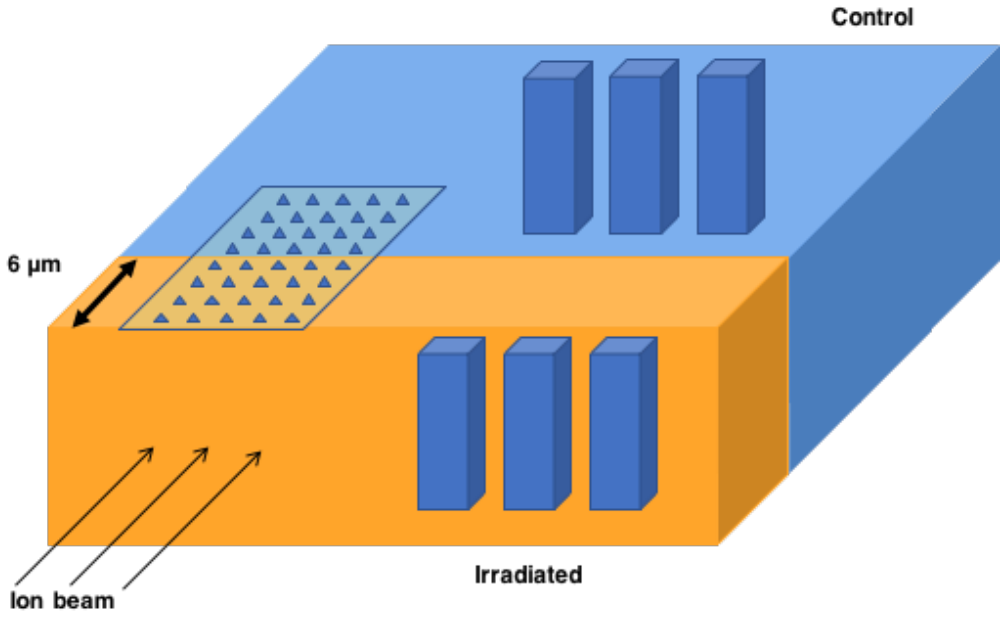

Figure 2.5 Schematic of the cross section of the sample showing variation of mechanical testing conditions (Figure not drawn to scale).

2.2.2 Sample preparation and specimen fabrication

The areas of indentation are shown schematically in Figure 2.6. With the obtained nanoindentation data, indentation size effect studies were performed on the surface samples before and after irradiation. Each of the four irradiated samples was mounted in slots cut in the triangle mount made of 303SS (Figure 2.7). Stainless steel thin foils were mounted next to the samples to prevent edge rounding, thereby allowing for pillar fabrication near the sample corner and ensuring uniform indents. The same grinding and polishing procedures mentioned previously were applied to achieve ideal surfaces for nanoindentation measurements. Proper surface preparation is very important for nanoindentation testing, as inappropriate surfaces can result in measurement errors [117-118].

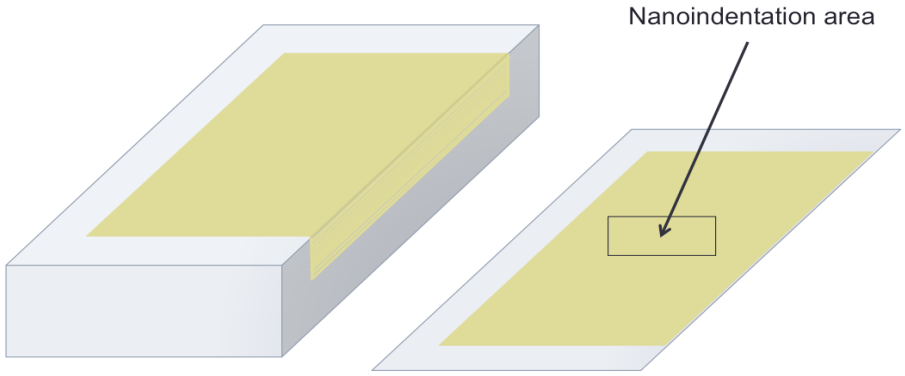

Figure 2.6. Schematic area of surface nanoindentation.

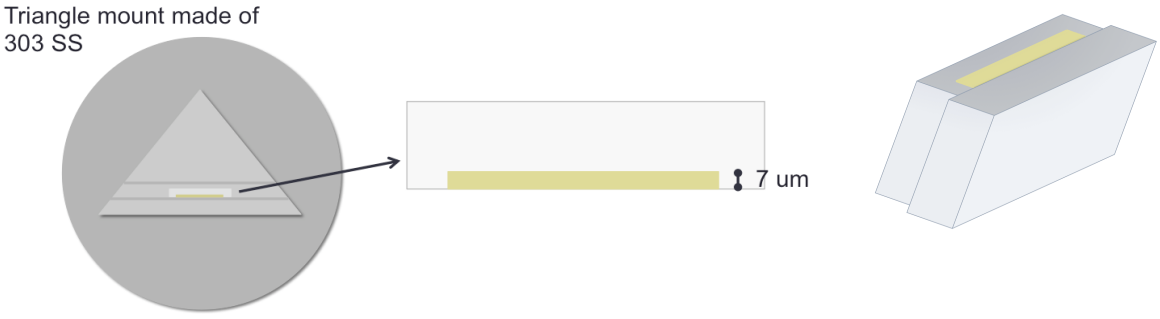

Figure 2.7. Schematic of the irradiated sample mounted in slots cut in the triangle mount made of 303SS.

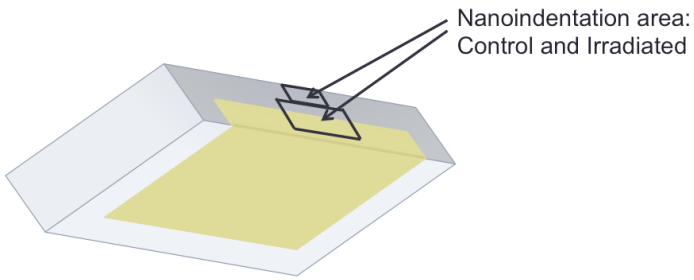

Figure 2.8. Schematic area of cross-section nanoindentation

2.2.3 Surface and cross-section nanoindentation

Quasi-static and Continuous stiffness measurement nanoindentation measurements were performed at the MML at UCB Figure 2.9 and the Agilent nanoindenter at University of Oxford (Figure 2.10), respectively. Quasi-static (QS) Nanoindentation was performed using a Micro Materials (MML) indenter under depth control mode. The standard Berkovich tip was calibrated using fused silica resulting in an area function for the particular tip used. The measured data (i.e. the hardness and the reduced modulus) were analyzed using the Oliver-Pharr method [62]. The indents were performed prior to ion irradiation and after irradiation, covering the depth range from 10 nm to 1000 nm. A separation distance of 5-10 μm was used between the indents ensuring no plastic zone interactions. With the obtained nanoindentation data, indentation size effect studies were performed on the surface samples before and after irradiation.

The continuous stiffness measurement (CSM) technique for nanoindentation was also used in this study. These experiments were carried out using a Keysight (formerly Agilent) G200 nanoindenter. In CSM indentation, an oscillating sinusoidal force is imposed on the nominally increasing loading segment of the indentation cycle. This allows the contact stiffness, and therefore the indentation hardness and modulus, to be measured as a function of indenter displacement continuously throughout the loading segment of the indentation. Arrays consisting of 25 indentations were made in both the irradiated and the unirradiated regions of the sample; all indentations were conducted in displacement control mode to a maximum displacement of 2 μm with a displacement rate of 10 nm/sec. Indents were positioned 50 μm apart to ensure that the plastic zones beneath the surface did not interact. The CSM conditions used were a frequency of 45Hz and an amplitude of 1nm.

Each of the four irradiated samples was mounted next to stainless steel thin foils to prevent edge rounding thereby ensuring symmetric indents and a flat irradiated area. The same grinding and polishing procedures mentioned previously were applied to achieve deformation-free surfaces for nanoindentation. A series of indentation measurements were performed on the irradiated cross-section samples in order to analyze the hardness change as a function of depth from the sample surface. Indents on the non-irradiated edge were also conducted for a direct comparison. All indents were performed under depth-controlled mode at a depth of 200 nm. The indents were also spaced approximately 5-10 μm apart to prevent plastic zone interactions.

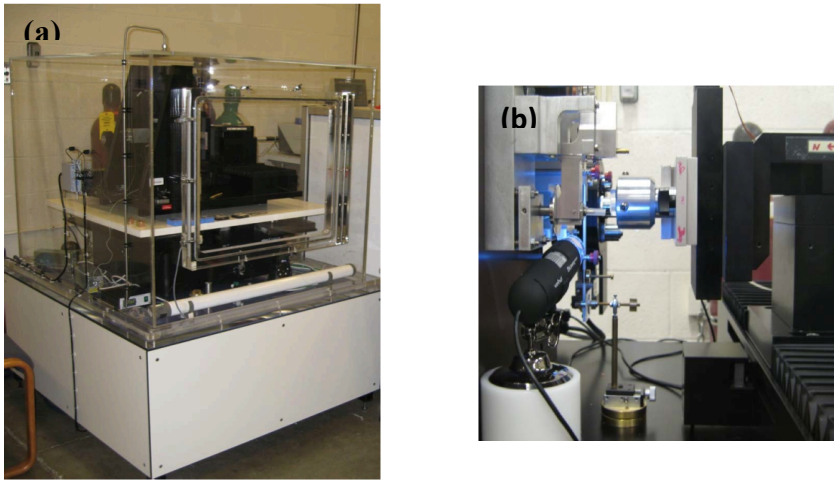

Figure 2.9 Micro Materials Nanoindenter at UCB (quasi-static nanoindentation). (a) Environmental shield ensures inert environment. (b) Sample-tip arrangement.

Figure 2.10 Schematic photograph of a G200 Agilent Nanoindenter similar to the one used at the University of Oxford for dynamic nanoindentation (CSM).

2.2.4 Micro-pillars fabrication and *in situ* microcompression

An FEI Quanta dual beam scanning electron microscope and focused ion beam (FIB-SEM) was used to fabricate pillars with the dimensions of either 3 μm x 3 μm x 6 μm (T91 and NCT91) or 2 μm x 2 μm x 4 μm (14YWT and 800H). Six pillars were fabricated in each of the cross-section samples with three pillars in the irradiated area and three pillars in the non-irradiated area. For the 800H alloy, with relatively large grain size, Electron Backscattered Diffraction (EBSD) was used to identify large grains for pillar locations. A large grain containing both the unirradiated and the irradiated material was selected for pillar fabrication in order to allow direct comparisons between the control and the irradiated pillars within the same grain. *In situ* uniaxial compression was performed utilizing a Hysitron PI-85 pico-indenter on the SEM-FIB fabricated pillars (see Figure 2.11) in the depth-controlled mode at the displacement rate of 10 nm/s using an indenter with a flat tip to obtain stress-strain curves for yield stress calculations [55].

(a) (b)

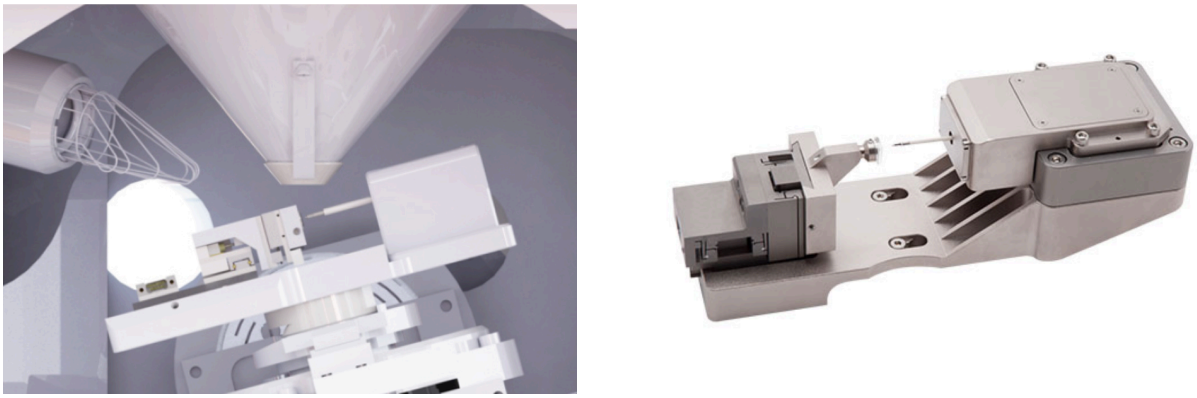

Figure 2.11 (a) Sample stage positon inside the FIB-SEM Dual-Beam chamber (b) Sample-tip configuration of the PI-85 indenter [119].

2.2.5 X-Ray diffraction

X-ray diffraction measurements were carried out on the same irradiated samples used for the micro-mechanical tests using a special high-resolution double-crystal diffractometer dedicated to line-profile-analysis [120]. The incident angle was fixed at 20° on a stationary specimen. The detection depth of $CoK_{\alpha 1}$ radiation at this angle is ~ 4 μm, and so the detected X-rays originate from the relatively flat region of the damage profile in Figure 2.3. The diffractometer was operated with a sealed Co X-ray tube of 0.4×8 mm^2 fine line-focus running at 30 kV and 35 mA with a wavelength of λ=0.1789 nm. The primary beam was monochromatised by a plane Ge monochromator using the (220) reflection. A slit of ~0.2 mm was inserted before the monochromator in order to select the $CoK_{\alpha 1}$ line and to remove the $CoK_{\alpha 2}$ contribution. The incident X-ray beam was positioned on the specimen surface using a low depth-resolution microscope and was observed to illuminate an area of ~ 0.2×1.0 mm on the specimen surface. The scattered X-rays were detected by two imaging plate (IP) detectors with a linear spatial resolution of 50 μm. The IPs were placed at the distance of 193 mm from the specimen covering an angular range of $25° < 2\theta < 170^{o}$. The diffraction patterns were obtained by integrating the intensity distributions along the corresponding Debye-Scherrer arcs on the IPs and are shown in Figure 2.12 Due to the plane Ge monochromator equipped with a 0.2 mm slit at a distance of ~150 mm from the X-ray source, the instrumental broadening effect of this setup was negligible [120], and can therefore be used for reliable line profile analysis.

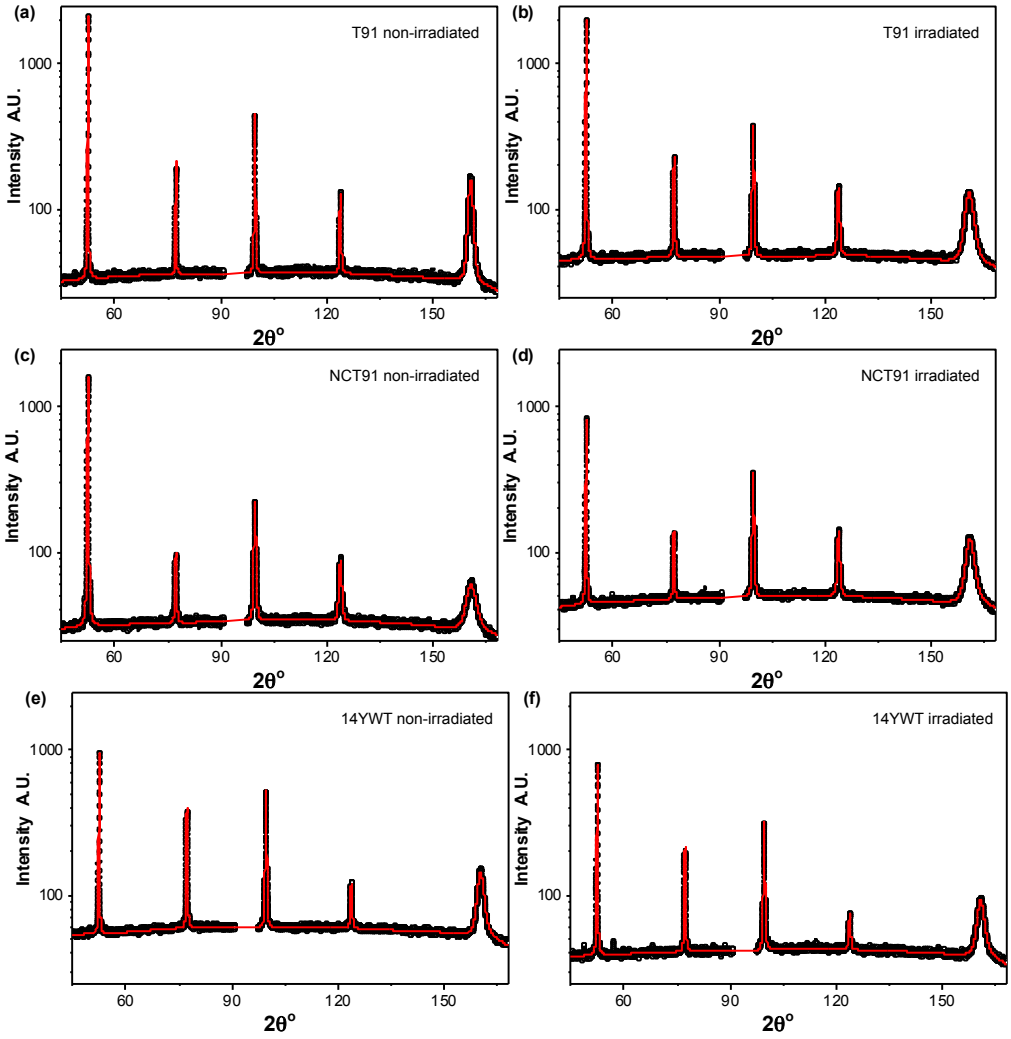

Figure 2.12 Measured (open circles) and CMWP calculated (red lines) XRD patterns (a) non-irradiated T91, (b) irradiated T91, (c) non-irradiated NCT91, (d) irradiated NCT91, (e) non-irradiated 14YWT and (f) irradiated 14YWT.

In order to provide control samples free from surface deformation, a ~2 x 1mm window was electropolished in specimens cut from in the bulk non-irradiated material. An electrolyte of 5% perchloric acid and 95% methanol was used and the time was controlled in order to remove ~100μm from the surface. This type of sample preparation has the advantage over mechanical polishing methods that it should not introduce any additional deformation in the surface of the samples and so provides a reliable reference value for the non-irradiated state. Due to a lack of control of the electropolishing technique and the relatively thin damage layer, it was not possible to electropolish the irradiated samples after irradiation. However, the careful polishing of the samples prior to irradiation would mean that any surface deformation would be minimal and the relatively large penetration depth of the Co X-rays ensures that the main contribution to the line broadening is from the irradiation-induced damage.

2.2 Nanoindentation: Results and discussion

2.3.1 Surface nanoindentation

Figure 2.13 illustrates the post irradiation nanoindentation for the surface indented samples. Figure 2.14 shows the hardness of the surface samples as a function of indentation depth obtained from QS indentation. Both the control and the irradiated hardness measurements of each sample are displayed in the same plot for comparison. Table 2.1 provides the average of hardness of all four alloys at a penetration depth of 1000 nm before and after irradiation, along with the increase in hardness in each of the alloy due to the ion irradiation. Although significant irradiation hardening was observed in the 800H and T91 alloys, a negligible hardening effect was observed in the NCT91 and 14YWT alloys, which is within the error of the measurements.

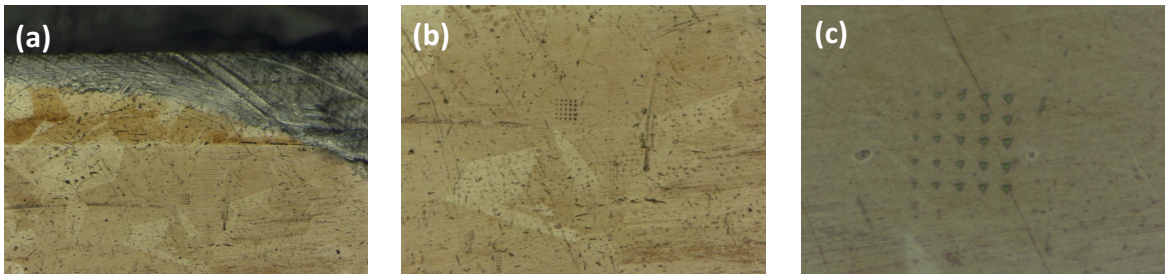

Figure 2.13 (a), (b) Examples of the post irradiation nanoindenation surface for the surface samples. (c) An example of surface indent fields.

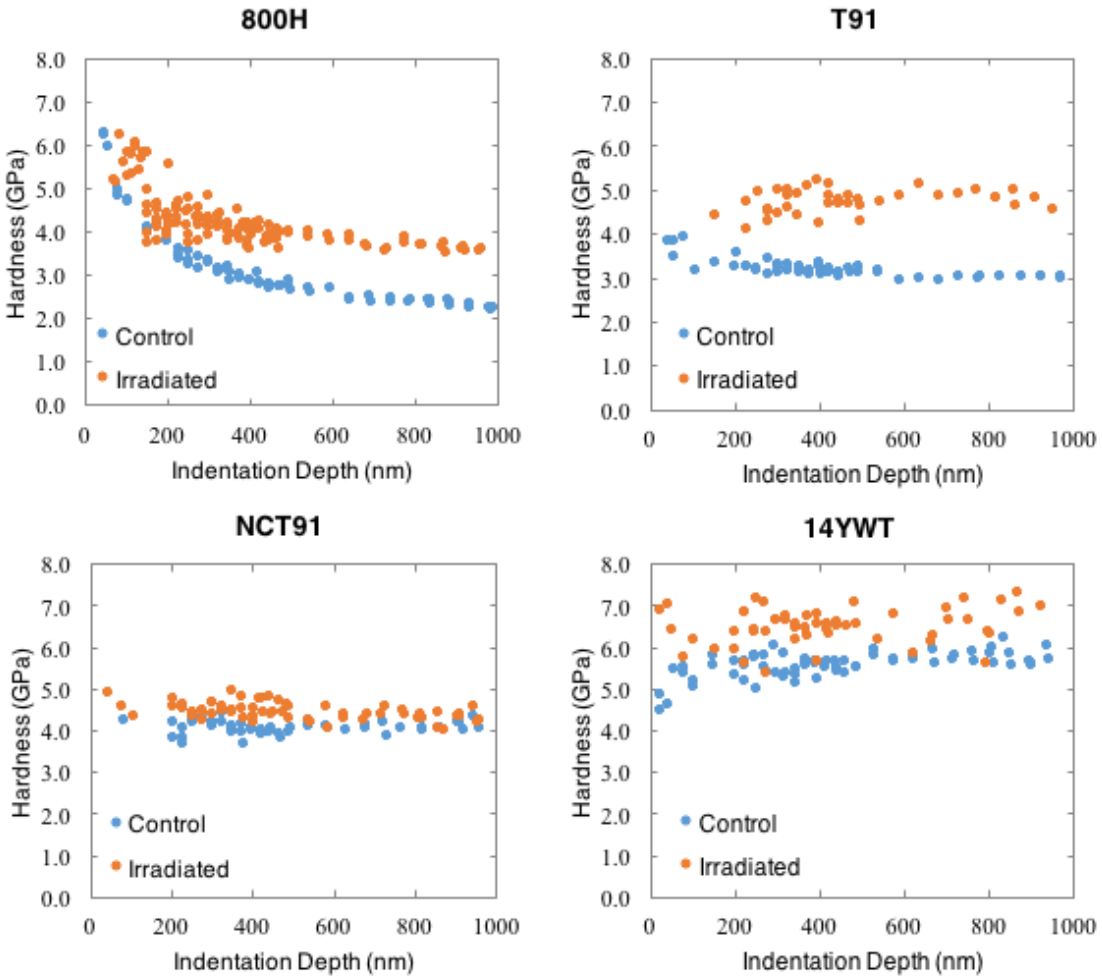

Figure 2.14 Surface hardness as a function of indentation depth.

Table 2.1 Hardness measurements obtained by nanoindentation on the surface

1000 nm depth		Hardness (GPa)	Difference in Hardness (GPa)
800H	Irradiated	3.63 ± 0.07	1.31
	Control	2.32 ± 0.08	
T91	Irradiated	4.77 ± 0.16	1.76
	Control	3.01 ± 0.02	
NCT91	Irradiated	4.28 ± 0.18	0.15
	Control	4.13 ± 0.11	
14YWT	Irradiated	7.04 ± 0.23	0.14
	Control	6.90 ± 0.39	

According to the hardness profiles, the 800H alloy appeared to be strongly size affected while the other samples were not. "Indentation size effect" is the phenomenon where hardness increases with decreasing penetration depth, making the measurements deviate from macroscopic hardness values. The size effect was characterized using the Nix and Gao model (Equation 1.5) [90]. H_0, which is the hardness in the limit of infinite depth, and h*, which is a characteristic length depending of the shape of the indenter, are the main parameters describing the size effect behavior. H_0 and h* can be calculated after plotting H^2 vs. 1/h. Typically, materials with a low size effect have a low h*, and materials with a large size effect have a high h*. The calculated h* values for all of the samples are tabulated in Table 2.2. The negative h* values are due to the slight hardness increase as a function of penetration depth, which is presumably due to small measurement errors within the error bars.

Table 2.2 Nix and Gao's h* values before and after irradiation

Sample	Before Irradiation		After Irradiation	
	h* (nm)	ISE	h* (nm)	ISE
800H	627	Strong	201	Moderate
T91	-2.97	None	-28.4	None
NCT91	16	None	41.5	None
14YWT	-8.06	None	-20.4	None

h* (nm)	ISE
>250	Strong
150 - 250	Moderate
50 - 150	Weak
<50	None

Figure 2.15 shows the hardness measurements obtained using the CSM technique. The average of 25 indentations is shown and error bars represent one standard deviation of the mean. Significant irradiation-induced hardening can be observed in the 800H alloy and the T91, however the NCT91 and the 14YWT show no significant irradiation induced hardening. It should be noted that there is a slight hardening effect in the 14YWT sample, which may be attributed to sample preparation or carbon contamination as highlighted in [121] in the low depth indents and microstructural heterogeneity beyond the surface region. In all samples and conditions, an indentation size effect was observed.

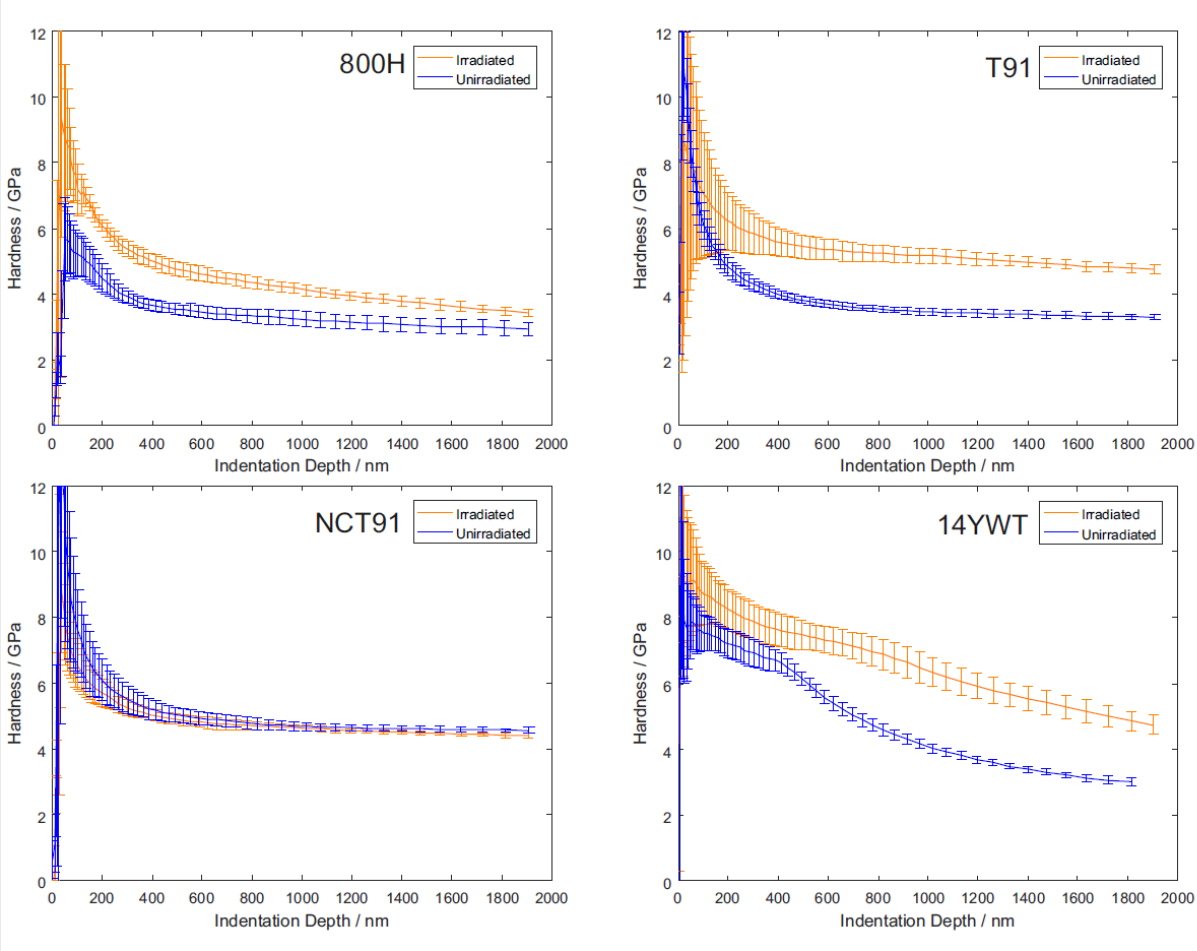

Figure 2.15 CSM indentation hardness measured from the surface of the sample.

2.3.2 Cross-section nanoindentation

Figure 2.16 show the post irradiation cross-section indents of the irradiated areas in cross-section samples as a function of distance from the edge.

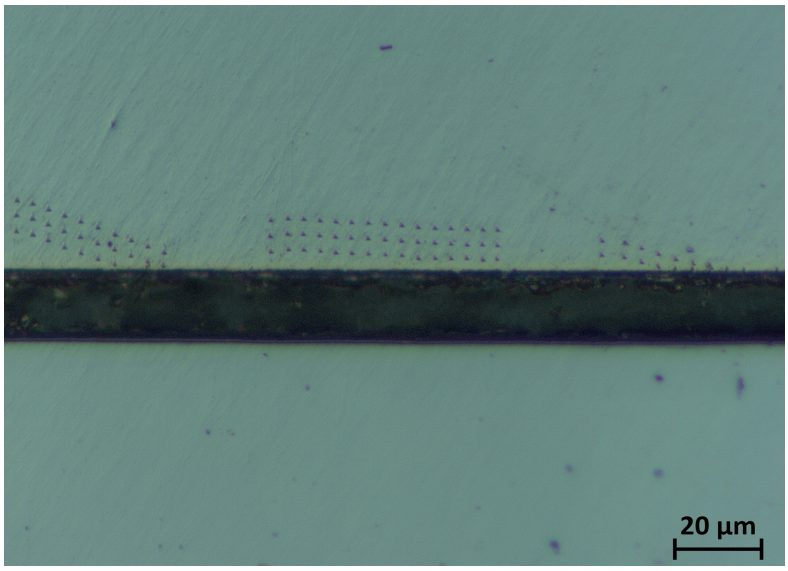

Figure 2.16 Example of indent fields performed on the cross-section samples.

Figure 2.17 shows hardness profiles from the cross-sectional samples, providing post-irradiation hardness measurements as a function of distance from the surface. A significant increase in hardness was observed in the irradiated regions of the 800H and T91 alloys. The hardness of 800H and T91 increased from 2.8 GPa to 4.2 GPa and from 3.8 GPa to 5.1 GPa, respectively. However, this characteristic was not observed in the NCT91 and 14YWT alloys. According to the hardness profiles, the hardness values did not deviate significantly from the average of ~4.5 GPa for NCT91 and ~6.9 GPa for 14YWT. The distinct hardness drop shown corresponds to the transition of the irradiated to the non-irradiated regions in the cross section of the sample. The 800H cross-section hardness profile suggests that the irradiation depth is approximately 6 µm. This agrees well with the SRIM predictions of 6.2 µm. The blue and the red lines in Figure 6 correspond to the average hardness at the same indentation depth (200 nm) in the control and the irradiated regions of the sample surface, respectively. While the surface hardness measurements reasonably match with the cross-section hardness measurements for 800H, T91 and NCT91, the agreement was not observed in the case of 14YWT due to the anisotropic microstructure.

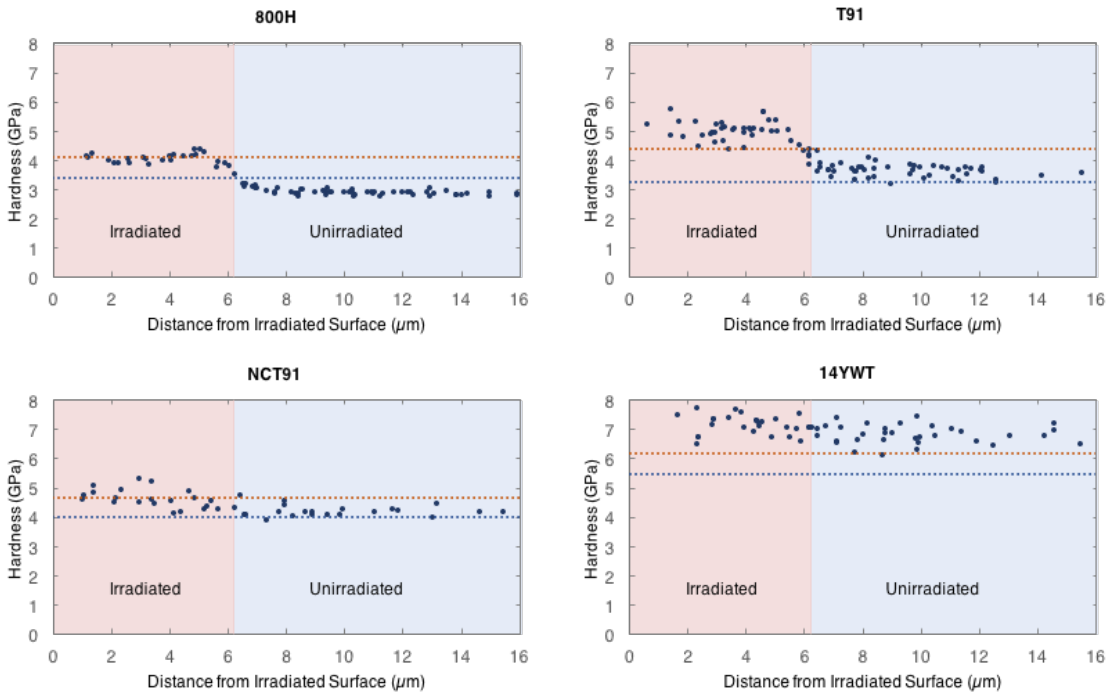

Figure 2.17 Hardness profile of cross-sectional samples as a function of distance from the edge (Penetration depth of 200 nm).

2.3 Microcompression: Results and discussion

Engineering stress and strain curves were obtained from microcompression testing. By taking the surface interactions between the tip and the pillars into account a 0.2% strain line parallel to the elastic region was plotted to obtain the offset yield point. Images of pillars in the non-irradiated and the irradiated area of the cross-sectional 800H sample before and after compression are shown in Figure 2.18. The corresponding stress-strain curves obtained from the load-displacement data and yield stresses are plotted next to each of the pillars for comparison. The yield stresses of the successfully compressed pillars fabricated in the non-irradiated and the irradiated area of the four samples are provided in Table 2.3. Pillars with possible experimental errors such as misalignment during the compression are excluded from the table.

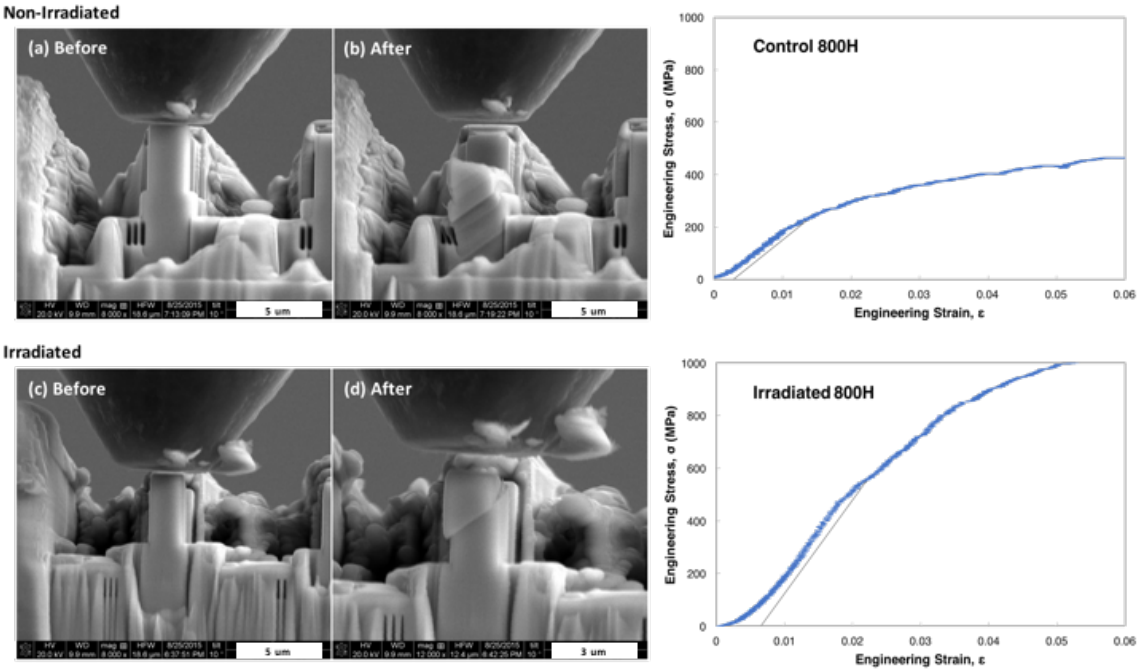

Figure 2.18 Microcompression testing of 800H pillars (a) non-irradiated area (b) irradiated area.

Table 2.3 Yield stresses obtained from microcompression testing in the control and the irradiated area

Sample	Yield Stress (MPa)							
	Non-Irradiated				Irradiated			
	Pillar 1	Pillar 2	Pillar 3	Average	Pillar 1	Pillar 2	Pillar 3	Average
800H	250	260	250	253 ± 6	625	580	575	593 ± 28
T91	945	730	660	778 ± 145	1,435	1,125	1,230	1,263 ± 158
NCT91	950	780	N/A	865 ± 120	920	860	N/A	890 ± 42
14YWT	2,380	1,658	1,240	1,759 ± 577	1,751	1,830	1,865	1,815 ± 58

2.4 X-Ray diffraction

X-ray diffraction also provides a useful tool for analyzing the microstructural properties of ion-irradiated layers. Due to limited penetration depth, the region from which X-rays are diffracted can be confined to the irradiated surface layer. X-ray line broadening can be used to probe the microstructure of materials non-destructively over statistically significant volumes, and so naturally complements small-scale mechanical testing techniques. The fitting of microstructural parameters to experimentally acquired profiles is achieved using the Convolutional Multiple

Whole Profile fitting (CMWP) algorithm, developed by Ungar et al. [122], and allows for the extraction of microstructural parameters, such as dislocation density and crystallite size. Although the code was originally developed for the investigation of deformed microstructures [120, 123-125], it has recently been successfully used to understand irradiation damage in materials [69,126].

Figure 2.19 shows the measured XRD patterns from non-irradiated and irradiated samples. Due to the large grain size of the 800H alloy, it was not possible to get sufficient statistics for accurate CMWP analysis and so the XRD investigation focused on the smaller grained BCC materials. The calculated profiles from CMWP are overlaid on the measured profiles in Figure 4. Good agreement was observed between the measured and calculated profiles for all the measured samples. The microstructural parameters from the CMWP analysis are shown in Table 2.4. The strongest increase in the dislocation density was observed in the T91 specimen, which showed a 5-fold increase in dislocation density after irradiation. In contrast, the nanocrystalline T91 showed an almost negligible increase in dislocation density after irradiation, considering the error in the values. The dislocation density of the 14YWT alloy was observed to double after irradiation, although the change in dislocation density was significantly less than that observed in T91.

Table 2.4 Microsctrutural parameters from CMWP evaluation of XRD profiles of control and irradiated BCC alloys

CMWP		$\langle x \rangle_{area}$ (nm)	ρ (10^{14} m^{-2})	M	q
T91	Irradiated	87 (±10)	14.8 (±1)	5.3 (±0.7)	1.6 (±0.1)
	Control	114 (±12)	2.7 (±0.2)	11 (±2)	1.2 (±0.2)
NCT91	Irradiated	67 (±8)	19.8 (±1.2)	2.8 (±0.4)	1.5 (±0.1)
	Control	70 (±8)	17.8 (±1.2)	5.7 (±0.8)	1.3 (±0.2)
14YWT	Irradiated	67 (±8)	16.3 (±1.1)	2.6 (±0.4)	2.0 (±0.1)
	Control	82 (±8)	7.6 (±0.6)	6.8 (±1)	1.9 (±0.1)

In order to qualitatively assess the diffraction patterns using the full width at half maximum (FWHM) of the reflections, modified Williamson-Hall (mWH) plots were created using the measured profiles and are shown in Figure 9 [123]. The figures show that for each investigated sample the slope of the mWH plot increases after irradiation; the change is large for T91, and small for NCT91 and 14YWT. Qualitatively, the slope of a mWH plot increases a function of dislocation density, as Eq. 5 in [123] demonstrates. Thus, the qualitative trends shown by the mWH plots for the dislocation densities are in agreement with the results of the quantitative CMWP analysis.

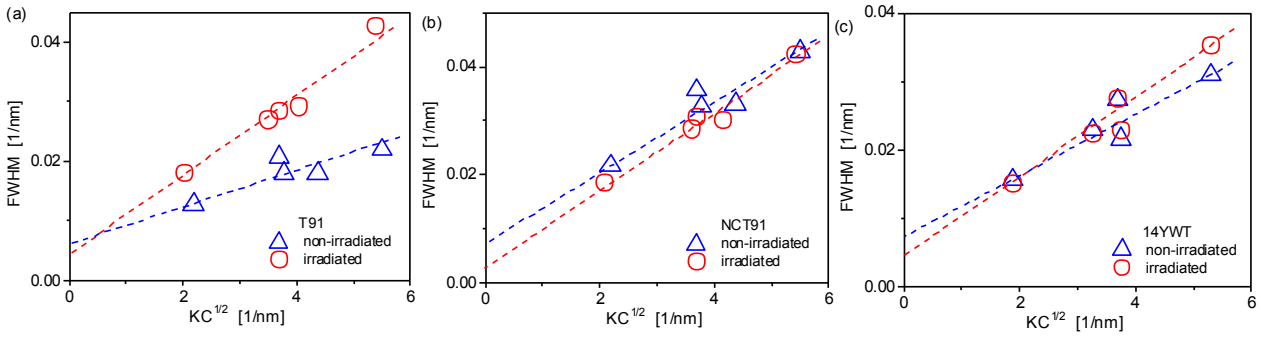

Figure 2.19 Modified Williamson Hall plots for T91, NCT91 and 14YWT measured from experimental XRD profiles.

Some interesting trends were also observed in the other microstructural parameters determined from CMWP, see Table 2.4. The *M* parameter shows the dipole character of the dislocations and can be considered as a measure of the degree of dislocation arrangement present in the sample. *M* is observed to decrease by approximately half in all three specimens after irradiation, indicating an increase in the ordering of irradiation-induced dislocations. The *q* parameter is a measure of the *hkl* dependence of the line broadening and can be used to determine the edge/screw nature of dislocations in cubic materials [127]. In BCC steels, the average screw/edge character would give $q = \sim 1.8$ with lower or higher values indicating a larger edge or screw ratio respectively. Negligible changes in the *q* parameter are observed after irradiation in all samples, however a lower average value is observed in T91 and NCT91 alloys than in 14YWT indicating 14YWT has a higher ratio of screw dislocations and the T91 alloy have a higher edge ratio. The errors for all parameters are shown in Table 2.4, and are determined by running the evaluation several times. As CMWP is a statistical Monte-Carlo procedure, this can lead to natural variation in the results, however it can be seen that with errors included, the trends in the microstructural parameters remain.

2.5 Discussion and technique comparisons

Hardness saturates after a certain dose at a temperature in indentation testing (typically around 10dpa) as it has been shown by others [61], which is the same way as yield stress saturates at a similar dose on materials [51,73-74]. Hardness as well as yield stress cannot increase indefinitely due to the fact that there are only a certain number of defects that can be fit within a specific volume. From the current results we can conclude that for the alloys of interest, hardness saturates either at 20 dpa or lower (likely at 10 dpa) as has been observed in other materials [51,61,128-129].

Comparing the size effect parameters of the different samples to each other provides insight into the materials microstructure. It is found that the softer FCC material, with a large grain size and low defect density, experiences a large size effect while the BCC materials, with a fine microstructure and significant defect density, have a lower size effect. This is in good agreement with Nix and Gao as well as others [90] and can be explained by the fact that fully annealed, large-grained materials generally have less stored dislocations and dislocation pinning points. It is also observed that the size effect is significantly reduced with the addition of radiation damage, in

agreement with these observations. It does raise the question, however, how macroscopic properties can be derived from nanoscale tests if the size effect changes as a function of irradiation damage. A simple ΔH value will not allow for the estimation of macroscopic hardness values and therefore yield strength. It is therefore a requirement that the size effect is known in order to estimate macroscopic properties for a given material. However, there is rarely sufficient ion-irradiated material available to perform a size effect study, which makes this approach difficult. However, the fact that minimal size effect was observed in the irradiated material leads to the assumption that the nanohardness is representative of the bulk material. Therefore, it is possible to measure the hardness of the irradiated material at the small scale with hardness measured at the larger scale on bulk non-irradiated material in order to calculate the delta hardness. A similar technique was outlined in [130].

The hardness measurements obtained using the CSM method, in the surface of the sample agree reasonably well with the surface indentation results obtained from the quasi-static technique with the exception of the 14YWT material. The microstructure of the 14YWT had a small grain size with grains ranging from as small as 100nm to 1μm in size. Due to the difference in the average grain sizes and precipitate distributions, it is possible to suggest that the QS experiments were made in a region with a low precipitation density and/or a large average grain size and the CSM experiments were made in a region of the sample with a high density of precipitates and/or a small average grain size. This would explain the difference in the hardness measured from each technique.

A size effect is observed for all samples in both the irradiated and unirradiated conditions. In this technique, the hardness is continuously being measured whilst the indenter is penetrating deeper into the material. As the displacement increases, the volume of material being sampled beneath the indenter (i.e. the plastic zone) will evolve from containing purely damaged material, to a combination of unirradiated and irradiated until finally at large penetration depths the unirradiated material will dominate the hardening response and the irradiated and unirradiated hardness curves will converge. At the depth at which this transition occurs (i.e changing from purely irradiated to a mixture), a change in the hardness behavior can be observed. This is clearer for the T91 and the 14YWT samples (see irradiated hardness curves of T91 and 14YWT in Figure 2.15) where a distinct ‘kink’ in the hardness curve can be observed. A similar ‘kink’ can be observed in the unirradiated hardness curve for the 14WYT sample. This can be explained from the geometry of the irradiation set up. Indentations in the unirradiated region of the sample were taken from the surface of the sample that was shielded from the ion-beam (Figure 2.2). In the case of the 14YWT sample, the unirradiated portion of the sample was clamped down during the irradiation. This ‘clamping’ mechanism created mechanical damage to the surface of the material which resulted in a distinct ‘kink’ in the unirradiated nanoindentation hardness measurements. As a result, the CSM non-irradiated hardness data for the 14YWT sample was not used for comparison.

Microcompression testing revealed significantly higher yield stresses in 800H and T91 in the irradiated area than the control area. However, a much smaller difference in the yield stress values was obtained in the control and the irradiated area of NCT91 and 14YWT. This agrees well with the nanoindentation results, confirming irradiation hardening in 800H and T91 but not in NCT91 and 14YWT. Although the focus of this paper is not to compare the mechanical property evolution resulting from ion irradiation to that resulting from neutron irradiation, it is worth noting that, as

an example, a considerable increase in yield stress has also been observed in neutron irradiated T91 [131]. Along with the increase in yield stress, the increase in hardness due to irradiation hardening was observed in neutron irradiated T91 [132], thus confirming the similarities between ion irradiated and neutron irradiated alloys in this aspect of mechanical property evolution.

In order to cross compare between nanoindentation and microcompression, and relate both small-scale mechanical testing methods, yield stress can be obtained from nanoindentation by converting Berkovich hardness (H_b) to Vickers hardness (H_v) (Eqn. 2.1) then to yield stress (σ_y) (Eqn. 2.2) [133].

$$H_V = 94.5\,H \qquad \text{(Eqn. 2.1)}$$

$$\sigma_y = 2.82\,H_V - 114 \qquad \text{(Eqn. 2.2)}$$

Figure 2.20 compares the difference in yield stresses of the four alloys obtained from nanoindentation and microcompression before and after irradiation. The agreement between the two testing methods results in the increase in confidence in the field of small-scale mechanical testing. Discrepancies between the two testing methods could be due to the different nature of the stress states for each method. While nanoindentation is associated with triaxial stress state, microcompression is a uniaxial type of testing.

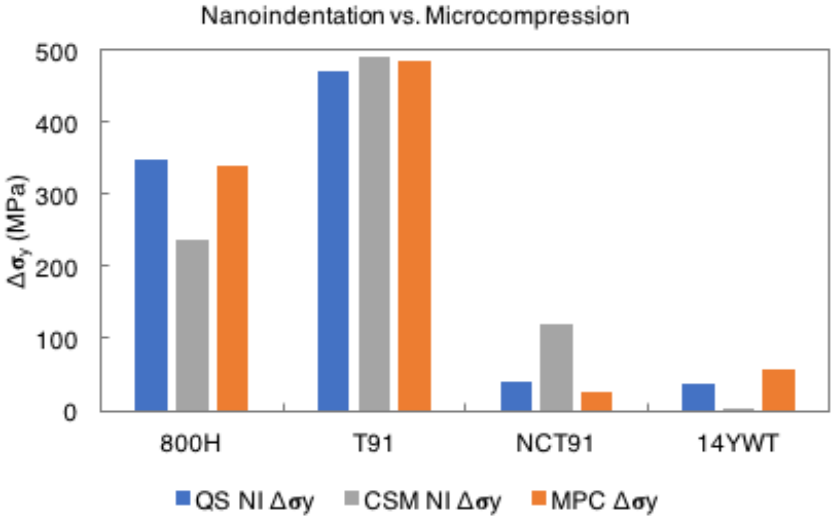

Figure 2.20 Difference in yield stresses before and after irradiation obtained from nanoindentation and microcompression experiments.

Table 2.5 Quasi-static (QS) and Continuous Stiffness Measurement (CSM) Indentation data for four alloys of interest

QS		H_b (GPa)	H_v (GPa)	NI σ_y (MPa)	NI $\Delta\sigma y$ (MPa)	MPC σ_y (MPa)	MPC $\Delta\sigma y$ (MPa)
800H	Irradiated	3.63	343	853	349	593	308
	Control	2.32	219	504		285	
T91	Irradiated	4.77	451	1158	471	1263	485
	Control	3.01	284	687		778	
NCT91	Irradiated	4.28	404	1025	39	890	25
	Control	4.13	390	986		865	
14YWT	Irradiated	7.04	665	1761	36	1815	56
	Control	6.9	652	1725		1759	

CSM		H_b (GPa)	H_v (GPa)	NI σ_y (MPa)	NI $\Delta\sigma y$ (MPa)	MPC σ_y (MPa)	MPC $\Delta\sigma y$ (MPa)
800H	Irradiated	4.12	389.34	983.9388	237.1761	593	341
	Control	3.23	305.235	746.7627		252	
T91	Irradiated	5.06	478.17	1234.4394	490.3416	1263	485
	Control	3.22	304.29	744.0978		778	
NCT91	Irradiated	4.67	441.315	1130.5083	119.9205	890	25
	Control	4.22	398.79	1010.5878		865	
14YWT	Irradiated	7.09	670.005	1775.4141	2.6649	1815	56
	Control	7.08	669.06	1772.7492		1759	

The initial dislocation density, as measured by CMWP, of the NCT91 alloy was the highest of all 3 BCC samples, and was in fact higher than the dislocation density of the other alloys after irradiation (Table 2.4). This is to be expected due to the severe plastic deformation technique used to fabricate these nanocrystalline alloys [134]. The resulting nanocrystalline grain structure, with sub-micron grain size, is likely to be responsible for the irradiation resistance of this alloy due to an increased concentration of grain boundaries, which are know to be effective neutral defect sinks [43]. This is reflected by the negligible increase in dislocation density observed in NCT91 after irradiation, which is within the error in the measurement and agrees with the negligible change in hardness observed in this alloy during nanoindentation tests. In comparison, the initial dislocation density of coarse-grained T91 was significantly lower than NCT91 as would be expected from a relatively large grained, annealed material. The non-irradiated dislocation density measured from the XRD profiles was ~ 3 times that as reported from TEM investigations [17], although the dislocation density was observed to vary dramatically throughout the microstructure. This alloy experienced the largest increase in dislocation density after irradiation, a 5-fold increase, which agrees with the severe irradiation hardening observed during the small-scale mechanical tests.

The initial dislocation density of the 14YWT alloy sits between the T91 and NCT91 control samples and agrees well with previous TEM measurements on 14YWT [135]. A relatively small increase in dislocation density after irradiation was observed compared to T91, which is most likely due to the large number density of ultra-fine nanoclusters present in the 14YWT microstructure. These nanoclusters act as selective sinks for defects, encouraging self-healing of damage through recombination with self-interstitial atoms [136]. The larger grained 14YWT microstructure is not as effective in mitigating irradiation damage as the nanograined T91 microstructure, probably due to the fact that nanoclusters are less efficient defect sinks than grain boundaries. Although the scatter in the data is greater, most likely due to a more heterogeneous microstructure, this is also reflected in the nanoindentation data (Figure 2.14) that shows a larger increase in hardness after irradiation in the 14YWT alloy than in NCT91. In addition, a similar trend is observed in the yield stress as determined from the microcompression experiments (Table 2.3), although this is not observed in the calculated yield stress obtained from the nanoindentation measurements. This could be because of the different types of stress state of each testing technique.

2.6 Comparisons of nanoindentation measurements from different indenters

Nanoindentation has been performed on the control surface 800H at the temperatures of 25 °C (room temperature), 100 °C, 200 °C and 300 °C, covering the depth range of 80 – 380 nm (Hysitron TriboIndenter 950, UCB) and 300 – 1000 nm (Micro Materials NanoTest, UCB). As evident in Figures 2.21 – 2.24, which show the hardness profiles across all indentation depth range, there was a very good consistency between the two machines. Hardness and modulus decreased with temperature as expected.

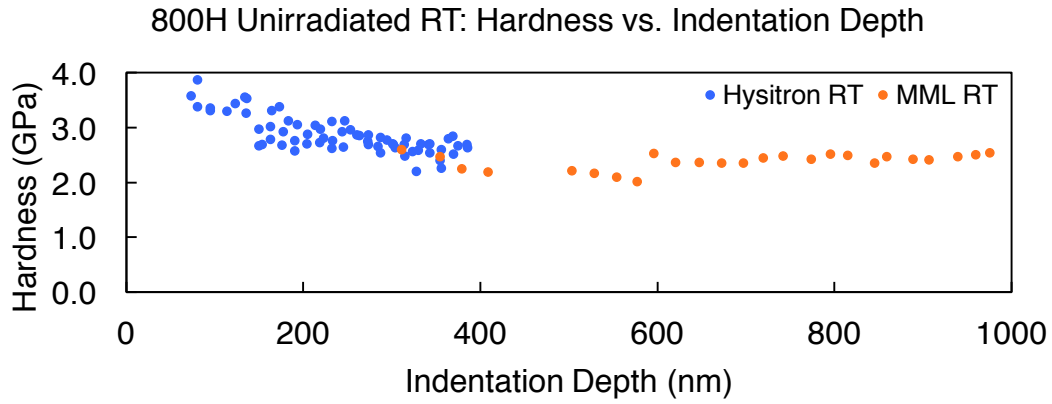

Figure 2.21 Hysitron TriboIndenter 950 and Micro Materials indenter - Surface hardness at room temperature as a function of indentation depth.

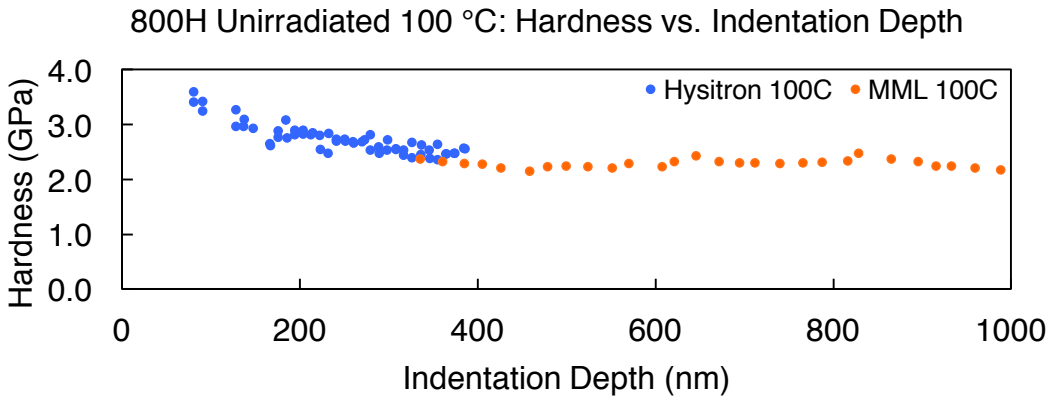

Figure 2.22 Hysitron TriboIndenter 950 and Micro Materials indenter - Surface hardness at 100 °C as a function of indentation depth.

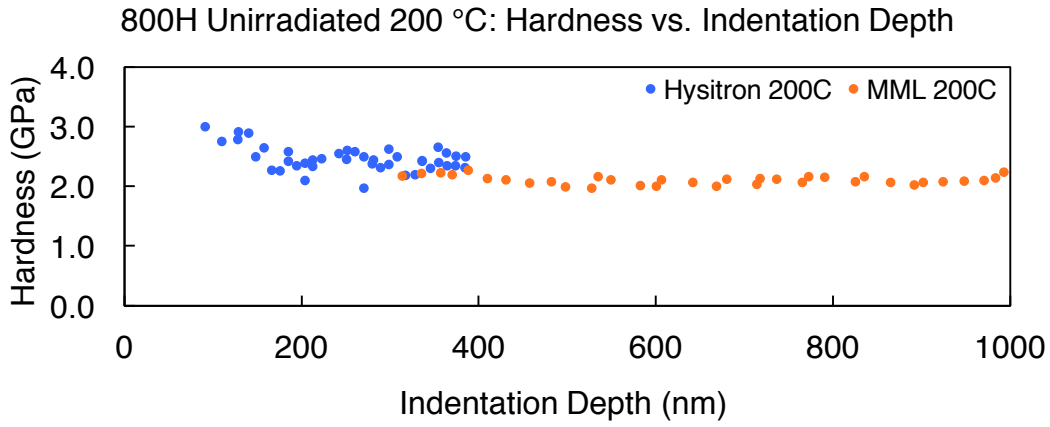

Figure 2.23 Hysitron TriboIndenter 950 and Micro Materials indenter - Surface hardness at 200 °C as a function of indentation depth.

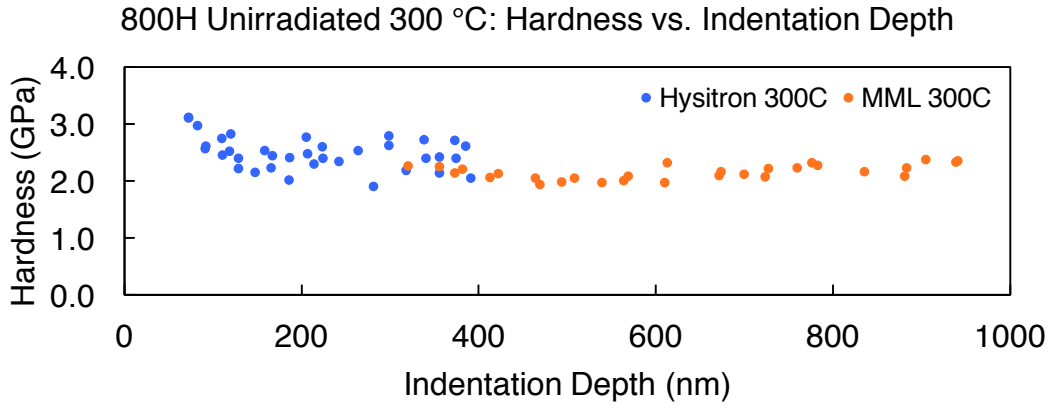

Figure 2.24 Hysitron TriboIndenter 950 and Micro Materials indenter - Surface hardness at 300 °C as a function of indentation depth.

Chapter 3

Indentation Size Effect (ISE)

3.1 ISE studies without EBSD

The first two sets of experiments were performed without taking grain orientation into consideration. Indentation size effect studies were carried out with the hardness measurements from multiple grains or in other words, from a polycrystalline volume. Figure 3.1 shows the size effect parameter h* as a function of temperature for two rounds of experiments with the same setup and parameters. The ISE is less significant with temperature for the first set of experiments while the opposite trend is observed for the second set. This implies that it is not possible to study ISE by sampling polycrystalline volume.

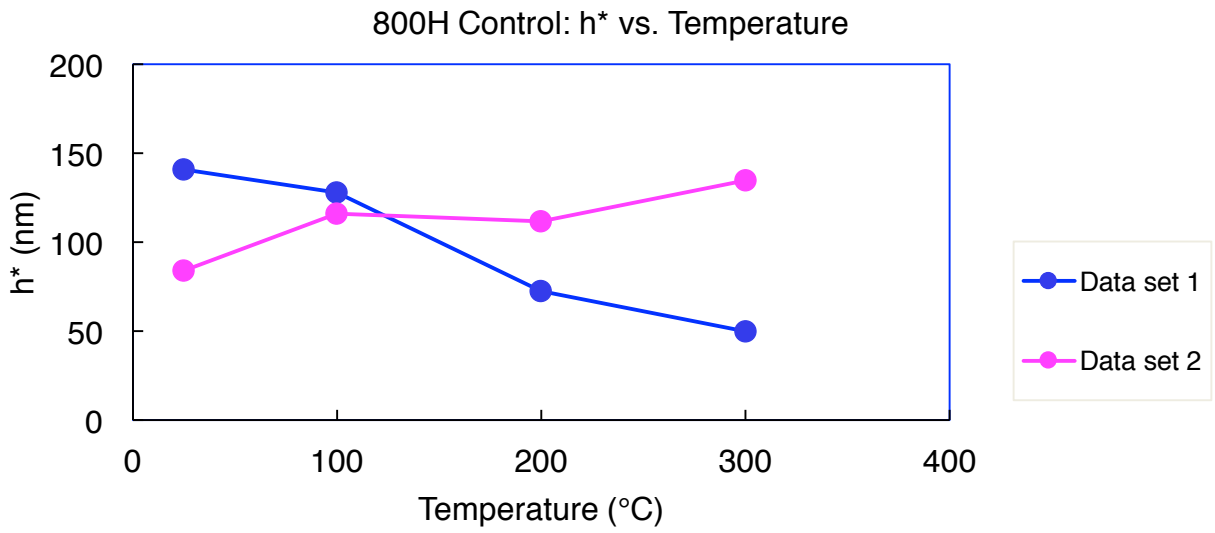

Figure 3.1 Opposite trends observed from two rounds of indentation size effect studies without taking grain orientation into consideration.

3.2 Experimental

The austenitic alloy 800H steel (31.6Ni-20.4Cr-45.5Fe (wt%)) is of particular interest for investigation due to its potential use as a structural material in nuclear reactors and is therefore selected for this study. Due to its high nickel and chromium content, 800H has superior mechanical properties such as swelling and void formation resistance, making it a strong candidate structural material for high temperature and nuclear applications [38]. Two grains of known orientation, in both the unirradiated and the irradiated 800H, were selected for this study and nanoindentation testing on each of the selected grains was performed up to 300 °C. One of the two orientations in the unirradiated and the irradiated 800H were purposely chosen to be the same for direct comparisons between the unirradiated and the irradiated conditions.

3.2.1 Sample preparation for EBSD

After irradiation the sample was polished again using the same procedure removing approximately 200nm of material leaving sufficient irradiated material for testing. This process is critical since ISE occurs at low penetration depths and is thus sensitive to surface irregularities while it was found that the as irradiated sample contained a thin layer of residue on top and therefore post irradiation EBSD was not possible. A series of indents of increasing depths were placed prior to polishing the sample with 0.1 µm diamond solution. The indents served as markers to ensure that less than 200 nm of irradiated layer was removed due to the polishing.

3.2.2 EBSD scans to identify grain orientations

EBSD was performed on both the unirradiated and the irradiated 800H to search for two grains of known orientations large enough to contain all indents for ISE studies at all temperatures, and the same orientation. The orientation <111> and <131> for the unirradiated 800H and <111> and <113> for the irradiated 800H were selected. Both EBSD scans are shown in Figure 3.2.

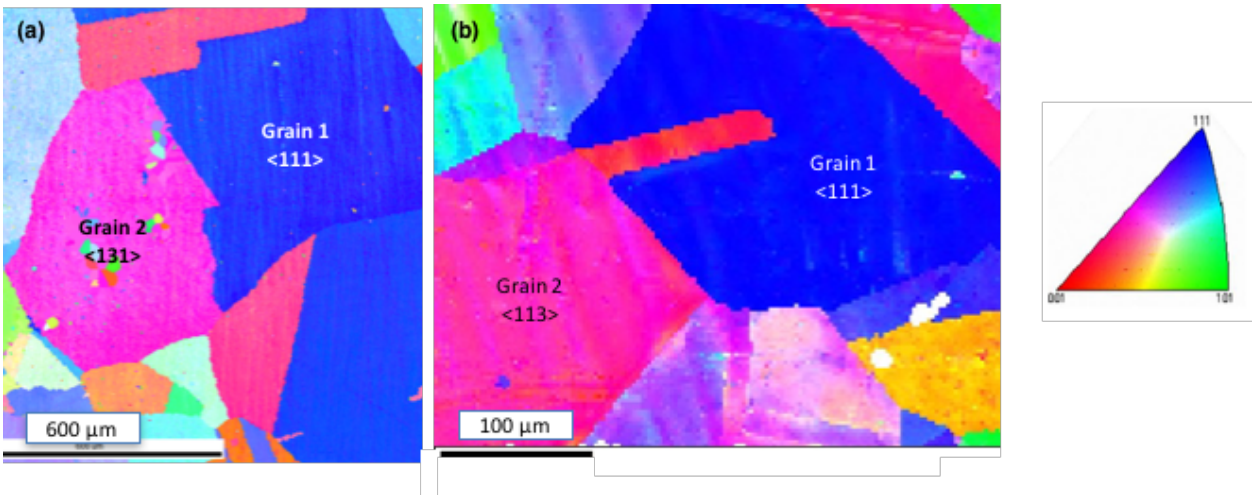

Figure 3.2 EBSD scans of the (a) unirradiated and the (b) irradiated 800H.

3.2.3 Nanoindentation

All the nanoindentation experiments were performed on the Hysitron Triboindenter TI-950 with the xSol high temperature stage (schematic provided in Figure 3.3 [137]). Hysitron's xSol high temperature stage enables high resolution nanomechanical measurements to be performed over a broad temperature range. The thermally stable xSol stage design provides excellent feedback-controlled temperature accuracy, fast stabilization times (under tight PID control), and a thermally stable stage design that enables quantitative, accurate, and reliable nanomechanical characterization at elevated temperatures up to 800°C. Dual resistive heating elements eliminate temperature gradients within the sample for a uniform temperature to the outermost testing surface. xSol's exclusive heating element architecture and proprietary probe design provides passive tip heating for isothermal tip-sample contact. Dissipated heat is transported outside of the instrument

enclosure through the xSol's liquid-cooled metal base [137]. The Hysitron xSol apparatus has been successfully used in several studies involving high temperature material performance [138-142].

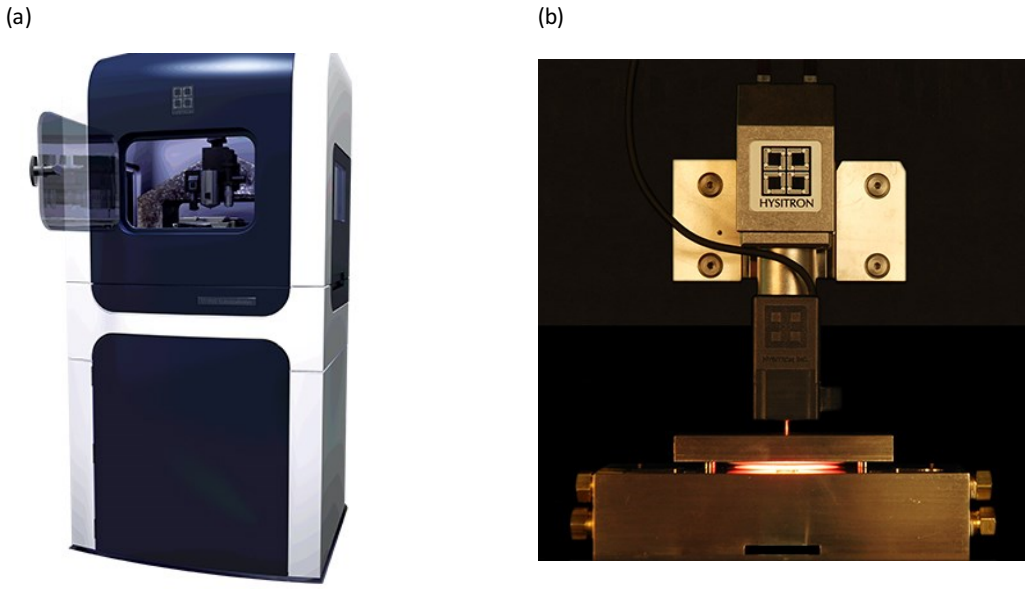

Figure 3.3 Hysitron Triboindenter TI-950 with the xSol high temperature stage [137].

For all the nanoindentation tests reported in this work, an Ar-H 5% cover gas was used to minimize oxidation. A diamond Berkovich probe, with a tip area function calibrated to Fused Quartz was used for the measurements. Indents were performed in an array of 5 x 4 indents per sample (unirradiated and irradiated) per grain location per temperature covering the depth range from 100 nm to 400 nm, and were spaced at a minimum of 10 μm apart from each other to avoid plastic zone interactions. Considering plastic zone size to be five times the indentation depth, for a 400-nm deep indent, the volume sampled is approximately 2 μm in radius, which is well within the irradiation penetration depth of 6.2 μm [59]. All the indents were performed in the displacement control quasi-static mode with a 5 second long segment each for loading, hold and unloading. Both the unirradiated and irradiated samples were tested at four different temperatures: room temperature, 100 °C, 200 °C and 300 °C. Due to the excellent thermal stability of the xSol high temperature stage, no more than a 10-minute hold was necessary before beginning testing at every temperature. The load-displacement curves from indentation testing were reproducible across all testing temperatures. The hardness was obtained from load vs. displacement curves according to the Oliver-Pharr method [62].

3.3 Results: Unirradiated and irradiated

Unirradiated 800H

Hardness and modulus measurements of the unirradiated <111> and <131> oriented grains are provided in Figure 3.4 and Figure 3.5, respectively. Figure 3.6 shows the data obtained from a the <111> oriented grain in the unirradiated 800H at room temperature. This represents the data set obtained for each of the specific test conditions, i.e., irradiation conditions, grain orientations and

temperatures. Figures 3.6 (a) shows the measurements of the hardness and the reduced modulus (indentation modulus), respectively, as a function of indentation depth. The error bars represent the standard deviations. Note that modulus values mentioned in this study refer to the reduced modulus or the indentation modulus. The Nix and Gao model was used to study the ISE, plotting the square of hardness H^2 vs the inverse of indentation depth $1/h$, where the linear fit with slope and intercept can be used to calculate the characteristic depth h^* which scales with size effect (Figure 3.6 (b)). R^2 was equal to or over 92% for all the unirradiated 800H data sets.

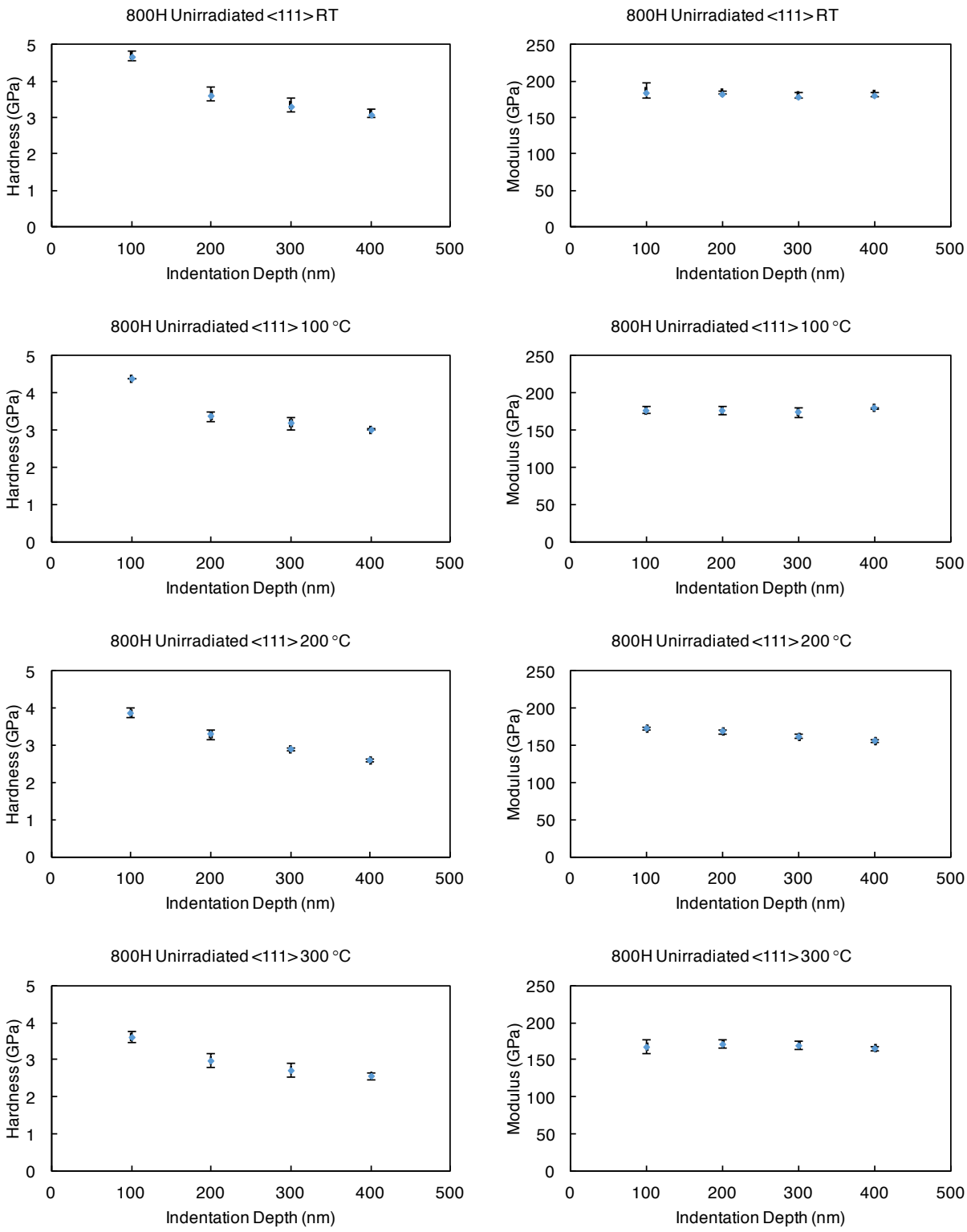

Figure 3.4 Hardness and modulus measurements of the unirradiated <111> 800H.

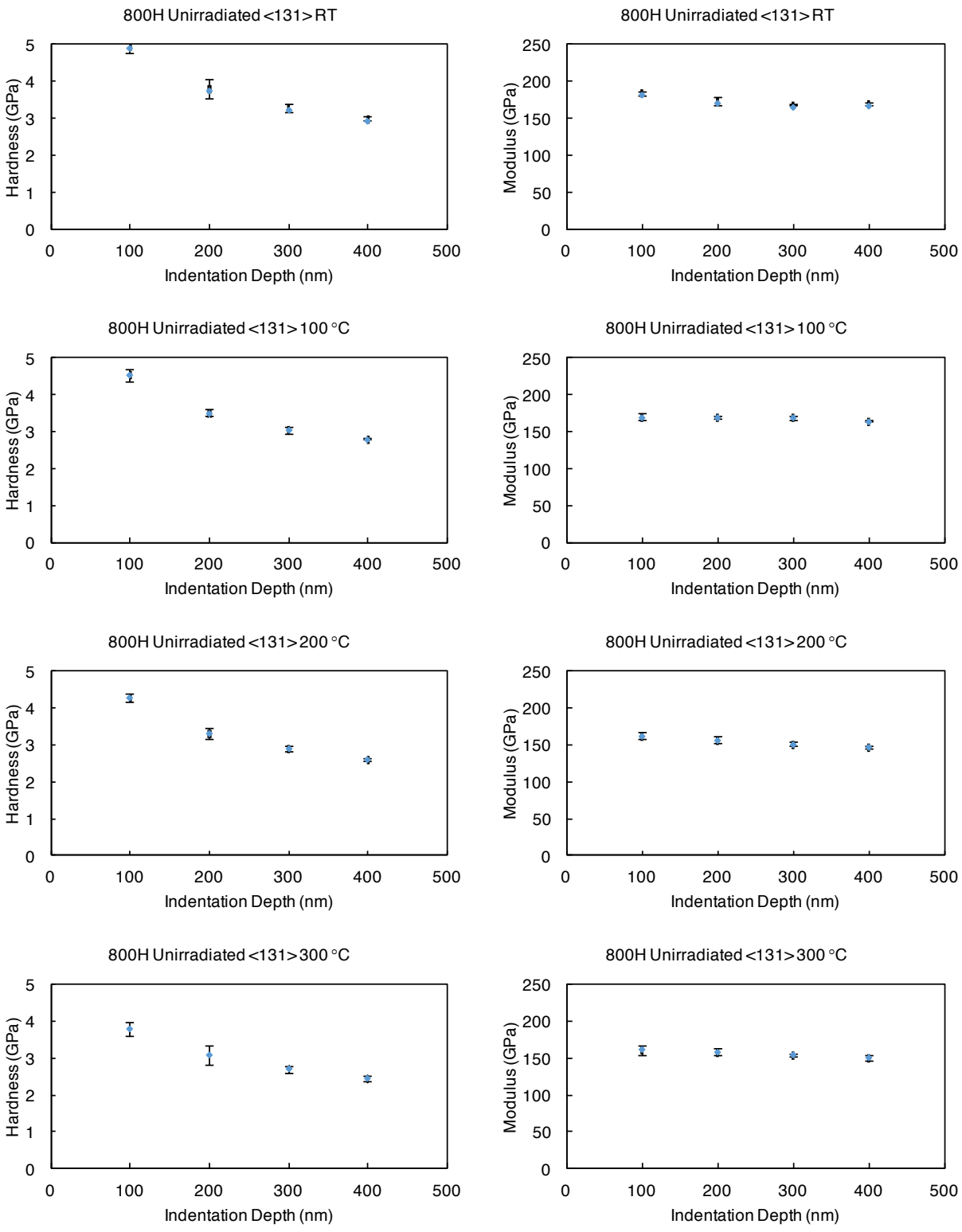

Figure 3.5 Hardness and modulus measurements of the unirradiated <131> 800H.

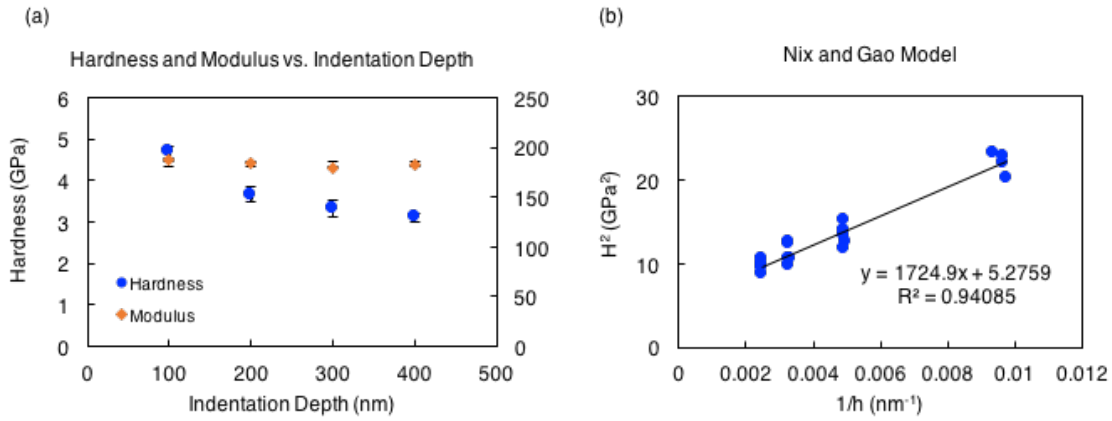

Figure 3.6 Unirradiated 800H; <111> grain orientation at room temperature: Nanoindentation results (a) Hardness and reduced modulus as a function of indentation depth (b) Nix and Gao plot showing how indentation size effect is calculated.

The hardness profiles for both grain orientations i.e. <111> and <131> are illustrated in Figures 3.7(a) and (c). Different colors of data points refer to different testing temperatures. At 100 nm indentation depth, the hardness of the <111> grain decreases from 4.69 GPa at room temperature to 3.63 GPa at 300 °C (22.6%). On the other hand, at the indentation depth of 400 nm, there is a 16% drop (3.1 GPa to 2.6 GPa) in the same grain. In the case of a <131> grain, the hardness decreases from room temperature to 300 °C at 100 nm and at 400 nm are from 4.91 GPa to 3.78 GPa (23%) and 3 GPa to 2.4 GPa (20%), respectively. It is therefore clear that the hardness decreases with increasing depth at different rates for each temperature, implying different size effect behaviors. Figures 3.7(b) and (d) provide the reduced modulus profiles for both grain orientations. At the indentation depth of 400 nm, the reduced modulus of the <111> grain decreases from 182 GPa at room temperature to 165 GPa at 300 °C (9%). At the same depth, the reduced modulus of the <131> grain decreases from 169 GPa at room temperature to 150 GPa at 300 °C (11%). The calculated drops in reduced modulus with temperature agrees well with the tensile modulus stated in the literature, which is approximately 9% from 20 °C to 300 °C [143]. Due to a scatter of measurement data, it may seem that modulus slightly decreases with indentation depth. However, when taken into account the standard deviations, the 'size effect' trend of the modulus as a function of indentation depth is negligible. Figures 3.8(a) and (b) plot the calculated hardness at infinite depth or the bulk hardness H_0 and the characteristic depth h^* or ISE, respectively, over temperature for the two grain orientations tested in the unirradiated sample. The data from the figures are also summarized in Table 3.1.

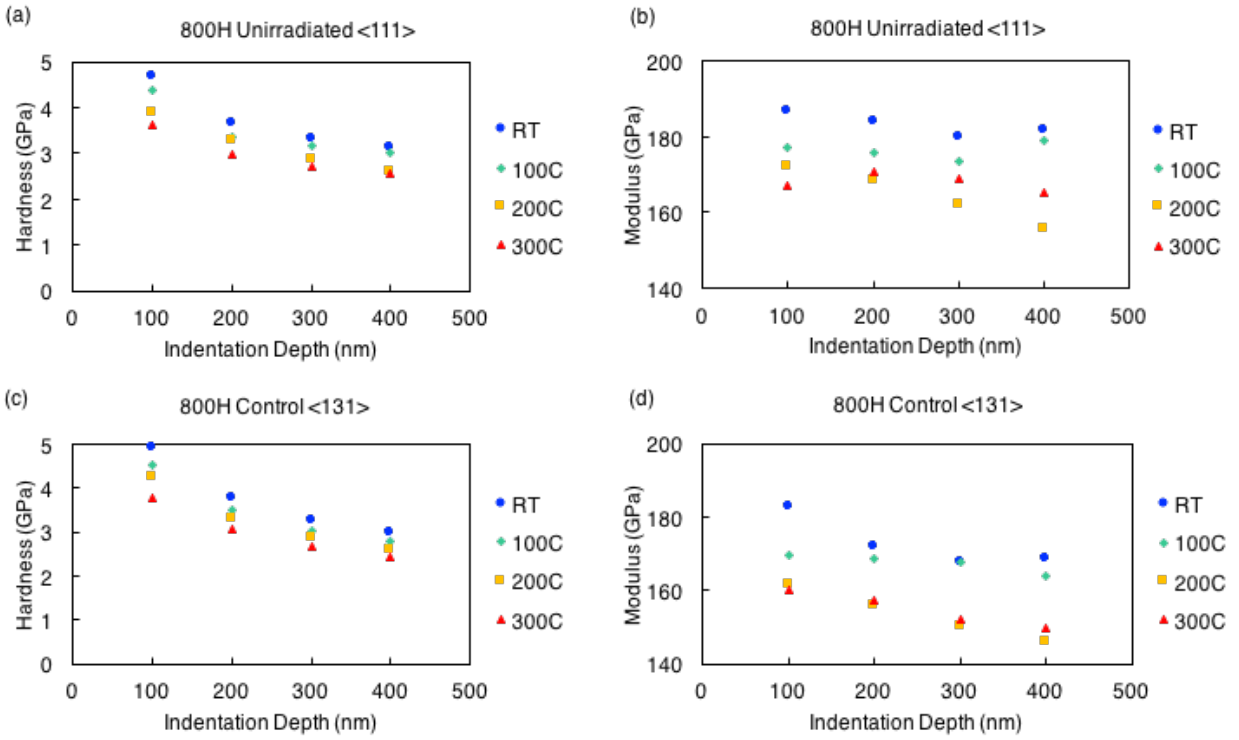

Figure 3.7 Unirradiated 800H; Hardness and modulus profiles as a function of depth and temperature of grains of <111> orientation and <131> orientation.

Table 3.1 Size effects at each testing temperature in each grain orientation in unirradiated and ion-irradiated 800H

	Unirradiated				Ion-Irradiated			
Temp (°C)	<111>		<131>		<111>		<113>	
	H_0	h*	H_0	h*	H_0	h*	H_0	h*
25	2.3	327	1.93	571	3.58	176	3.51	172
100	2.32	251	1.88	481	3.51	127	3.31	129
200	2.11	255	1.77	487	3.45	122	3.11	122
300	2.11	200	1.85	324	3.35	97	3.06	91

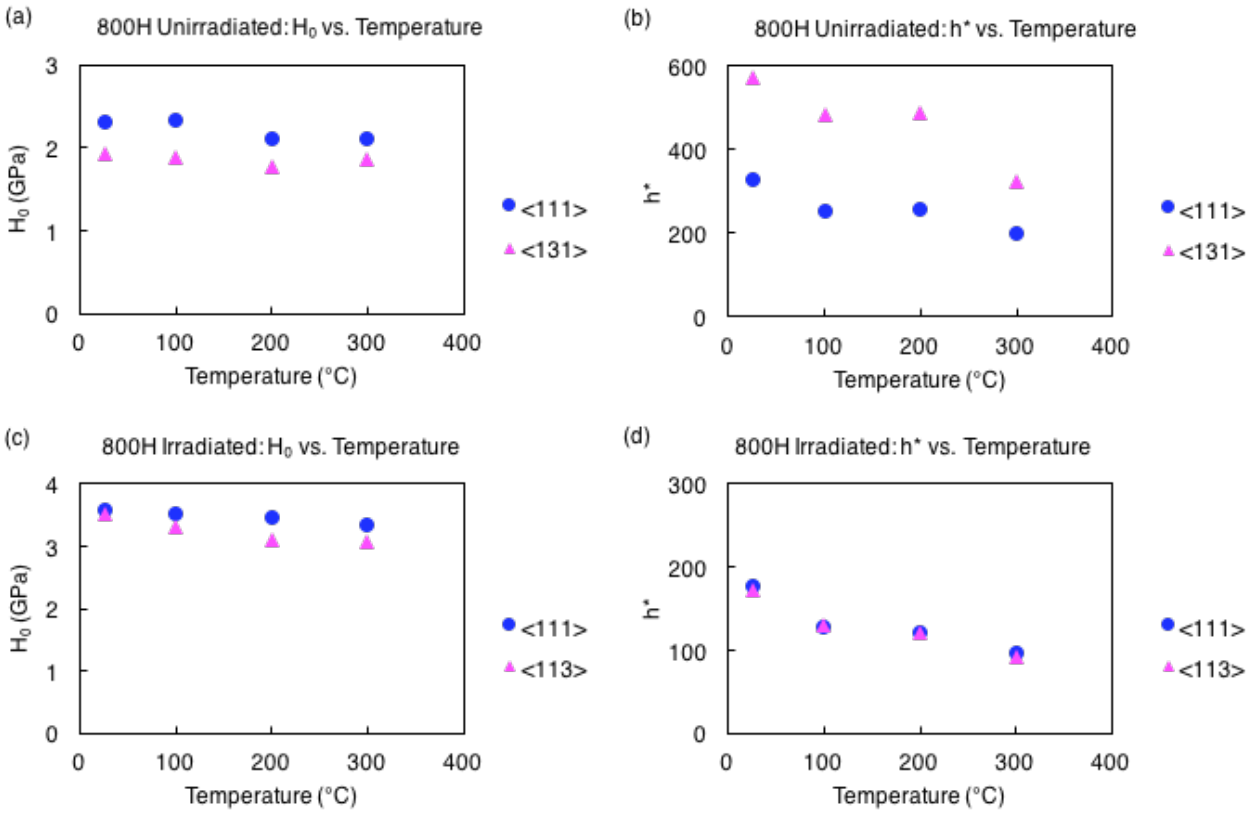

Figure 3.8 Nix and Gao model for indentation size effect (ISE) study in unirradiated and irradiated 800H showing H_0 and h^* as a function of temperature.

Irradiated 800H

Hardness and modulus measurements of the unirradiated <111> and <113> oriented grains are provided in Figure 3.9 and Figure 3.10, respectively. Figure 3.11 represents an example of the hardness and reduced modulus measurement data as a function of indentation depth, along with the Nix and Gao plot (with R^2 equal to or above 85%), obtained from a grain orientation of <111> in the irradiated 800H at room temperature. Hardness profiles as a function of testing temperature for <111> and <113> grain orientations are shown in Figures 3.12(a) and 3.12(c), respectively. Since the irradiated 800H has a higher hardness value than the unirradiated 800H, the penetration depth is only approximately 350 nm with the maximum indenter load. At this depth, hardness decreases from 4.4 GPa at room temperature to 3.8 GPa at 300 °C in the <111> grain (14%) and from 4.4 GPa at room temperature to 3.4 GPa at 300 °C in the <113> grain (23%). Similar to the unirradiated 800H, the decreasing rate of hardness with penetration depth is different for each testing temperature, suggesting different size effect behaviors. Figures 3.12(b) and 3.12(d) provide the reduced modulus profiles as a function of temperature for the <111> and the <113> grains. At approximately 350 nm indentation depth, the reduced modulus drops from 215 GPa and 195 GPa at room temperature to 191 GPa and 178 GPa at 300 °C, which corresponds to 11% and 9% for the <111> grain and the <113> grain, respectively. H_0 and h^* are plotted over testing temperature in Figures 3.8(c) and 3.8(d) for both grain orientations, and are tabulated in Table 3.1.

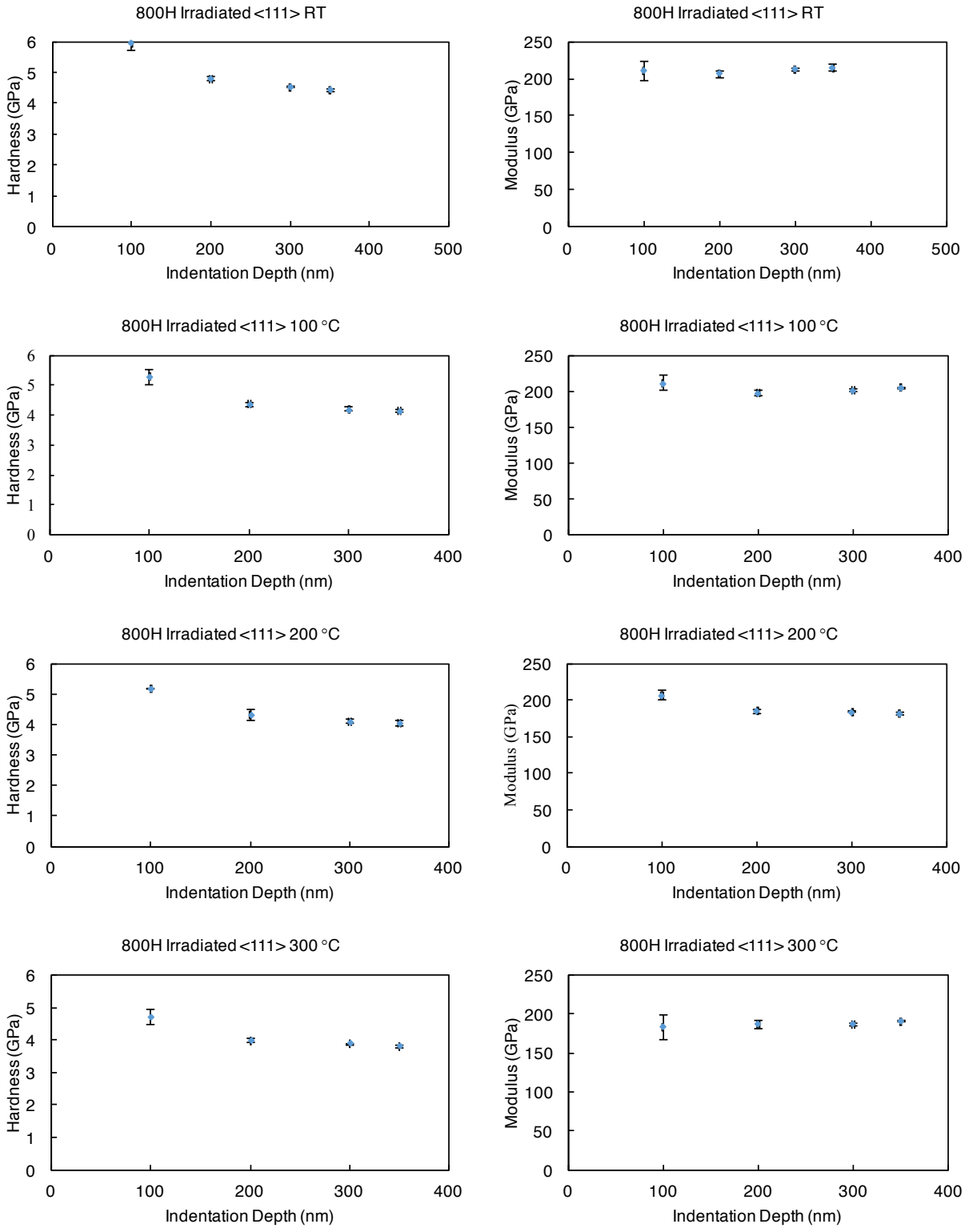

Figure 3.9 Hardness and modulus measurements of the unirradiated <111> 800H.

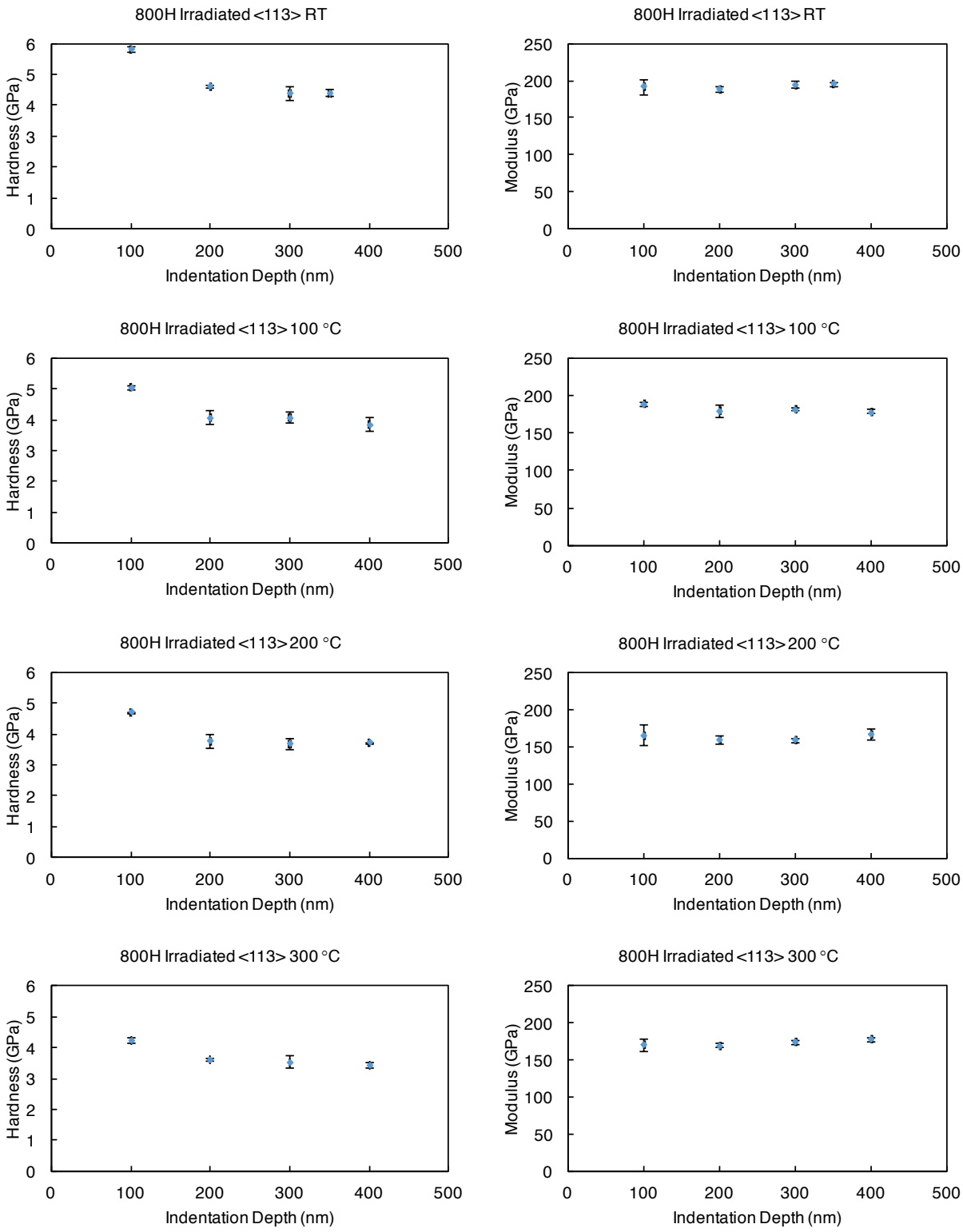

Figure 3.10 Hardness and modulus measurements of the unirradiated <113> 800H.

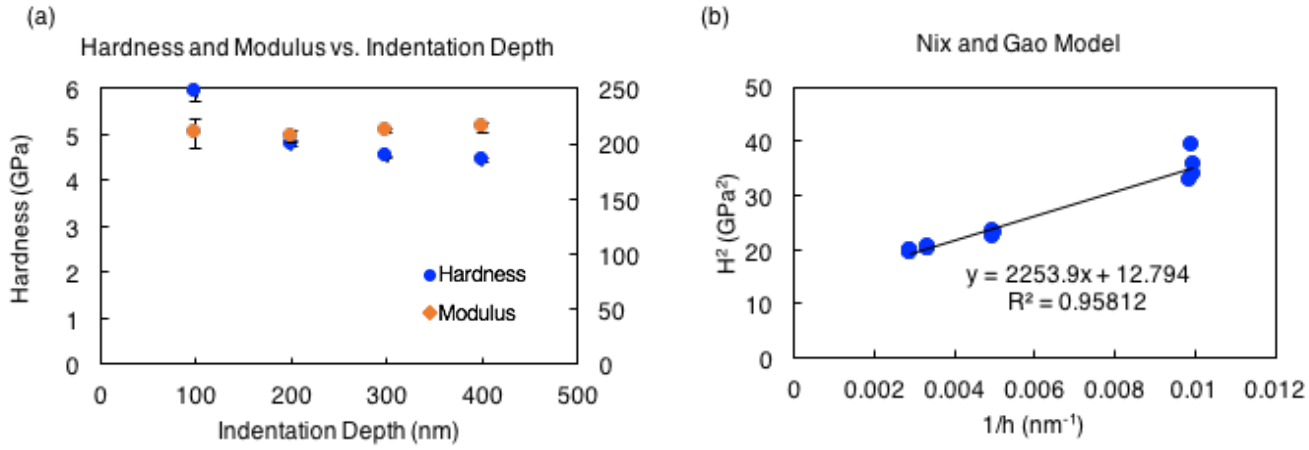

Figure 3.11 Irradiated 800H; <111> grain orientation at room temperature: Nanoindentation results (a) Hardness and reduced modulus as a function of indentation depth (b) Nix and Gao plot showing how indentation size effect is calculated.

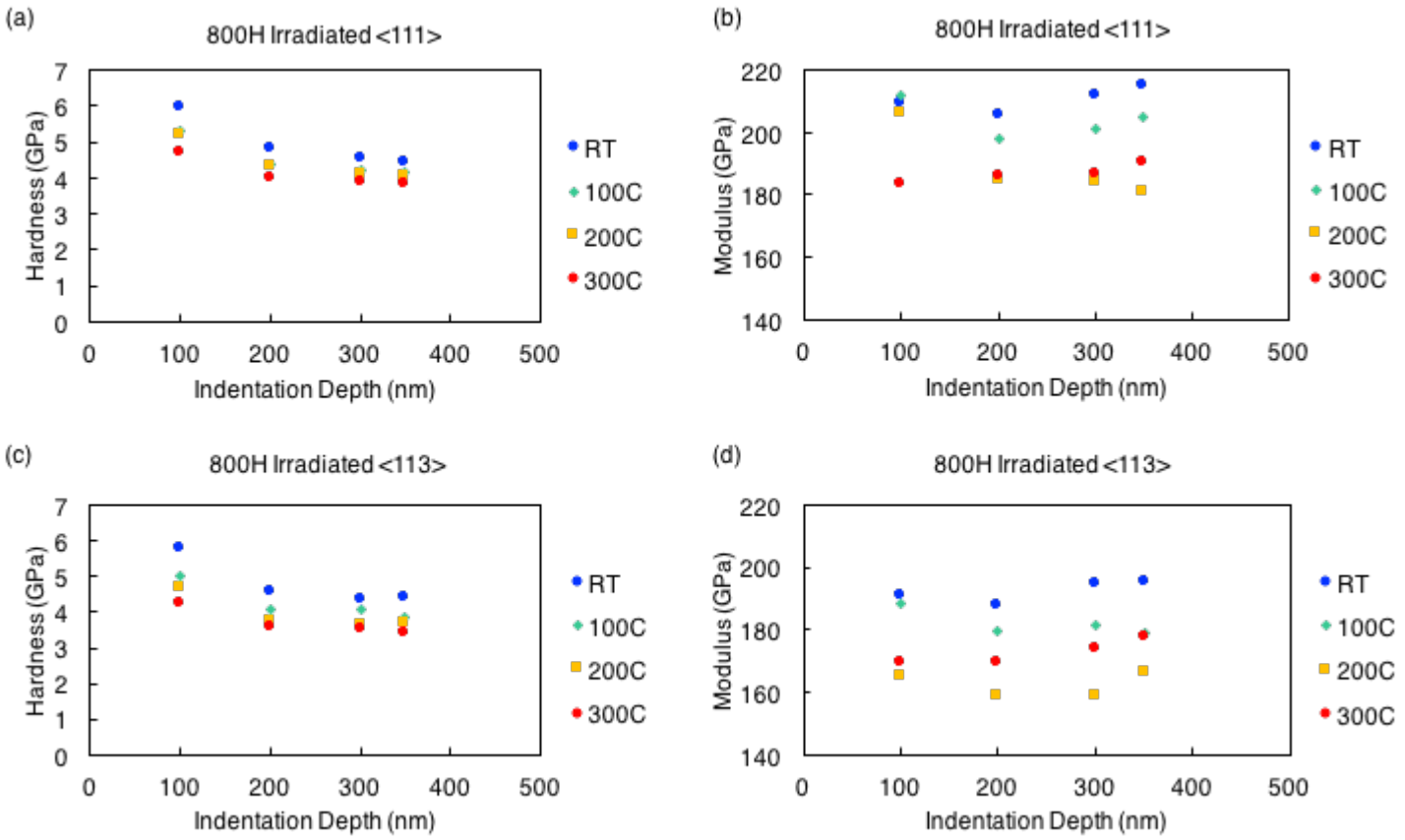

Figure 3.12 Irradiated 800H; Hardness and modulus profiles as a function of depth and temperature of grains of <111> and <113> orientations.

For comparison reasons, the hardness measurements from the <111> grain in the unirradiated 800H and that from the same grain orientation in the irradiated 800H were used for size effect studies over temperatures. Figure 3.13(a) compares the hardness profiles as a function of indentation depth of the unirradiated and the irradiated 800H. The differences in the hardness drop rates in the two samples suggests different amounts of indentation size effect. Figure 3.13(b) shows Nix and Gao plots obtained from the hardness data in Figure 8(a), illustrating less pronounced size effect after irradiation. The characteristic depth h* reduces from 327 nm to 176 nm after irradiation. h* values are plotted over temperatures in Figure 8(c). The h* are reduced by 38.8% from 327 nm to 200 nm for the unirradiated 800H and 44.9% from 176 nm to 97 nm for the irradiated 800H in the <111> grain orientation. Figure 3.14 shows the logarithmic relationship of the h* and temperature for both grain orientations in unirradiated and both in irradiated 800H. It is worth noting that while two grain orientations from the unirradiated 800H have different relationships, the two grains from the irradiated 800H follow very similar relationships. This implies the significantly reduced influence of grain orientation on indentation size effect behavior as a function of temperature after irradiation.

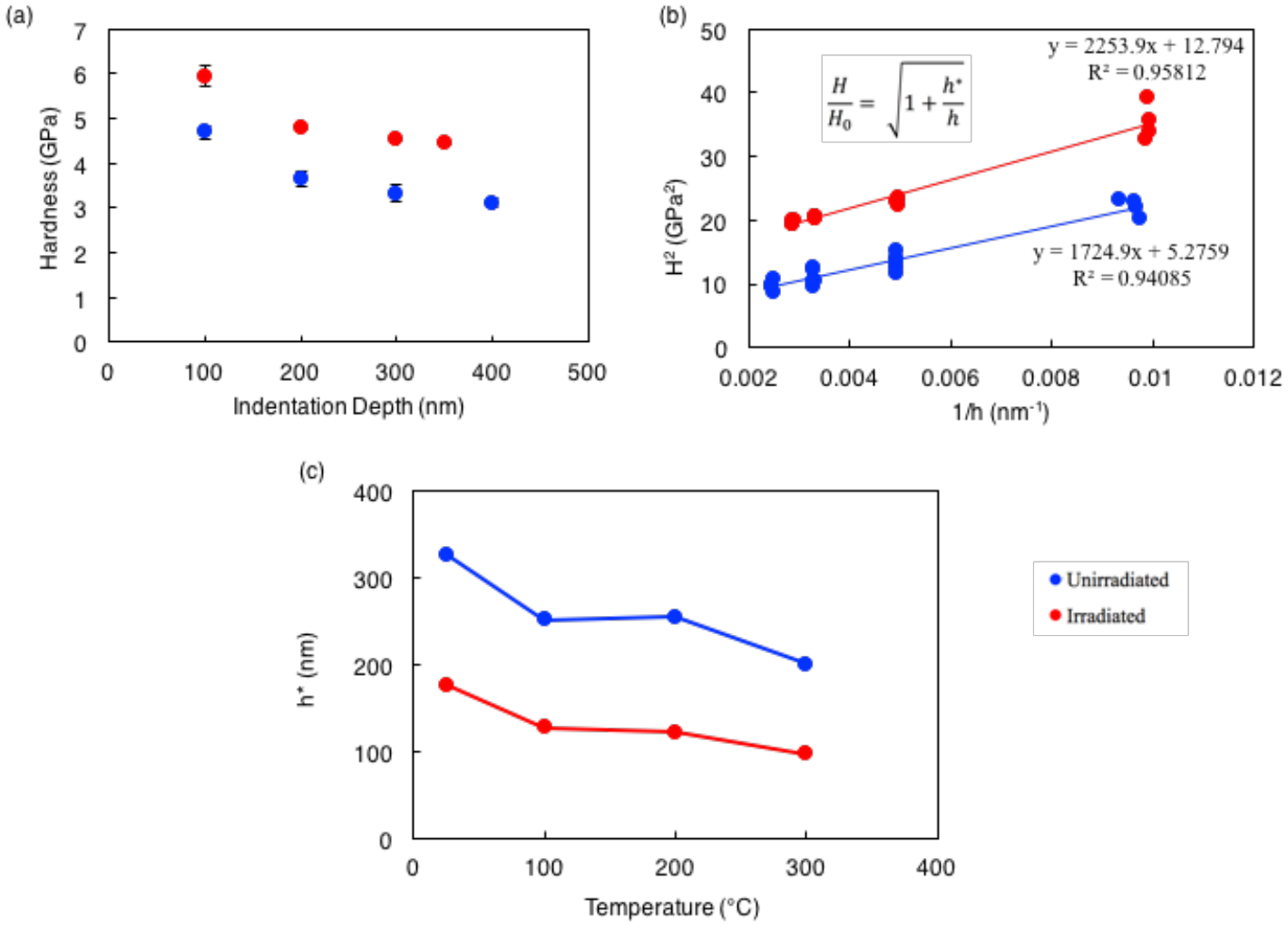

Figure 3.13 Comparisons between hardness profiles and indentation size effects in unirradiated and irradiated 800H.

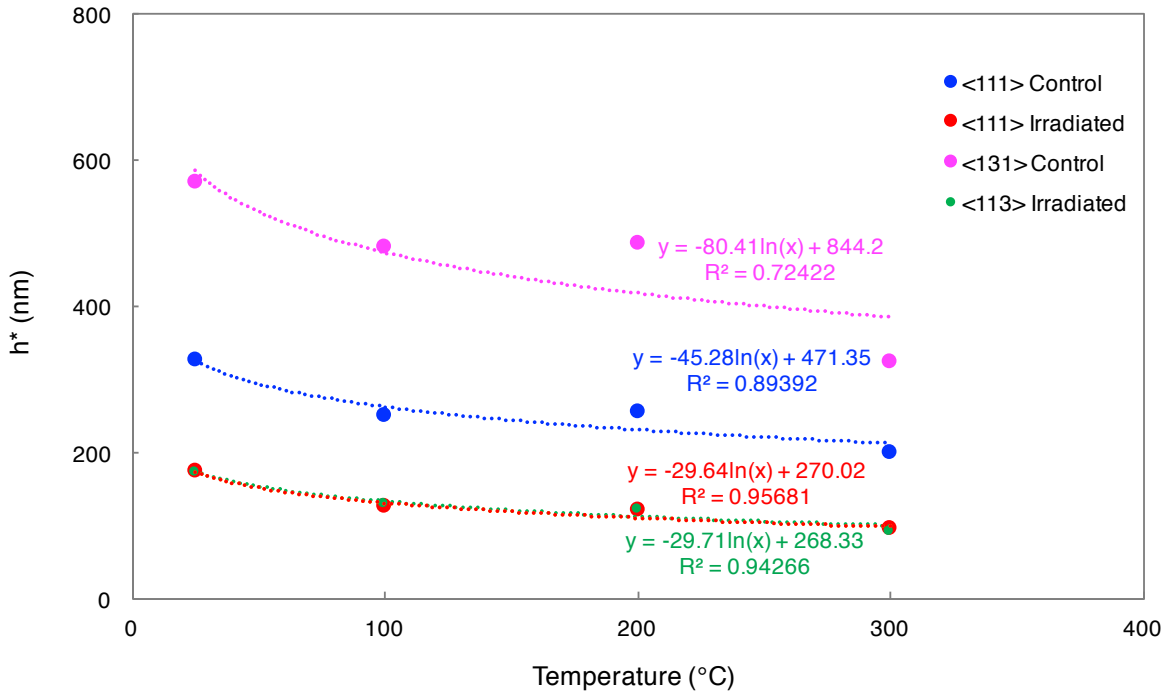

Figure 3.14 Logarithmic relationship of the h* and temperature for each grain orientation in unirradiated and irradiated 800H.

3.4 Influence of irradiation and temperature on ISE

In the work on ISE of single crystal Cu at room temperature by Durst et al. and Backes et al. [61,92-93], the calculated h^* values from single-crystal samples varied from 200-700 nm, depending on crystal orientation. The wide range of h^* suggested that orientation has a strong influence on ISE. However, the study of the influence of crystal orientation on indentation size effect has not been performed. To exclude orientation dependence, grain orientations were identified and taken into account in this study. For both the unirradiated and the irradiated 800H, different grain orientations result in different hardness, reduced modulus and h^*. Flom et al. [144] reveals significant anisotropy in the hardness which is characteristic to different crystal orientations where the anisotropy arises from different numbers and orientations of active slip systems during an indentation [145]. The plastically deformed volume underneath the indenter can be correlated to where slip on the preferred planes and directions occur [144-145]. This is due to the distributions of dislocations unique to specific orientations [146], emphasizing that grain orientations must be specified when studying ISE in large grained materials or single crystals.

Although the modulus data do not contribute to the size effect studies, they serve as a tool to ensure the accuracy of the hardness data. Table 3.2 provides the comparisons between the unirradiated and the irradiated 800H. For the <111> grain orientation, the increases in hardness after irradiation is due to the radiation damage (radiation-induced defects) caused by ion-irradiation [56,147-150]. Studies have shown that ISE is weak if not absent for materials with pre-existing high dislocation densities and defects (high density of SSDs) [92, 146, 151] since the deformation is not dislocation

source limited but rather dislocation mobility (defect interaction) limited. A similar case was also observed in Cu nanopillars [152] where only very small volumes tested experience a size effect on irradiated materials.

Table 3.2 Comparisons between the unirradiated and irradiated 800H

RT → 300 ˚C	Unirradiated 800H		Irradiated 800H	
h*	<111>	327 nm → 200 nm	<111>	176 nm → 97 nm
	<131>	571 nm → 324 nm	<113>	172 nm → 91 nm
f	<111>	↑18%	<111>	↑22%
	<131>	↑21%	<113>	↑24%
H_0	<111>	↓8%	<111>	↓6%
	<131>	↓4%	<113>	↓13%
Modulus	<111>	↓9%	<111>	↓11%
	<131>	↓11%	<113>	↓9%

In agreement with the aforementioned studies, the ISE in the <111> grain tested here in the irradiated 800H is less significant than that of the same grain orientation in the unirradiated 800H. This originates from the fact that the radiation-induced defects causing radiation damage act as dislocation obstacles, thus increasing flow stress through the material as also discussed in [152].

As shown in the results, at the same penetration depth, hardness decreases with increasing temperature in all cases (unirradiated and irradiated). This is expected but the more interesting observation is that the ISE is also less pronounced with increasing temperature for every grain orientation in both the unirradiated and the irradiated 800H. Increasing temperature decreases shear modulus and lattice friction or Peierls stress, and increases dislocation mobility [94], resulting in the larger plastic zone size for GNDs storage and thus the larger scaling factor *f*, which scales with the radius of the plastically deformed volume (schematic shown in Figure 3.15) [153]. From Equation 1.7, since H_0 scales linearly with shear modulus G (Equation 1.8), h^* is only dependent upon f while other parameters are constant, with the assumption that the dislocation density remains relatively constant with temperature and no significant defect structure change occurs in the temperature regime of interest. Accordingly, ISE are less significant at high temperatures due to the larger GND storage volume i.e. plastic zone size.

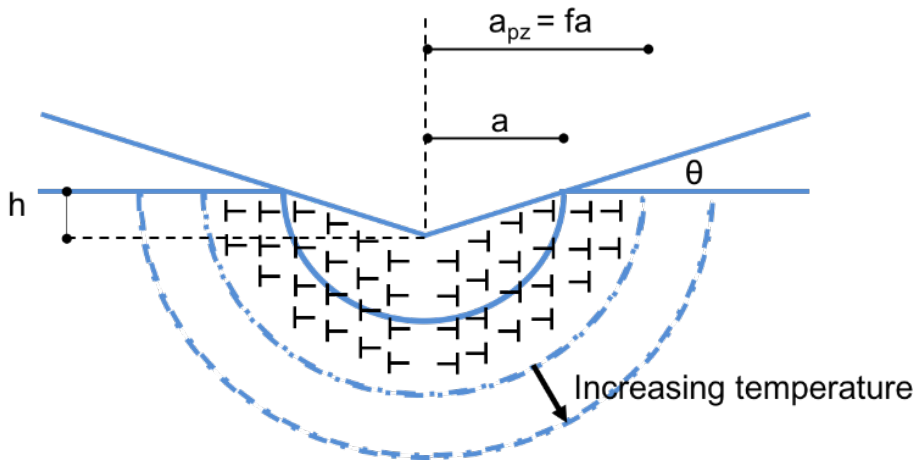

Figure 3.15 Schematic of the temperature influence on GND storage volume.

The assumption that the defect density is not changing in the temperature regime evaluated here is valid for both the unirradiated and the irradiated 800H because the maximum testing temperature stays well below the irradiation temperature. Therefore, all effects observed are due to the dislocation defect interaction and not due to the change of defect density as a function of temperature. The data suggests that h^* is also significantly reduced on the irradiated material as temperature increases i.e. ISE is even less pronounced. Again, if we assume the radiation induced defects do not change as a function of temperature one may conclude that for the irradiated material the plastic zone size is increasing as a function of temperature and therefore a higher density of SSDs become available.

Another aspect of this discussion can be brought in if one considers the fact that irradiated materials deform differently than unirradiated materials. Some irradiated materials tend to form defect free slip channels (dislocation channeling) rather than ordinary plastic deformation leading to highly localized slip where the mobile dislocations absorb the smaller radiation induced defects in the material leaving areas of reduced defect density behind [154-156]. However, it is still unclear whether dislocation channeling actually occurs under the indenter [154]. Without dislocation channeling, radiation-induced defects result in a higher density of existing SSDs after irradiation and therefore contribute to less pronounced ISE in the same manner as that of unirradiated, cold-worked materials. Nevertheless, if the assumption that irradiated materials deform through dislocation channeling during indentation holds, one could assume that that the plastic deformation is highly localized and the hardness measured at a specific condition (depth and temperature) is not based on GNDs but rather on the development of these slip channels. Thus, the Nix and Gao model could no longer be used in the case of irradiated materials.

Higher temperatures assist dislocations in overcoming the activation barriers to dislocation-defect interactions and therefore would cause more softening as a function of temperature in the irradiated material than what is observed in the unirradiated material. The evidence for this phenomenon is illustrated by the decrease in the difference in the average hardness between the unirradiated grain (0.82 GPa) and the irradiated grain (0.67 GPa) of the same orientation with increasing temperature (see Figure 3.16). As mentioned previously, there has been only a single study on the influence of

temperature on ISE by Franke et al. [94]. In Franke's study, from room temperature to 200 °C, h^* of the single crystal Cu (unknown grain orientation) decreases significantly from 280 nm to 83 nm. Current results confirm the less pronounced size effect at higher temperatures for all grain orientations in both samples: from 327 nm to 255 nm in the <111> grain and from 571 nm to 487 nm in the <131> grain in the unirradiated 800H, also from room temperature to 200 °C. The most original and novel finding of the current work, however, is the suggestion of a strong influence of crystal orientation on ISE. In other words, this work pioneers the independent influence of crystal orientation, irradiation conditions and temperature on ISE. Table 3.3 compares the results from Franke's study to the current study. The increase in the storage volume, measured by the parameter f, at high temperatures is observed in both cases, although in Cu the percent increase is significantly higher. While the bulk hardness of Cu remains roughly constant, the bulk hardness in both grain orientations of 800H decreases with temperature. The same trend is also observed for reduced modulus in 800H.

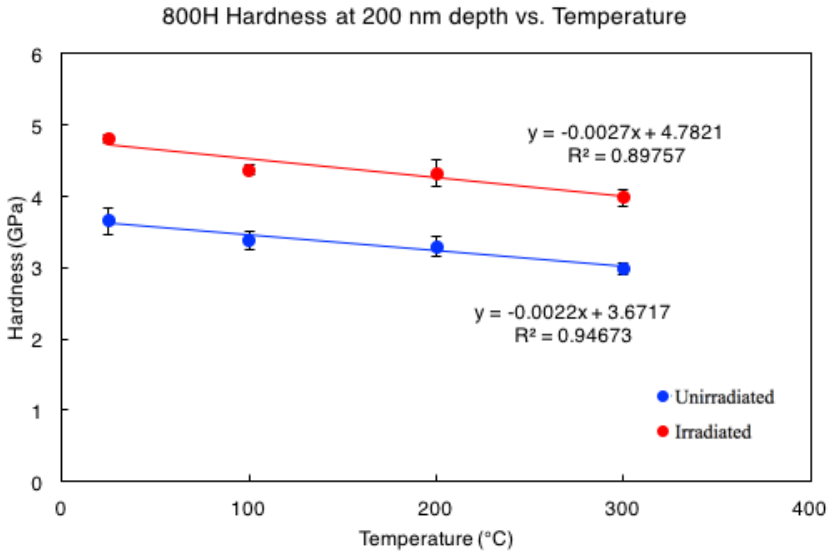

Figure 3.16 Hardness at 200-nm indentation depth as a function of temperature for both unirradiated and irradiated <111>.

Table 3.3 Comparisons with literature: Franke's study [94]

RT → 200 ˚C	Franke's study	Current study	
Material	Single crystal Cu	<111> 800H	<131> 800H
h*	280 nm → 83 nm	327 nm → 200 nm	571 nm → 324 nm
f	↑44%	↑7%	↑4%
H_0	Roughly constant	↓8%	↓8%
Modulus	N/A	↓10%	↓12%

Chapter 4

Sample Size Effect (SSE) in Microcompression

Despite the extensive sample size effect studies of both BCC and FCC metals at room temperature, the influence of temperature on sample size effect has only been investigated and understood in BCC metals [106,157] but not FCC metals. In order to understand the influence of irradiation and temperature on sample size effects observed in FCC metals, the austenitic alloy 800H steel (31.6Ni-20.4Cr-45.5Fe (wt%)) has been chosen for investigation due to its potential use as a structural material in nuclear reactors. Alloy 800H has superior mechanical properties due to its high nickel and chromium content, making it a strong candidate structural material for high temperature and nuclear applications [38]. Micro-pillars of different sizes for microcompression testing experiments at ambient and at 300 °C were fabricated in the same grain containing both the unirradiated and the ion-irradiated areas for comparison reasons.

4.1 Experimental

Electron Backscattered Diffraction (EBSD) was used to identify a large grain containing both the unirradiated and the irradiated areas for micro-pillar fabrication in order to eliminate the influence of grain orientation and allow direct comparisons between the micro-pillars of different irradiation and compression conditions within the same grain. A grain of <111> orientation with the length of approximately 200 μm along the irradiated edge was chosen for the study. The grain was purposely chosen to An FEI Quanta dual beam scanning electron microscope and focused ion beam (FIB-SEM Dual-Beam) was used to fabricate micro-pillars with the dimensions of 2 μm x 2 μm x 4 μm, 1 μm x 1 μm x 2 μm and 0.5 μm x 0.5 μm x 1 μm for room temperature size effect study. Three micro-pillars of each size were fabricated. In the case of high temperature size effect study, only micro-pillars with the dimensions of 2 μm x 2 μm x 4 μm and 1 μm x 1 μm x 2 μm were manufactured. Four micro-pillars of each size were manufactured. The detailed procedures for micro-pillar fabrication follow the steps outlined by Kiener et al [109]. In situ uniaxial compression was performed utilizing a Hysitron PI-85 pico-indenter at room temperature and a Hysitron PI-88 pico-indenter at 300 °C on the SEM-FIB manufactured pillars in the depth-controlled mode at the displacement rate of 10 nm/s using an indenter with a flat tip to obtain stress-strain curves for yield stress calculations [55].

4.2 Results

Load-displacement data were obtained from microcompression testing of micro-pillars at room temperature (Hysitron PI-85 pico-indenter) and at 300 °C (Hysitron PI-88 pico-indenter). Images of representative post-compression unirradiated and irradiated 800H micro-pillars and associated engineering stress-strain curves obtained from microcompression testing at room temperature are illustrated in Figure 4.1 and Figure 4.2, respectively. Similarly, Figure 4.3 and Figure 4.4 provides images and associating engineering stress-strain curves of unirradiated and irradiated micro-pillars compressed at 300 °C. The images of the compressed micro-pillars are representative of each of the dimensions tested. The corresponding stress-strain curves are plotted next to each of the

representative micro-pillars for comparison. Figure 4.5 and Figure 4.6 provides average values of the unirradiated and the irradiated 800H micro-pillars, respectively, both at room temperature and at 300 °C. Conducting microcompression tests in an *in situ* manner allows direct observations of the deformation behaviors of the unirradiated versus irradiated micro-pillars. Despite testing temperature, unirradiated micro-pillars deformed via multiple slips while irradiated micro-pillars undergo a single or a few slip events without activating new slip planes. The slip events observed real-time during microcompression experiments correspond to the load drops in the resulting stress-strain curves. Due to significantly less amount of drifts, the engineering stress-strain curves obtained from the micro-pillars compressed at room temperature are significantly smoother than those obtained at 300 °C.

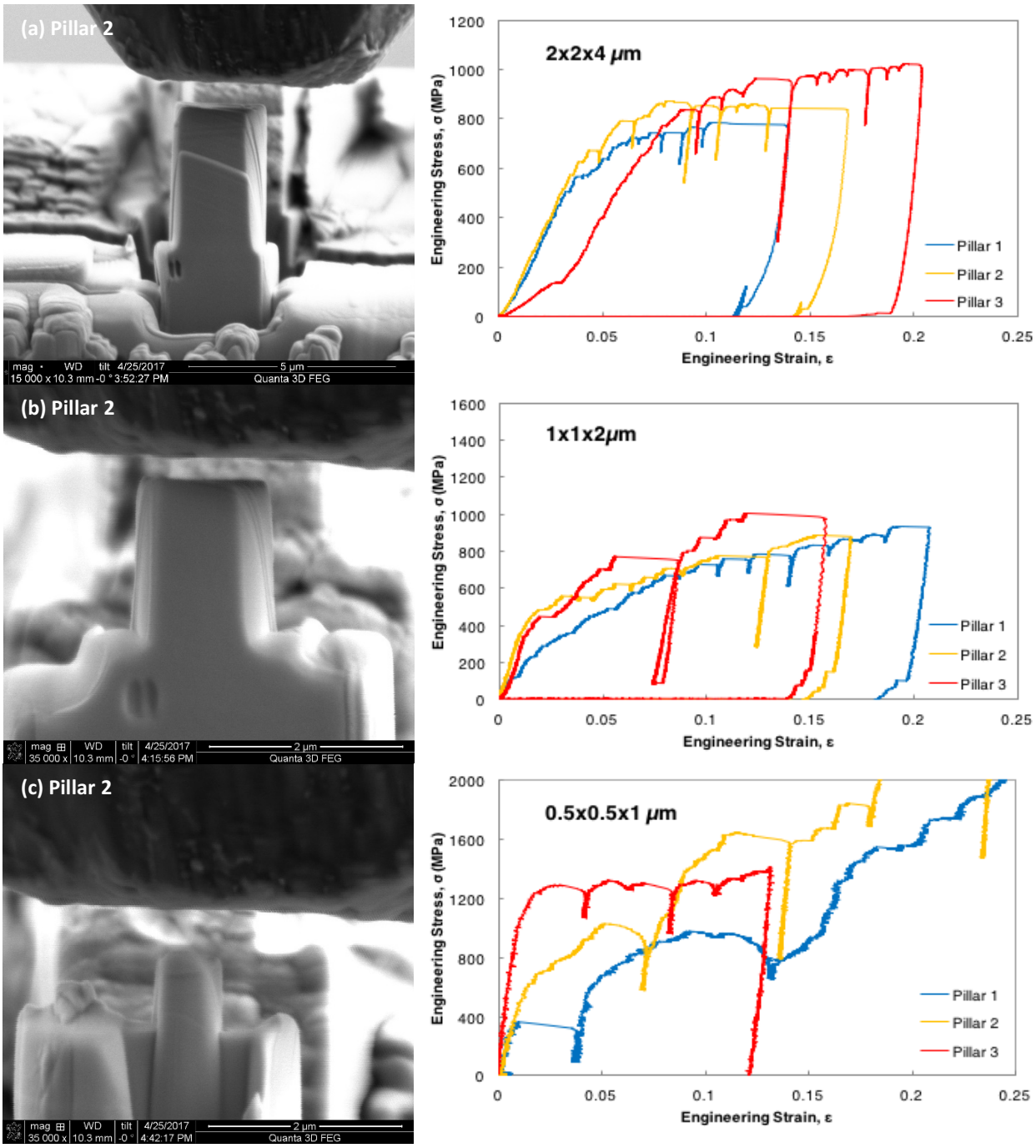

Figure 4.1 Compressed unirradiated 800H micro-pillars and associated stress-strain curves obtained from microcompression testing at room temperature (a) 2x2x4 µm (b) 1x1x2 µm (c) 0.5x0.5x1 µm.

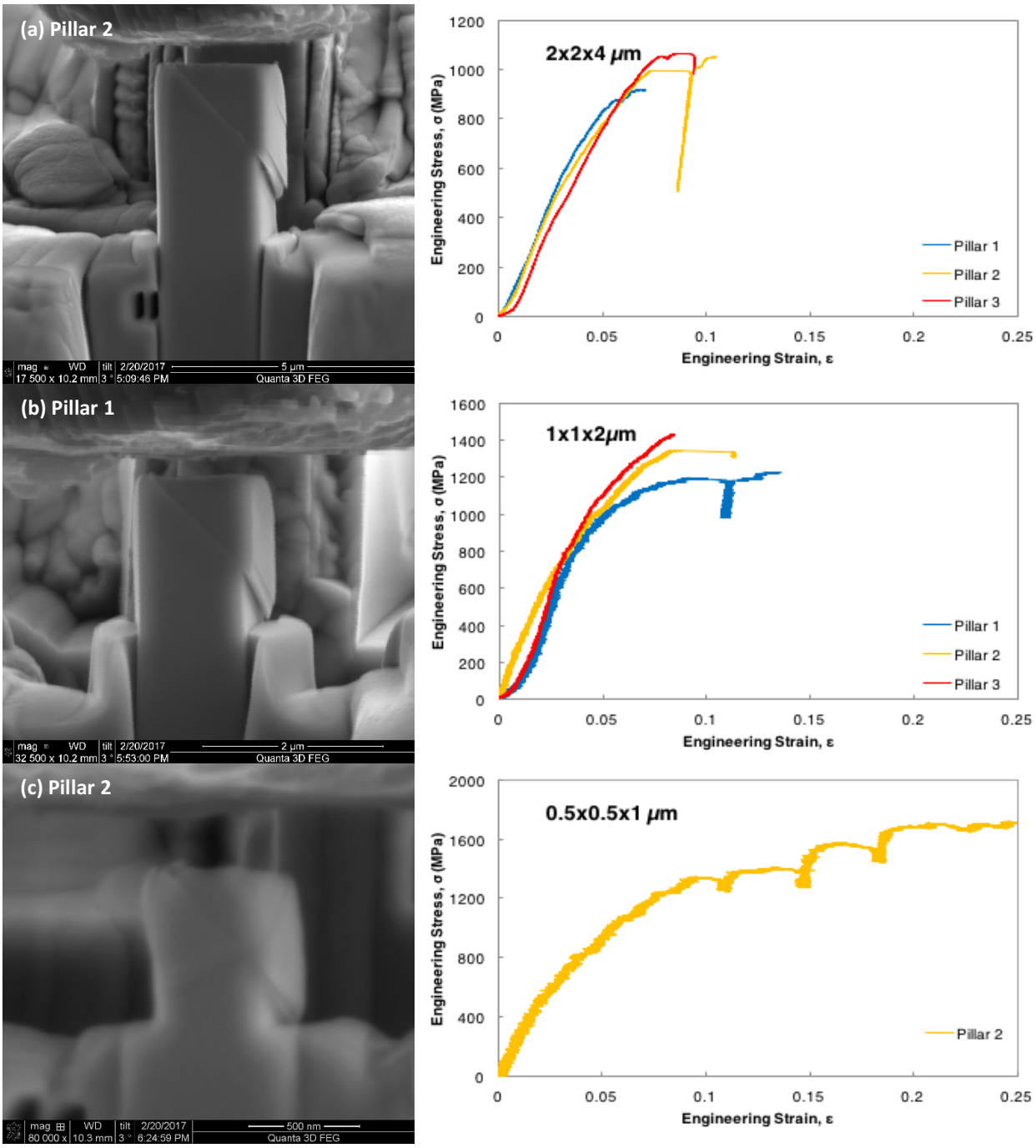

Figure 4.2 Compressed irradiated 800H micro-pillars and associated stress-strain curves obtained from microcompression testing at room temperature (a) 2x2x4 μm (b) 1x1x2 μm (c) 0.5x0.5x1 μm.

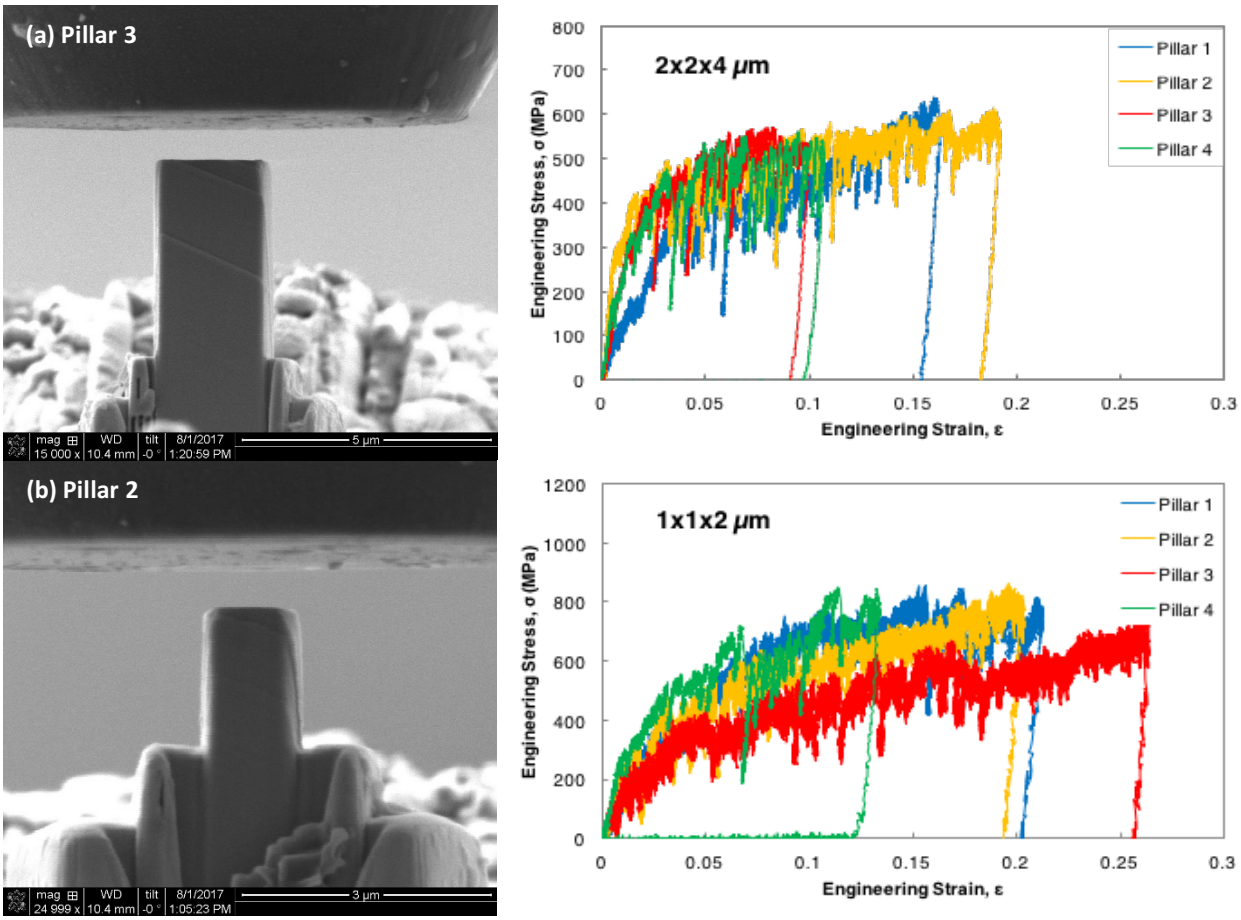

Figure 4.3 Compressed unirradiated 800H micro-pillars and associated stress-strain curves obtained from microcompression testing at 300 °C (a) 2x2x4 µm (b) 1x1x2 µm.

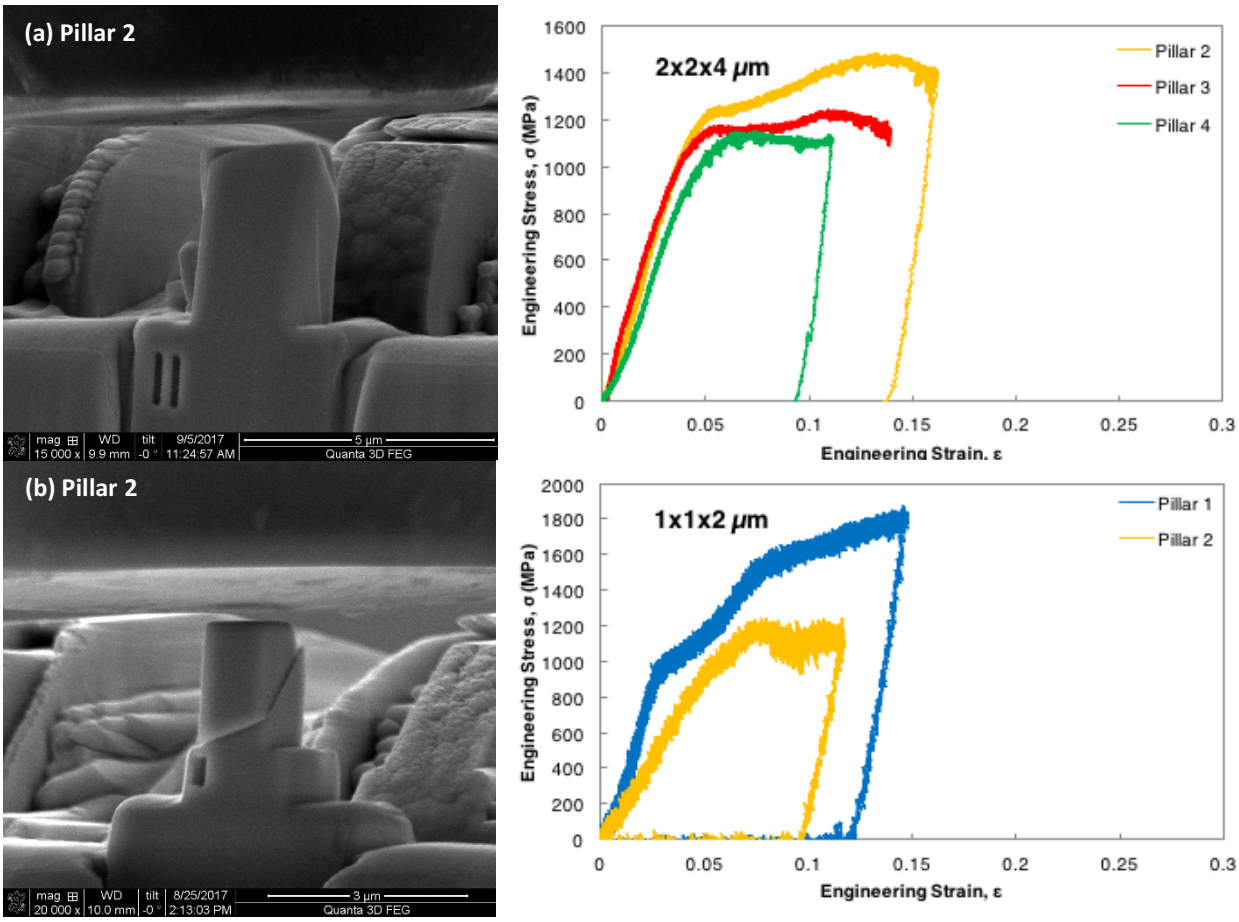

Figure 4.4 Compressed irradiated 800H micro-pillars and associated stress-strain curves obtained from microcompression testing at 300 °Cs (a) 2x2x4 µm (b) 1x1x2 µm.

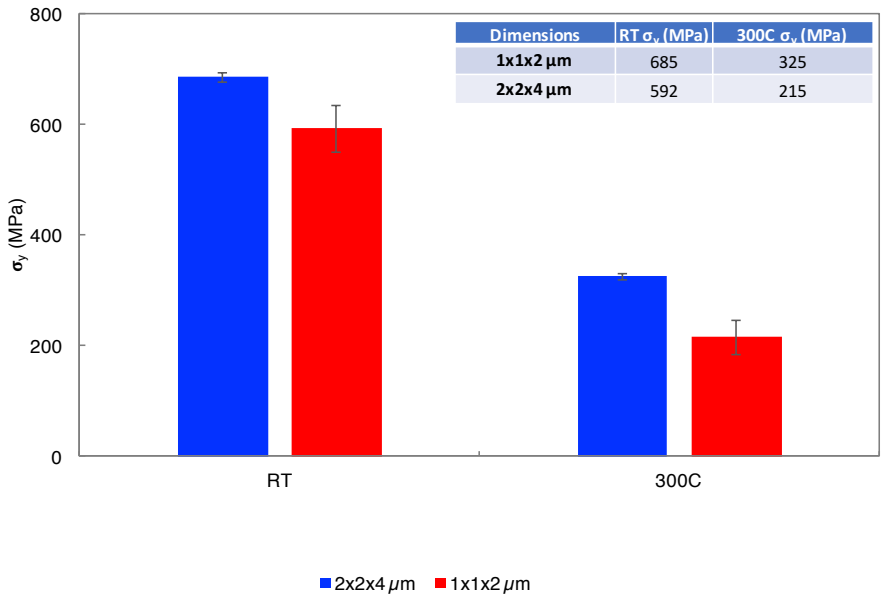

Dimensions	RT σ_y (MPa)	300C σ_y (MPa)
1x1x2 μm	685	325
2x2x4 μm	592	215

Figure 4.5 Average values of the unirradiated micro-pillars at room temperature and at 300 °C.

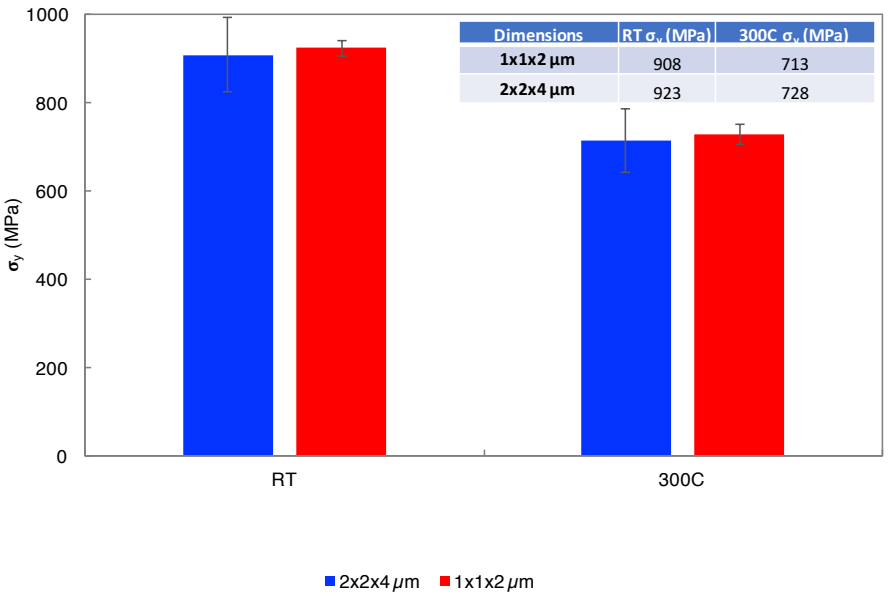

Dimensions	RT σ_y (MPa)	300C σ_y (MPa)
1x1x2 μm	908	713
2x2x4 μm	923	728

Figure 4.6 Average values of the irradiated micro-pillars at room temperature and at 300 °C.

Taking the surface interactions between the tip and the micro-pillars into account, a 0.2% strain line parallel to the elastic region was plotted to obtain the offset yield point. Variation in yield stresses can be observed from micro-pillars of different grain orientations due to different shear stresses necessary to activate slip planes and initiate plastic deformation. Such differences could

be eliminated by using Equation 4.1 to convert yield stresses to critical resolved shear stresses, which are characteristic to grain orientations. Since 800H has an austenitic crystal structure, the slip systems of 800H are {111}<110> i.e. {111} family of planes and <110> family of directions. A grain of [111] orientation in FCC crystals has a relatively low Schmid factor where multiple possible slip systems available [158]. The maximum value of the Schmid factor for [111] loading direction is 0.272, corresponding to the slip systems (11-1)[101], (1-11)[110], (-111)[110] and (-111)[101]. The yield stresses and the critical resolved shear stresses of the successfully compressed micro-pillars fabricated in the unirradiated and the irradiated area of the 800H alloy are provided in Table 4.1 (room temperature) and Table 4.2 (300 °C). Data from micro-pillars with possible experimental errors such as imprecise dimensions and misalignment during *in situ* compression are excluded from the tables. In this work yield stresses can be conveniently compared between micro-pillars of different irradiation conditions and compression temperatures because all experiments were performed on micro-pillars manufactured in the same grain.

$$\tau = \sigma_y (cos\varphi cos\lambda)_{max} \qquad \text{(Eqn. 4.1)}$$

where τ = shear stress, σ_y = yield stress, φ = angle between the slip plane normal and loading direction (compression axis) and λ = angle between the slip direction and loading direction (compression axis)

The average yield stress of unirradiated micro-pillars of the largest dimensions of 2x2x4 μm at room temperature is 592 MPa, which is over three times of the commercially reported bulk alloy 800H yield stress of 150 MPa [143]. This implies the existence of sample size effect phenomenon. Microcompression testing revealed significantly higher yield stresses in irradiated micro-pillars. Yield stresses of micro-pillars of the same irradiation conditions and dimensions decreases with temperature. Sample size effect phenomenon where strength (i.e. yield stress) increases with decreasing size is observed in the unirradiated micro-pillars, regardless of testing temperatures. Sample size effect is more significant in the unirradiated micro-pillars at 300 °C. In the case of irradiated micro-pillars, there is no size effect both at room temperature and at 300 °C.

Table 4.1 Yield stresses and critical resolved shear stresses (CRSS) of unirradiated and irradiated micro-pillars compressed at room temperature

Unirradiated	RT	σ_y (MPa)	σ_{CRSS} (MPa)	Irradiated	RT	σ_y (MPa)	σ_{CRSS} (MPa)
	Pillar 1	570	155		Pillar 1	850	231
	Pillar 2	630	171		Pillar 2	995	271
2x2x4 μm	Pillar 3	575	156	**2x2x4 μm**	Pillar 3	925	252
	Average	592	161		Average	923	251
	Std Dev	33.3	8.96		Std Dev	72.5	20
	Pillar 1	685	186		Pillar 1	850	231
	Pillar 2	665	181		Pillar 2	1000	272
1x1x2 μm	Pillar 3	705	192	**1x1x2 μm**	Pillar 3	875	238
	Average	685	186		Average	908	247
	Std Dev	20	5.51		Std Dev	80.4	21.9
	Pillar 1	960	261		Pillar 1	N/A	N/A
	Pillar 2	1025	279		Pillar 2	1050	286
0.5x0.5x1 μm	Pillar 3	1075	292	**0.5x0.5x1 μm**	Pillar 3	N/A	N/A
	Average	1020	277		Average	N/A	N/A
	Std Dev	57.5	15.6		Std Dev	N/A	N/A

Table 4.2 Yield stresses and critical resolved shear stresses (CRSS) of unirradiated and irradiated micro-pillars compressed at 300 °C

Unirradiated	300 °C	σ_y (MPa)	σ_{CRSS} (MPa)	Irradiated	300 °C	σ_y (MPa)	σ_{CRSS} (MPa)
2x2x4 μm	Pillar 1	170	46.2	2x2x4 μm	Pillar 1	N/A	N/A
	Pillar 2	260	70.7		Pillar 2	705	192
	Pillar 3	240	65.3		Pillar 3	750	204
	Pillar 4	190	51.7		Pillar 4	730	199
	Average	215	58.5		Average	728	198
	Std Dev	42	11.4		Std Dev	22.5	6.03
1x1x2 μm	Pillar 1	315	85.7	1x1x2 μm	Pillar 1	725	197
	Pillar 2	295	80.2		Pillar 2	700	190
	Pillar 3	370	101		Pillar 3	N/A	N/A
	Pillar 4	320	87		Pillar 4	N/A	N/A
	Average	325	88.5		Average	713	194
	Std Dev	31.9	8.85		Std Dev	17.7	4.95

4.3 Discussion and the influence of irradiation and temperature on SSE

One of the major drawbacks of microcompression testing is the extensive and costly sample fabrication process involving the use of FIB-SEM dual-beam machining. However, compared to other uniaxial small-scale mechanical testing techniques such as tensile testing, sample preparation in microcompression testing is relatively less complicated and less time-consuming. The presumably uniaxial stress state characteristic of microcompression testing allows significantly more straightforward data interpretation compared to triaxial stress state observed in indentation testing [159]. Nevertheless, it is worth noting that the two testing techniques are comparable despite the discrepancies between their stress state natures. The difference in yield stresses of the <111> grain before and after irradiation obtained from indentation at 1000 nm penetration [150] and microcompression testing is illustrated in Figure 4.7. Yield stress from indentation testing was obtained by converting measured hardness data (Berkovich hardness H_b) to Vickers hardness (H_v) (Equation 4.2) then ultimately to yield stress (σ_y) (Equation 4.3) [150, 133]. After irradiation, the increase in the average yield stress of the largest micro-pillars with 2x2x4 μm dimensions is 331 MPa, which is comparable to the increase in the yield stress of 341 MPa calculated from indentation hardness measurements.

$$H_V \propto 94.5 H_b \qquad \text{(Eqn. 4.2)}$$

where H_V is Vickers hardness and H_b is Berkovich hardness

$$\sigma_y \propto 2.82 H_V - 114 \qquad \text{(Eqn. 4.3)}$$

where σ_y is yield stress

Microcompression and the fundamentals of deformation mechanisms in micro-pillars have been extensively studied [114]. It is worth noting that the reason for choosing the aspect ratio of micro-

pillars in this study to be 2:1 was to avoid plastic buckling, as plastic deformation through slip events are of interest in investigating sample size effect [70,160]. Comparing micro-pillars of the same size, larger yield stresses are observed in irradiated micro-pillars. This is due to hardening by irradiation-induced faulted loops which hinder dislocation motions, resulting in higher stress required for slip events to occur [38,161].

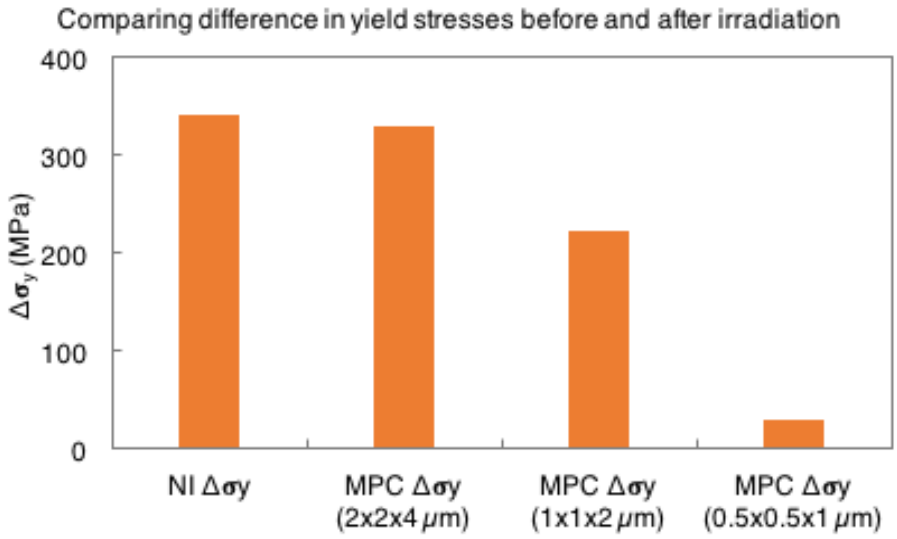

Figure 4.7 Comparison between the difference in yield stresses of the <111> grain before and after irradiation obtained from nanoindentation and microcompression testing.

A fewer number of load drops were visible in the engineering stress-strain curves of the irradiated micro-pillars than that of the unirradiated micro-pillars. In displacement controlled tests, load drops refer to dislocation activities i.e. slip events [162-163]. This suggests localized, heterogeneous deformation along a few, if not a single, slip planes activated during the compression of the irradiated micro-pillars, implying dislocation channeling which is commonly observed in irradiated alloys [155,164-165]. A power-law dependence of yield stress on micro-pillar diameter (the width of the cross section in this case) is illustrated in Equation 4.4 and shown in Figure 4.8 [166]. Sample size effect is remarkably less pronounced and become non-existent in the irradiated micro-pillars where $n = 0.09$ versus in the unirradiated counterparts where $n = 0.39$, which agrees well with the previous studies where sample size effect is dependent on initial dislocation density i.e. size effect is less pronounced as initial dislocation density is increased [167].

$$\sigma_y \propto Ad^{-n} \qquad \text{(Eqn. 4.4)}$$

where σ_y is yield stress, A is a constant, d is micro-pillar diameter or size, n is the power law exponent

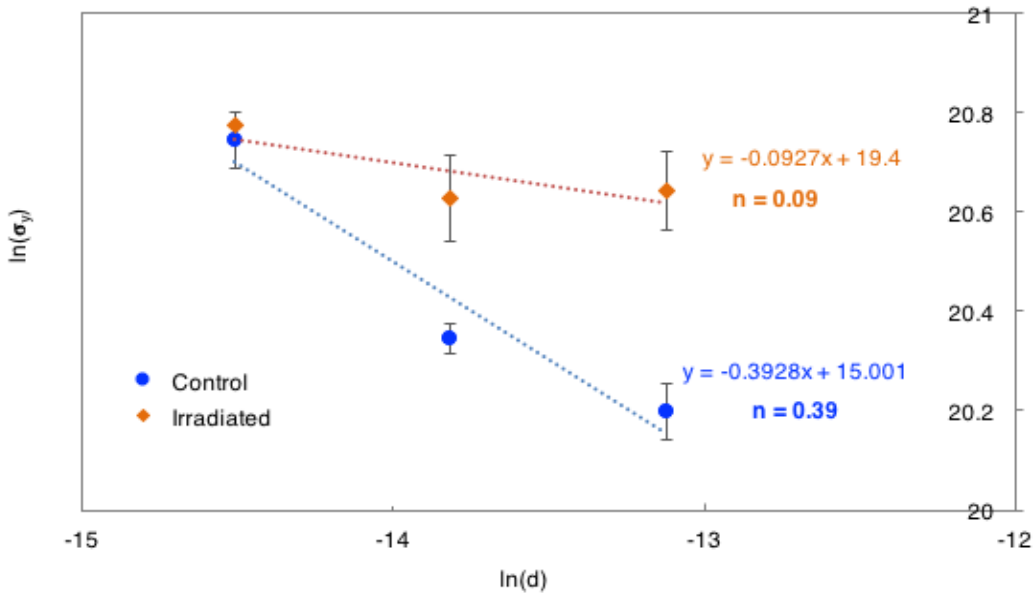

Figure 4.8 Sample size effect studies of the unirradiated and irradiated micro-pillars compressed at room temperature (the smallest micro-pillar dimensions is 0.5x0.5x1 μm).

In microcompression testing, Sample size effect is caused by the relative influences of the size-independent (lattice stress τ_0 and dislocation forest hardening $0.5Gb\sqrt{\rho_{tot}}$) and size-dependent components (single-ended source activation $\frac{\alpha Gb}{L}$) of the critical resolved shear stress τ_{CRSS} in Equation 1.9. Considerable size effect in unirradiated 800H micro-pillars is resulted from the more contribution of the size-dependent term to τ_{CRSS}. This may be due to the lower τ_0 in FCC crystals and the low ρ_{tot}. Heavy-ion irradiation results in a large number of dislocations into the matrix, increasing the total dislocation density. The increased dislocation density strains the material and thus raises lattice stress, leads to smaller dislocation spacing, and increases dislocation forest hardening stress, all of which contribute to the size-independent term being more dominant. Accordingly, no size effect is observed in irradiated 800H micro-pillars. Moreover, when the dislocation density is so large that dislocation spacing is reduced to the sample dimension regime, L in Equation 1.9 is referred to irradiation-induced dislocation spacing instead of sample size, as dislocation spacing refers to the smallest microstructural dimension [157]. In that case, there is no sample size effect since all components constituting to the τ_{CRSS} are size-independent. Further investigation is needed in order to confirm the suggested possible reasons behind the reduced sample size effect after irradiation; however, this is out of the scope for this study.

The yield stresses from both unirradiated and irradiated 800H micro-pillars compressed at 300 °C are significantly lower than those obtained at room temperature. This is due to the lower lattice stress and the higher dislocation mobility at elevated temperatures. Nevertheless, the most novel discovery of this work is the influence of temperature on sample size effect in 800H micro-pillars: sample size effect is more pronounced at an elevated temperature. That is, n is 0.21 at room temperature and 0.61 at 300 °C, shown in Figure 4.9 (the smallest micro-pillar dimensions is 1x1x2

μm). This finding is in contrast to the study conducted by Wheeler et al. [168] on the size effect in annealed Cu micro-pillars (dimensions of 0.4-4 μm) as a function of temperature, which is the only study to date that has been done on high temperature sample size effect in FCC metals. Wheeler et al. concluded that since size-dependent term contributing to the critical resolved shear stress is athermal and the size-independent terms are negligibly affected by temperature compared to the magnitude of the size effect, sample size effect in FCC metals is constant with temperature up to almost half of the melting point. While this may hold true for annealed Cu in the work performed by Wheeler et al., this work performed on the austenitic alloy 800H argues that this assumption might not hold true across all FCC metals due to the fact that higher strength FCC metals might be more affected by temperature.

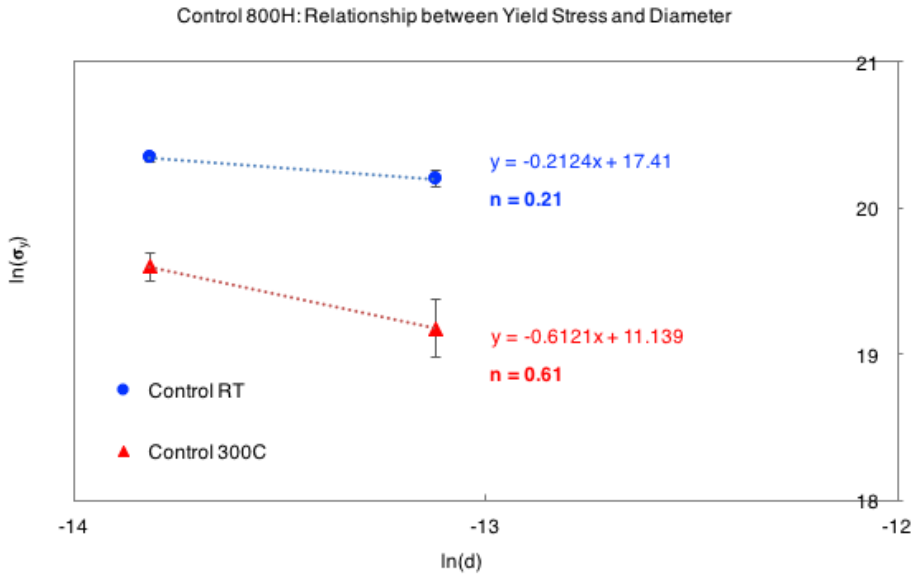

Figure 4.9 Influence of temperature on sample size effect in unirradiated 800H micro-pillars (the smallest micro-pillar dimensions is 1x1x2 μm).

An interesting observation is that while the power-law exponent n for FCC metals is in the range of 0.61-0.97 [71], the power-law exponent obtained from the unirradiated 800H micro-pillars is 0.39 (Figure 4.8), the smallest micro-pillar dimensions is 0.5x0.5x1 μm), which interestingly lies in the range of n = 0.21-0.48 for BCC metals where size effect is relatively small [71,166]. This suggests the possibility of unirradiated 800H having similar characteristics and therefore sample size effect behaviors to BCC metals. Increasing the temperature has different influences on different stresses contributing to the critical resolved shear stress for single-arm dislocation activation to plastic deformation in micro-pillars. As temperature increases, Burgers vector increases, shear modulus and lattice stress decrease, and the total dislocation density remains constant in this work as the sample had been held at the irradiation temperature well above the test temperature for an extended period of time. The change temperature has on Burgers vector is relatively trivial due to the length scale of angstroms. Therefore, it can be concluded that sample size effect is either constant or more significant at higher temperatures, depending on the strength of the micro-pillars, regardless of crystal structure. A possible explanation of the more pronounced size effect at 300 °C in unirradiated 800H micro-pillars is due to the higher lattice stress of the material despite negligible lattice stress in most FCC metals [71]. In BCC micro-pillars, size effect

scales with the influence of lattice resistance on yield stress measured by the ratio of the test temperature to the critical temperature of a BCC metal micro-pillars are made of [157,166]. When temperature has its most influence on the size-independent lattice resistance, size effect is therefore undoubtedly more significant. In the case of the irradiated 800H micro-pillars, sample size effect is nonexistent both at room temperature and at 300 °C, shown in Figure 4.10. As *L* refers to dislocation spacing and the total dislocation density is held constant at testing temperatures, all three terms constituting to the critical resolved shear stress in Equation 1.9 are considered size-independent.

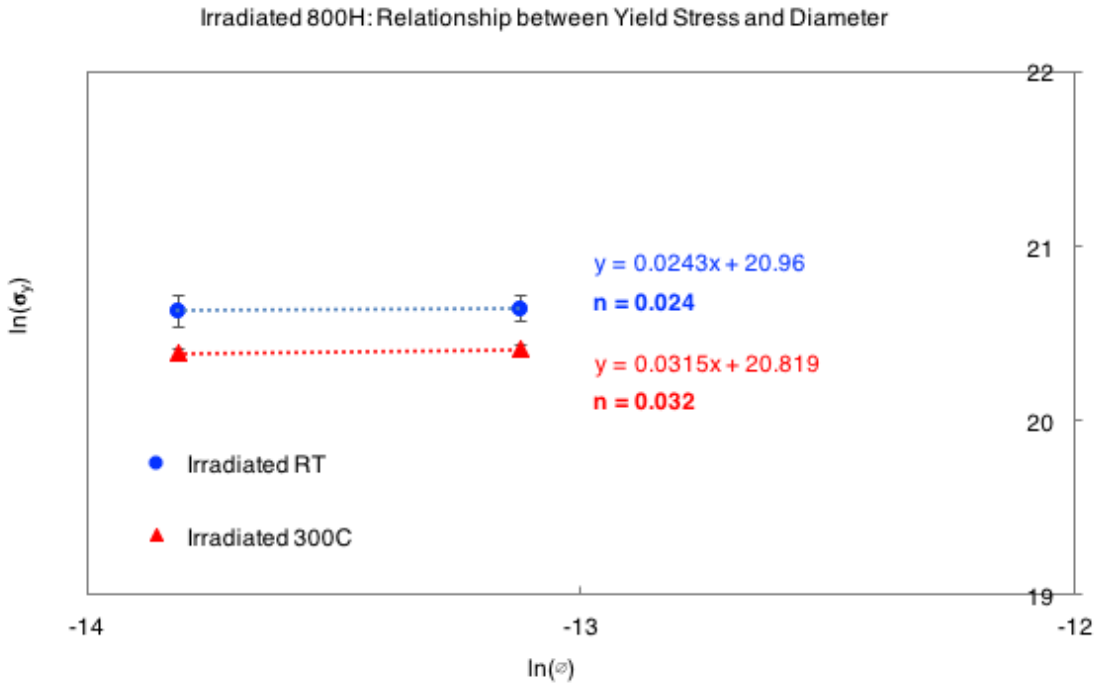

Figure 4.10 Influence of temperature on sample size effect in irradiated 800H micro-pillars (the smallest micro-pillar dimensions is 1x1x2 μm).

Chapter 5

TEM Characterization

5.1 Experimental and results

5.1.1 Flash polishing studies

Flash polishing studies were performed with an attempt to reduce FIB-induced damage from FIB-manufactured TEM foils. Table 5.1., constructed by Prof. Yabuuchi (Kyoto University), provides conditions for the flash polishing of metal alloys [169]. As FIB-manufactured TEM foils were lifted out from the cross-section T91 and 14YWT samples, the second column of Table 5.1 (RAFMs ODS SUS) provides the most appropriate polishing condition, so therefore was chosen for this study. The polishing solution consists of 5% or 8 ml. perchloric acid ($HClO_4$) and 95% or 92 ml. acetic acid (CH_3COOH). A rough diagram of the flash polishing system is provided in Figure 5.1 [169]. Major components of the flash polishing system include a power supply with the capability of providing 15 V., a timer that can be programmed at 10 ms, a solid state relay and the electrodes. The positive electrode is a pair of self-closed tweezers that holds the half Cu grid with a FIB-manufactured TEM sample with the thickness of approximately 150nm welded to it. The negative electrode is a standard Ni plate. This flash polishing system is to be performed in the temperature range of $0 – 5^0$C.

Table 5.1 Conditions of flash polishing

	pure Fe Fe binary alloy	RAFMs ODS SUS	W
Solution	5% HClO4 95 % methanol	5% HClO4 95 % acetic acid	1% NaOH
Voltage	12 V	15 V	18 V
Temperature	-30℃	0 - 5℃	0 - 5℃
Polishing time	10 ms	10 ms	10 ms
thickness before flash polishing	300 - 400 nm	150 nm	400 nm
distance between foil to electrode	1 cm	1 cm	1 cm

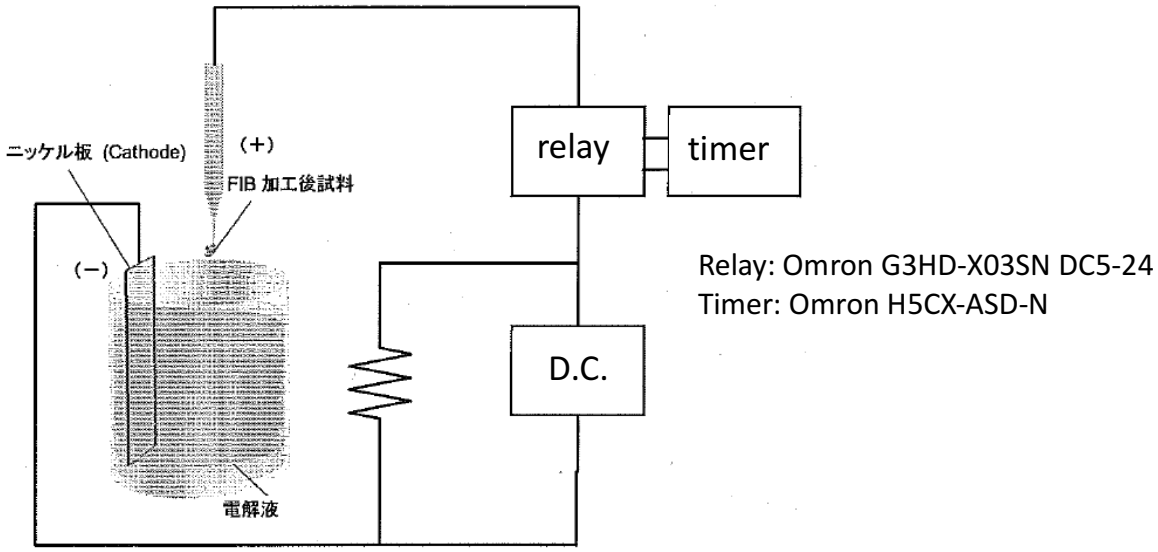

Figure 5.1 Rough diagram of the flash polishing circuit [169].

After studying the timer and relay circuit needed to achieve the desired voltage and polishing time, the flash polishing system in Figure 5.2 was set up at University of California, Berkeley. The system was tested many times to ensure consistent results and thus consistent polishing conditions. The power supply was set to 15 V, and the timer was programmed at 10 ms. as shown in Figure 5.3(a). After pushing the switch button, the oscilloscope always read 15 V for approximately 8 ms. This is illustrated in Figure 5.3(b). The rise and the drop time of the voltage are both approximately 1 ms., accounting for the 2 ms. loss from the programmed 10 ms. In order to compensate for the rise and the drop time, the timer could be programmed at 12 ms. instead of 10 ms. By doing so, the oscilloscope read 15 V for 9 ms. However, the timer was programmed at 10 ms. in order to avoid overpolishing and potentially losing the samples.

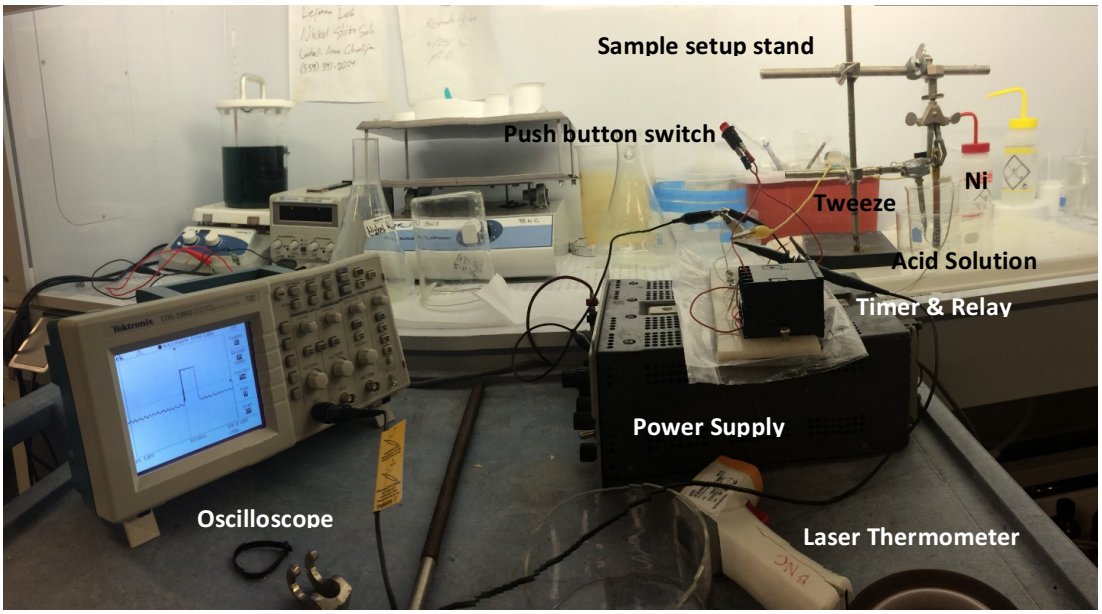

Figure 5.2 Flash polishing setup at University of California, Berkeley

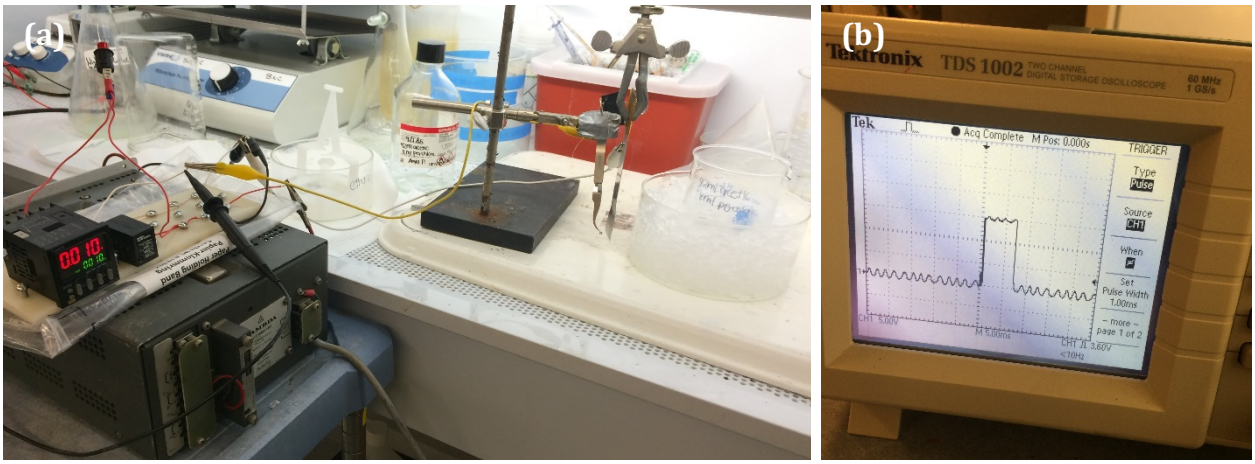

Figure 5.3 (a) Flash polishing setup for the experiment. The timer on the left is programmed to 10 ms. (b) The resulting voltage step curve illustrated by the oscilloscope.

Once the flash polishing system setup was accomplished, the system was put to the test. Two flash polishing dummy samples (jet polished TEM disks made out of Al-4%Cu alloy) were flash polished, one at 7.1^0C and the other at 4.4^0C. Prior to flash polishing, the polishing solution in the beaker was cooled down in the refrigerator (Figure 5.4(a)), and the IR thermometer was used to measure the temperature of the polishing solution right before the flash polishing was performed (Figure 5.4(b) and 5.4(c)). After flash polishing, the two dummy samples were observed under the TEM. It was proven that the flash polishing system worked as the dummy samples both got polished and lost the electron transparent area.

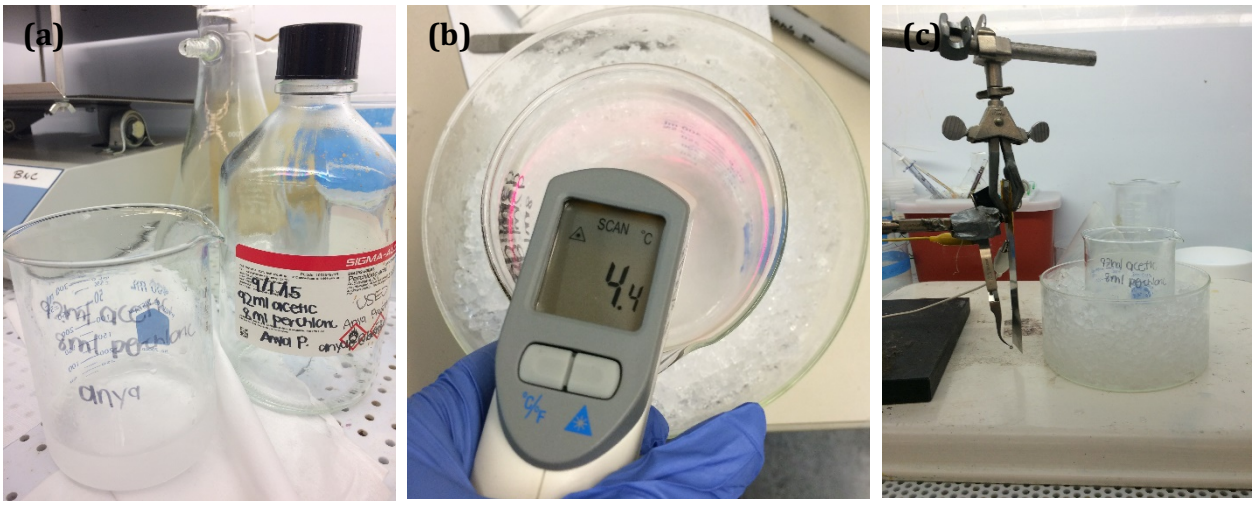

Figure 5.4 (a) Flash polishing solution in the beaker, ready to be cooled down in the refrigerator to the polishing temperature range (b) Laser thermometer reads the temperature of the polishing solution right before flash polishing is performed (c) The closer view of the flash polishing setup right before the polishing is carried out. The self-closed tweezers on the left holds the half Cu grid with the FIB-manufactured sample welded to one of the posts.

The FIB-manufactured T91 and 14YWT foils were flash polished at 2.6^0C and 2.4^0C, respectively. Unfortunately, as illustrated in Figure 5.5(a) and 5.5(b), the T91 foil disappeared after polishing. The most possible reason why the foil disappeared is that the thinnest area close to the Pt weld was polished away due to inappropriate foil thickness, voltage, polishing solution, polishing temperature or polishing time. The 14YWT foil, however, remained on the post after flash polishing. TEM images comparing the non-irradiated area and the irradiated area before and after flash polishing are shown in Figure 5.6 and Figure 5.7, respectively. The sample appeared only a little cleaner after flash polishing. The second round of flash polishing was performed on the 14YWT foil. Since the foil was already very thin, the same polishing conditions were carried on with the shorter polishing time, which was 5 ms. instead of 10 ms. When observed under the TEM, the defect density in the 14YWT foil was not differentiable from prior to the second time polishing. This could be due to the shorter polishing time. Unfortunately, after mechanical handling of the foil during a couple TEM sessions, the 14YWT broke off the post and the sample was lost.

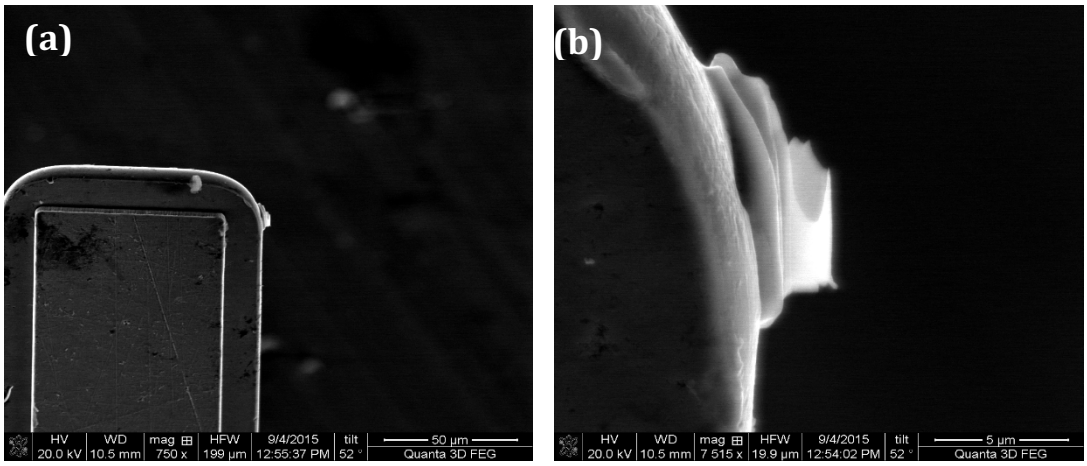

Figure 5.5 SEM images taken after flash polishing the FIB-manufactured T91 TEM foil (a) the post where the foil was welded to (b) the remaining portion of the T91 foil.

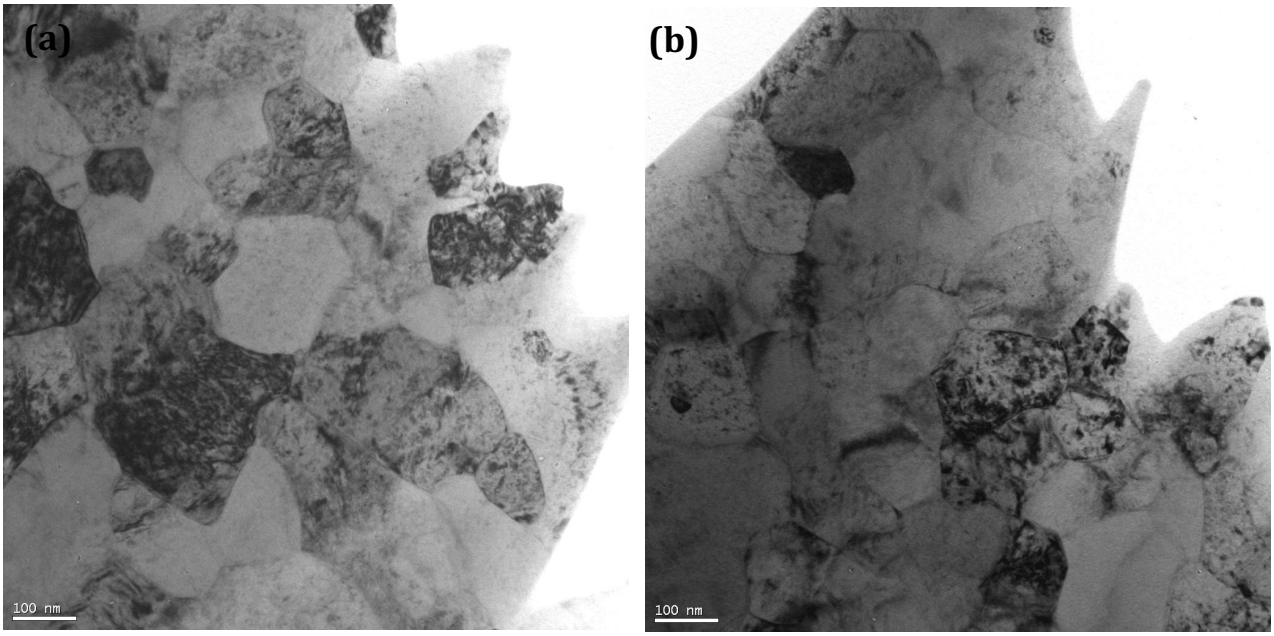

Figure 5.6 TEM images of the non-irradiated area in the FIB-manufactured 14YWT foil (a) before flash polishing (b) after flash polishing.

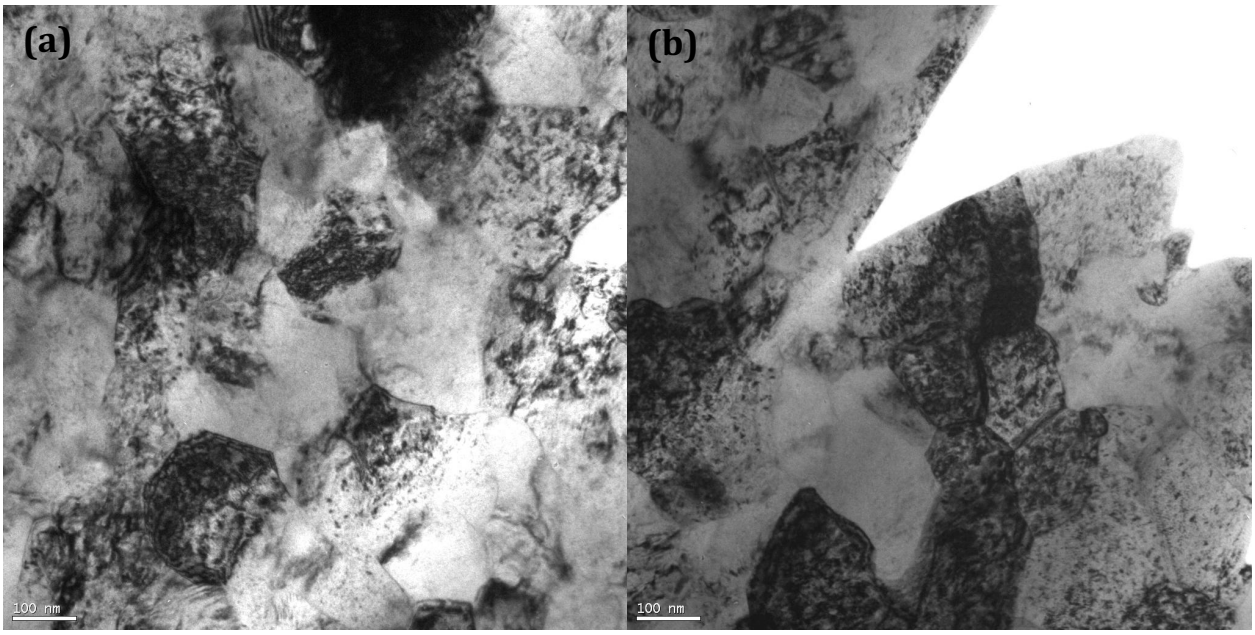

Figure 5.7 TEM images of the irradiated area in the FIB-manufactured 14YWT foil (a) before flash polishing (b) after flash polishing.

The next step to improve the flash polishing technique is to perform flash polishing on dummy samples that are comparable to the FIB-manufactured TEM foils such as jet-polished stainless steel TEM disks. Schematic of a jet-polished stainless steel flash polishing dummy sample is provided in Figure 5.8. Flash polishing dummy samples will be initially observed under the TEM. Subsequently, FIB damage will be induced on the samples. TEM images at the zone axes of particular grains of interest will be taken for comparison reasons. The dummy samples will then flash polished, and the TEM images will be taken with the exact same imaging condition after polishing. Accordingly, it would be possible to compare the FIB-induced defect density prior to and after flash polishing.

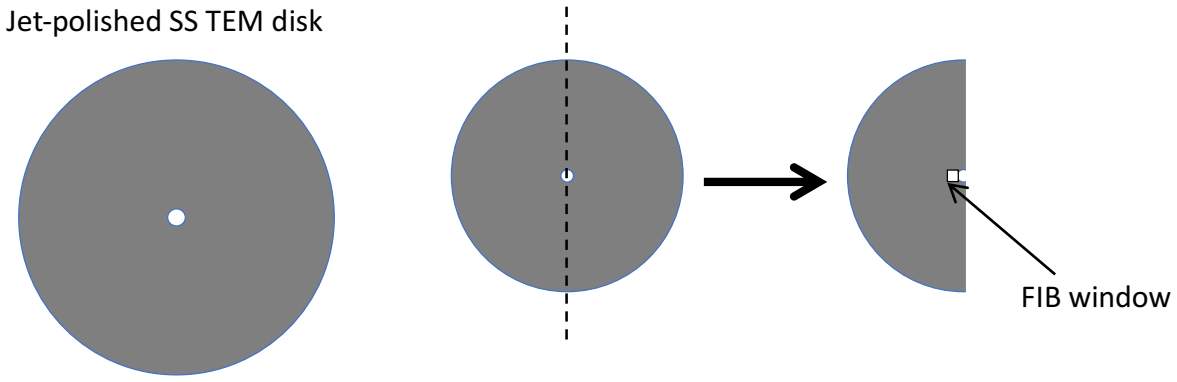

Figure 5.8 Schematic of the jet-polished stainless steel flash polishing dummy sample.

5.1.2 TEM foil fabrication

A FIB-fabricated TEM foil was prepared from the region perpendicular to the irradiated surface where the ion beam hits the sample, consisting of both the unirradiated and the irradiated matrix for direct comparisons. The FEI Strata 235 dual beam Focused Ion Beam FIB was used throughout all preparation steps. The final voltage used for thinning and cleaning procedures was 6 kV. TEM foils of the cross section of the compressed micro-pillars were fabricated using FEI Quanta3D FEG/FIB ESEM. After compression at room temperature, the top and the sides of the unirradiated and irradiated micro-pillars with 2x2x4 μm dimensions were covered with platinum layer for protection against FIB damage introduced during TEM foil fabrication. The micro-pillars were then thinned down to the width of 1 μm. Due to the limitations of the microscope, the final voltage used for thinning was 15 kV. All transmission electron microscopy analysis was performed using a JEOL 3010 microscope with 300 kV operating voltage. For comparison purposes, same two-beam conditions were intentionally chosen for both the unirradiated and the irradiated areas of the TEM foil. Similarly, TEM images were obtained from the same two-beam conditions in the case of post-compression micro-pillars.

5.1.3 TEM lift-outs of post compression micro-pillar cross sections

A schematic of the lifted-out pillar cross section is shown in Figure 5.9. TEM characterization was carried out in order to complement the studies of the influence of irradiation on mechanical property evolution obtained from *in situ* microcompresstion. TEM foil containing the unirradiated and the irradiated regions of the 800H alloy is shown in Figure 5.10. A contrast between the two regions is due to different levels of defect density resulted from ion-beam irradiation, with an assumption that the FIB damage of both regions is comparable. Figure 5.11 compares the unirradiated and the irradiated areas at higher magnifications. Although FIB-manufactured TEM foils inevitably experience defects during the fabrication processes, a clear transition from the lower to the higher defect density in the lamella (Figure 5.10) suggests the validity of characterization studies of irradiated samples prepared using FIB. Shown in Figure 5.12 (a) is a bright field image of a room temperature compressed 2x2x4 μm unirradiated micro-pillar. The bright field image of the irradiated counterpart taken from the same two-beam condition is shown in Figure 5.13. Despite FIB damage layers, wavy slips are commonly observed throughout the unirradiated micro-pillar. Figure 5.12 (b) provides a zoomed in image of wavy slip events in Figure 5.12 (a). Dislocations are of an order of hundreds of nanometers in length. Wavy slips are not observed in the irradiated micro-pillar foil.

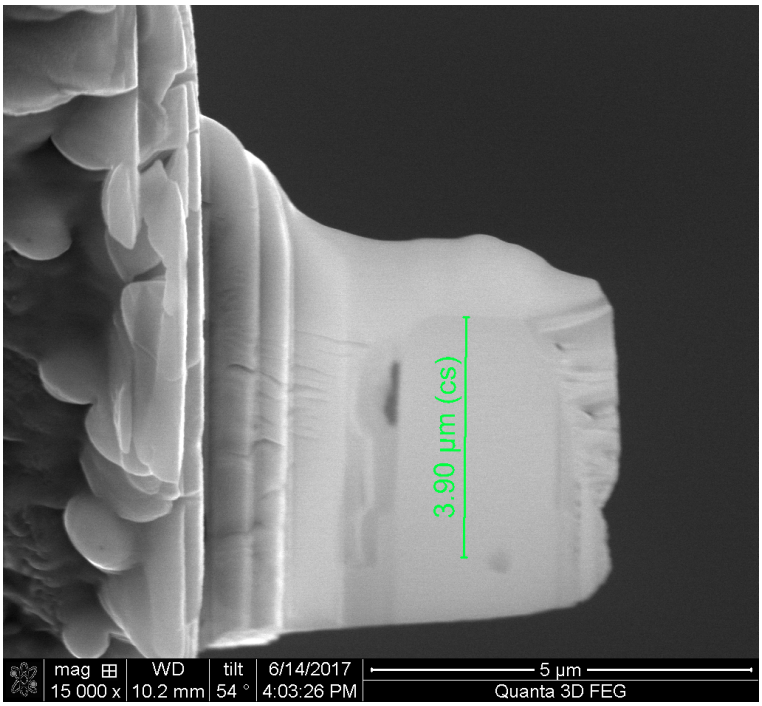

Figure 5.9 A schematic of the lifted-out pillar cross section.

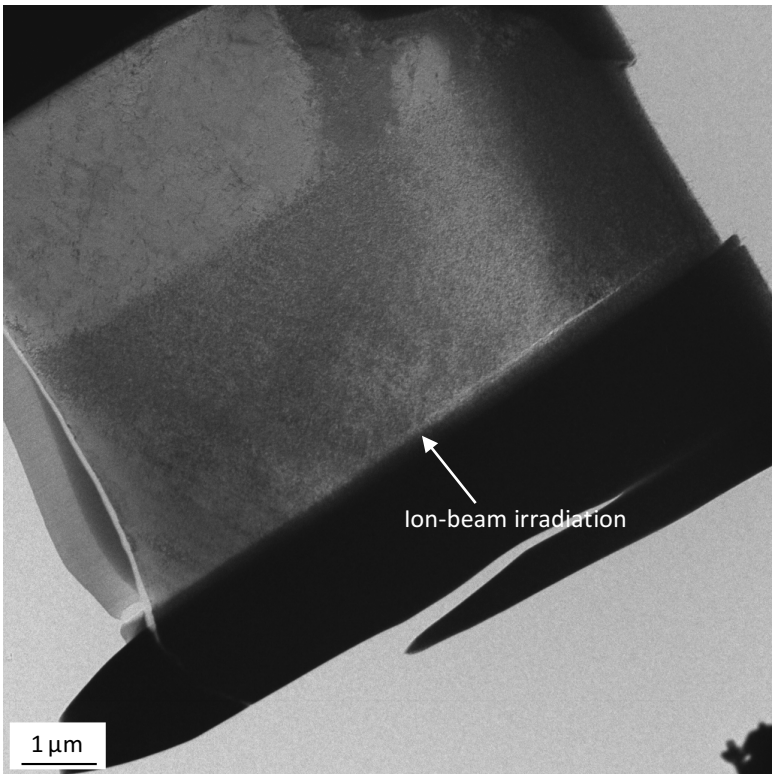

Figure 5.10 TEM foil of the 800H alloy consisting of unirradiated and ion-irradiated matrix from the [011] zone axis.

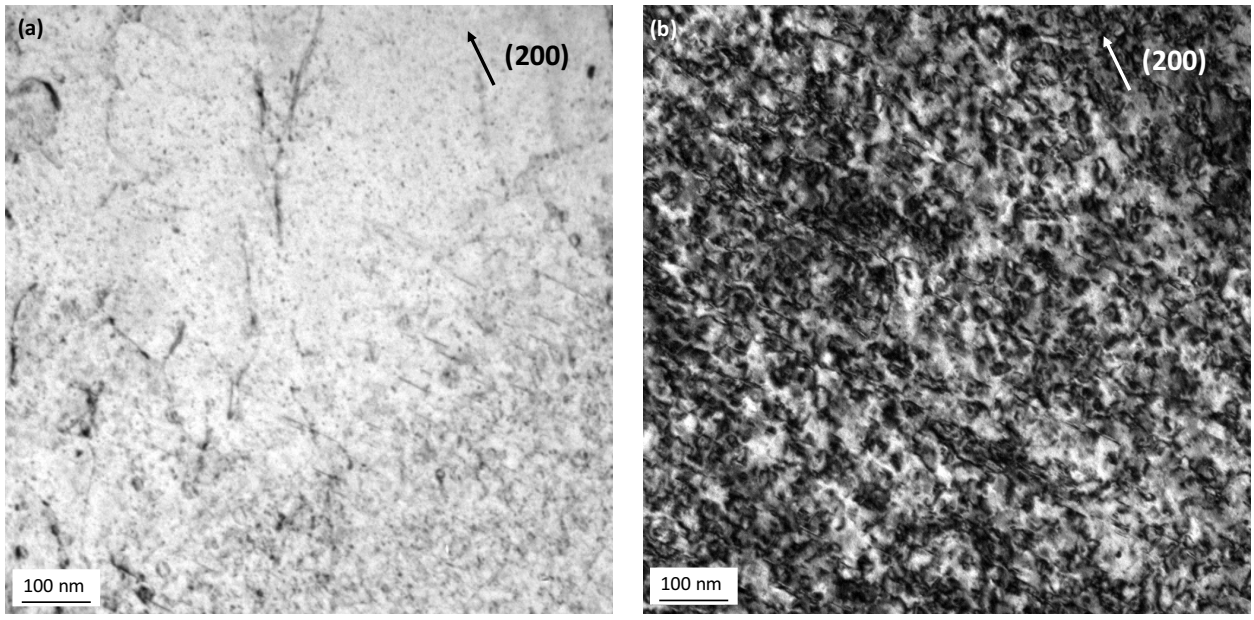

Figure 5.11 Bright field image (g = 200) of the 800H alloy (a) unirradiated area (b) irradiated area.

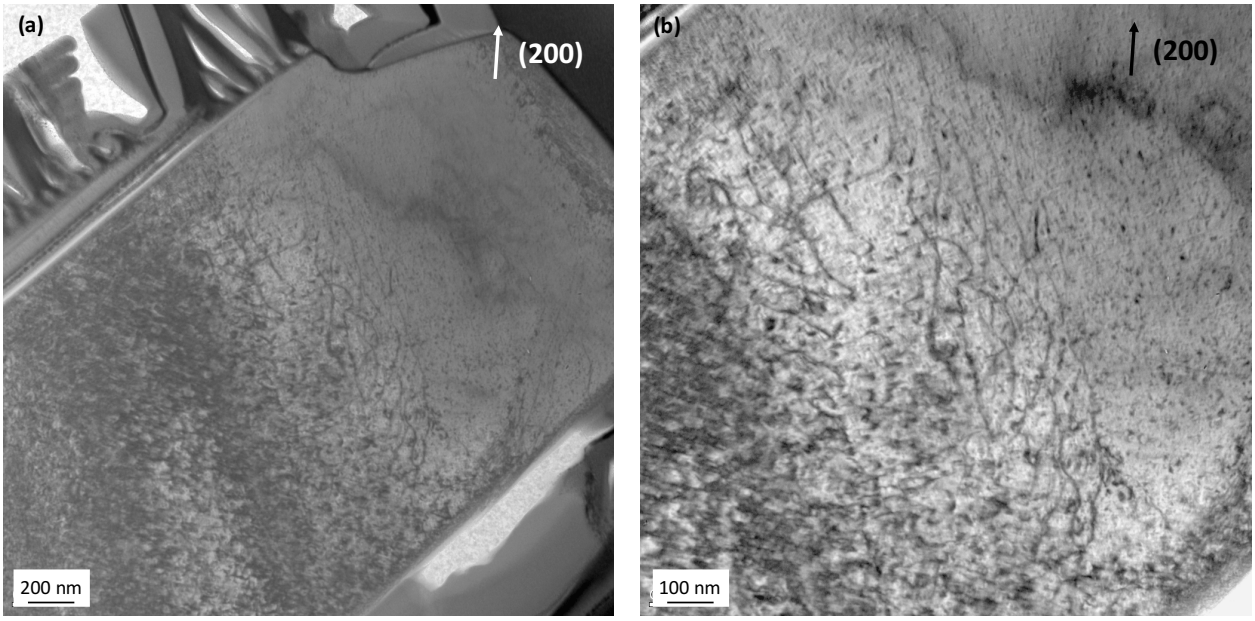

Figure 5.12 Bright field image (g = 200) of the room temperature compressed 2x2x4 μm unirradiated micro-pillar showing wavy slips.

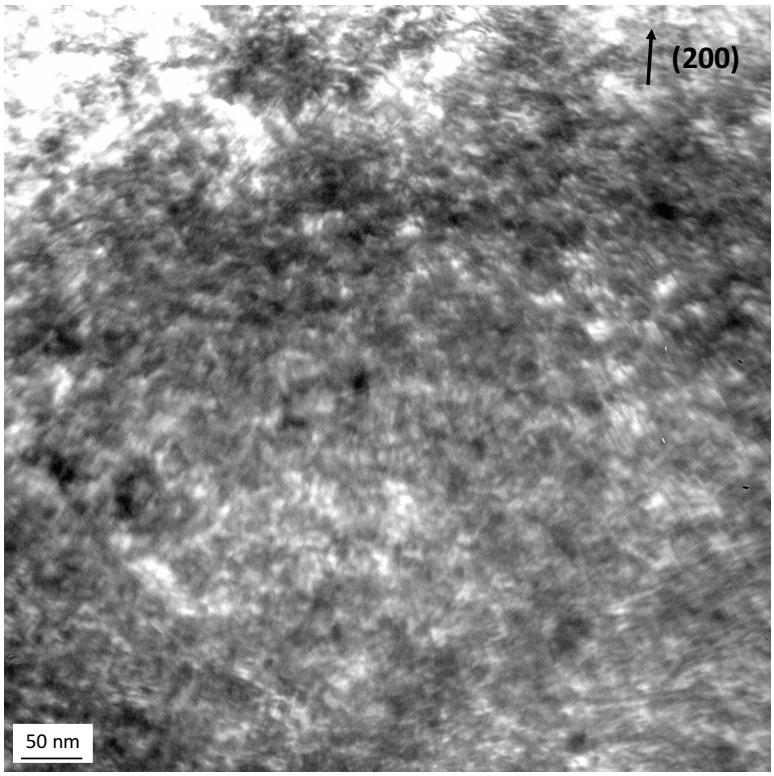

Figure 5.13 Bright field image (g = 200) of the room temperature compressed 2x2x4 μm irradiated micro-pillar.

5.2 Influence of irradiation on microstructure

The observation of wavy slips only in the unirradiated micro-pillar and not the irradiated counterpart could be explained by the fact that the irradiated matrix contains a significantly higher dislocation density after irradiation as shown earlier in Figure 5.10. Another possible explanation is that after irradiation, dislocations are pinned by irradiation-induced defects. Dislocation motion is localized in the defect-free channels i.e. the dislocations tends to move through the channels due to a lower energy barrier. The lack of cross slip events is also an evidence of dislocation localization. This indicated that most dislocations are concentrated on certain slip planes instead of having cross slip on multiple possible slip planes. This localization could contribute to altered mechanical properties.

Chapter 6

Conclusions

This dissertation presented the micromechanical testing techniques utilized for mechanical property measurements in nuclear structural materials. Surface and cross-sectional nanoindentation measurements and *in situ* micro-pillar compression testing were used to investigate the mechanical properties of ion irradiated materials (800H, T91, NCT91 and 14YWT), which are potential structural candidates for Gen-IV reactors. The two different mechanical testing methods demonstrated comparable yield stress measurements and showed that the nano-grained NCT91 and 14YWT alloys are significantly more resistant to irradiation hardening than T91 and 800H. The results are supported by bulk XRD measurements, which showed a significantly larger increase in dislocation density after irradiation in the coarse-grained T91 alloy than in nanocrystalline NCT91 and 14YWT. The methods demonstrated here will be vital in understanding the use of ion irradiation to simulate neutron irradiation and therefore reduce the handling difficulty and complications associated with neutron irradiation, which is essential for the high damage levels expected in Gen-IV reactors.

Nevertheless, size effects observed in small-scale mechanical testing, including nanoindentation and microcompression, have been a major obstacle to obtaining mechanical properties from small amount of irradiated volume. These size effects have been studied extensively at room temperature. However, the influence of temperature on size effects is currently not clear. Of particular interest is the development of high temperature small-scale mechanical testing techniques, which would better relate the mechanical property measurements to the actual operating temperatures of structural materials in nuclear reactors, and the fundamentals behind the independent influence of irradiation and temperature on indentation size effect and sample size effect in 800H. TEM characterization of the post-compression micro-pillars were also performed in order to complement the mechanical behavior evolution due to ion irradiation.

Novel findings can be summarized as follows:

1. *Indentation Size Effect (ISE)*:

For both unirradiated and the irradiated 800H, while hardness decreases with depth and temperature, reduced modulus remains relatively constant with depth and decreases with temperature. Orientation has a strong influence on indentation size effect. For the same grain orientation, ISE is less pronounced after irradiation. ISE is less pronounced at high temperatures due to the larger plastic zone size or the storage volume of GNDs.

2. *Sample Size Effect (SSE)*:

Sample size effects in the unirradiated and the irradiated 800H micro-pillars are investigated at room and at elevated temperatures. After irradiation, a few or a single slip events as opposed to

multiple slip events were observed (*in situ* and under the TEM) in the irradiated 800H, suggesting localized plastic deformation through dislocation channeling mechanism via specific slip planes. Different deformation behaviors can be explained by different microstructures and defect densities observed under the TEM i.e. wavy slips in the unirradiated micro-pillars. Sample size effect is less pronounced in the irradiated 800H owing to irradiation-induced dislocations possibly having spacing smaller than sample dimensions. For unirradiated 800H, increasing temperature results in the decrease in lattice stress and shear modulus, causing size-dependent term to have more significant contribution to the critical resolved shear stress needed to initiate plastic deformation. Sample size effect is therefore more significant.

In summary, the high temperature nanoindentation technique developed here coupled with careful consideration of grain orientation demonstrates a testing method that can provide higher confidence in the properties measured from small volumes. In other words, less significant ISE at high temperatures helps bridge the gap between macroscale mechanical testing and small-scale mechanical testing. For the first time, due to the more contribution of the size-dependent term, the reasonably more pronounced sample size effect at higher temperatures in FCC metals raises a possible conclusion that size effect may not be determine solely by crystal structure. While the high temperature nanoindentation method provides measurements that better relate to the actual operating temperatures in real-world applications such as in nuclear reactors, the high temperature *in situ* microcompression allows real-time observation of deformation mechanisms which can be complemented by TEM characterization.

References

[1] Mansur, L. K., et al. "Materials needs for fusion, Generation IV fission reactors and spallation neutron sources–similarities and differences." Journal of Nuclear Materials 329 (2004): 166-172.

[2] Murty, K. L., and I. Charit. "Structural materials for Gen-IV nuclear reactors: Challenges and opportunities." Journal of Nuclear Materials 383.1 (2008): 189-195.

[3] Allen, T. R., et al. "Materials challenges for generation IV nuclear energy systems." Nuclear Technology 162.3 (2008): 342-357.

[4] Yvon, P., and F. Carré. "Structural materials challenges for advanced reactor systems." Journal of Nuclear Materials 385.2 (2009): 217-222.

[5] Chant, I., and K. L. Murty. "Structural materials issues for the next generation fission reactors." JOM 62.9 (2010): 67-74.

[6] Zinkle, Steven J., and G. S. Was. "Materials challenges in nuclear energy." Acta Materialia 61.3 (2013): 735-758.

[7] Yvon, Pascal, et al. "Structural materials for next generation nuclear systems: Challenges and the path forward." Nuclear Engineering and Design 294 (2015): 161-169.

[8] Locatelli, Giorgio, Mauro Mancini, and Nicola Todeschini. "Generation IV nuclear reactors: Current status and future prospects." Energy Policy 61 (2013): 1503-1520.

[9] Fazio, Concetta, et al. "Innovative materials for Gen IV systems and transmutation facilities: The cross-cutting research project GETMAT." Nuclear Engineering and Design 241.9 (2011): 3514-3520.

[10] Tuček, K., et al. "Generation IV Reactor Safety and Materials Research by the Institute for Energy and Transport at the European Commission's Joint Research Centre." Nuclear Engineering and Design 265 (2013): 1181-1193.

[11] Yvon, Pascal, ed. Structural Materials for Generation IV Nuclear Reactors. Woodhead Publishing, 2016.

[12] Klueh, R. L., et al. "Ferritic/martensitic steels–overview of recent results." Journal of Nuclear Materials 307 (2002): 455-465.

[13] Schaeublin, R., D. Gelles, and M. Victoria. "Microstructure of irradiated ferritic/martensitic steels in relation to mechanical properties." Journal of Nuclear Materials 307 (2002): 197-202.

[14] Klueh, R. L., and A. T. Nelson. "Ferritic/martensitic steels for next-generation reactors." Journal of Nuclear Materials 371.1 (2007): 37-52.

[15] Plesiutschnig, Ernst, et al. "Ferritic phase transformation to improve creep properties of martensitic high Cr steels." Scripta Materialia 122 (2016): 98-101.

[16] Henry, J., and S. A. Maloy. "Irradiation-resistant ferritic and martensitic steels as core materials for Generation IV nuclear reactors." Structural Materials for Generation IV Nuclear Reactors (2016): 329.

[17] Gupta, G., et al. "Microstructural evolution of proton irradiated T91." Journal of nuclear materials 351.1 (2006): 162-173.

[18] Clausing, R. E., et al. "Radiation-induced segregation in HT-9 martensitic steel." Journal of Nuclear Materials 141 (1986): 978-981.

[19] Jiao, Z., and G. S. Was. "Segregation behavior in proton-and heavy-ion-irradiated ferritic–martensitic alloys." Acta Materialia 59.11 (2011): 4467-4481.

[20] Wharry, Janelle P., et al. "Radiation-induced segregation and phase stability in ferritic–martensitic alloy T 91." Journal of Nuclear Materials 417.1 (2011): 140-144.

[21] Wharry, Janelle P., and Gary S. Was. "A systematic study of radiation-induced segregation in ferritic–martensitic alloys." Journal of Nuclear Materials 442.1 (2013): 7-16.

[22] Field, Kevin G., et al. "Dependence on grain boundary structure of radiation induced segregation in a 9wt.% Cr model ferritic/martensitic steel." Journal of Nuclear Materials 435.1 (2013): 172-180.

[23] Lauritzen, T., A. Withop, and U. E. Wolff. "Swelling of austenitic stainless steels under fast neutron irradiation at elevated temperatures." Nuclear Engineering and Design 9.2 (1969): 265-268.

[24] Kenik, E. A. "Radiation-induced segregation in irradiated Type 304 stainless steels." Journal of nuclear materials 187.3 (1992): 239-246.

[25] Kenik, E. A., T. Inazumi, and G. E. C. Bell. "Radiation-induced grain boundary segregation and sensitization of a neutron-irradiated austenitic stainless steel." Journal of nuclear materials 183.3 (1991): 145-153.

[26] Yamamoto, Yukinori, et al. "Creep-resistant, Al2O3-forming austenitic stainless steels." Science 316.5823 (2007): 433-436.

[27] Yamamoto, Yukinori, et al. "Alloying effects on creep and oxidation resistance of austenitic stainless steel alloys employing intermetallic precipitates." Intermetallics 16.3 (2008): 453-462.

[28] Ukai, Shigeharu, and Masayuki Fujiwara. "Perspective of ODS alloys application in nuclear environments." Journal of Nuclear Materials 307 (2002): 749-757.

[29] Alamo, A., et al. "Assessment of ODS-14% Cr ferritic alloy for high temperature applications." Journal of Nuclear Materials 329 (2004): 333-337.

[30] Odette, G. R., M. J. Alinger, and B. D. Wirth. "Recent developments in irradiation-resistant steels." Annu. Rev. Mater. Res. 38 (2008): 471-503.

[31] Schneibel, Joachim H., et al. "Ultrafine-grained nanocluster-strengthened alloys with unusually high creep strength." Scripta Materialia 61.8 (2009): 793-796.

[32] Lin, Jun-Li, et al. "In situ synchrotron tensile investigations on 14YWT, MA957, and 9-Cr ODS alloys." Journal of Nuclear Materials 471 (2016): 289-298.

[33] Kim, Ick-Soo, et al. "Effect of Ti and W on the mechanical properties and microstructure of 12% Cr base mechanical-alloyed nano-sized ODS ferritic alloys." ISIJ international 43.10 (2003): 1640-1646.

[34] Allen, T., et al. "Advanced structural materials and cladding." MRS bulletin 34.01 (2009): 20-27.

[35] De Castro, V., et al. "Analytical characterisation of oxide dispersion strengthened steels for fusion reactors." Materials Science and Technology 27.4 (2011): 719-723.

[36] De Castro, V., et al. "In-situ Fe+ ion irradiation of an oxide dispersion strengthened steel." Journal of Physics: Conference Series. Vol. 522. No. 1. IOP Publishing, 2014.

[37] De Castro, Vanessa, et al. "TEM characterization of simultaneous triple ion implanted ODS Fe12Cr." Journal of Nuclear Materials 455.1 (2014): 157-161.

[38] Gan, Jian, et al. "Irradiated microstructure of alloy 800H." Journal of nuclear materials 351.1 (2006): 223-227.

[39] Rouxel, Baptiste, et al. "Influence of the austenitic stainless steel microstructure on the void swelling under ion irradiation." EPJ Nuclear Sciences & Technologies 2 (2016): 30.

[40] Zhou, Rongsheng, et al. "Irradiation-assisted stress corrosion cracking of austenitic alloys in supercritical water." Journal of Nuclear Materials 395.1 (2009): 11-22.

[41] Was, G. S., et al. "Corrosion and stress corrosion cracking in supercritical water." Journal of Nuclear Materials 371.1 (2007): 176-201.

[42] Rose, M., A. G. Balogh, and H. Hahn. "Instability of irradiation induced defects in nanostructured materials." Nuclear Instruments and Methods in Physics Research Section B: Beam Interactions with Materials and Atoms 127 (1997): 119-122.

[43] Song, M., et al. "Response of equal channel angular extrusion processed ultrafine-grained T91 steel subjected to high temperature heavy ion irradiation." Acta Materialia 74 (2014): 285-295.

[44] Nanstad, Randy K., et al. "High temperature irradiation effects in selected Generation IV structural alloys." Journal of Nuclear Materials 392.2 (2009): 331-340.

[45] de Castro, Vanessa, et al. "Effects of single-and simultaneous triple-ion-beam irradiation on an oxide dispersion-strengthened Fe12Cr steel." Journal of Materials Science 50.5 (2015): 2306-2317.

[46] Nelson, R. S., D. J. Mazey, and J. A. Hudson. "The use of ion accelerators to simulate fast neutron-induced voidage in metals." Journal of Nuclear Materials 37.1 (1970): 1-12.

[47] Kulcinski, G. L., A. B. Wittkower, and G. Ryding. "Use of heavy ions from a tandem accelerator to simulate high fluence, fast neutron damage in metals." Nuclear Instruments and Methods 94.2 (1971): 365-375.

[48] Packan, N. H., K. Farrell, and J. O. Stiegler. "Correlation of neutron and heavy-ion damage: I. The influence of dose rate and injected helium on swelling in pure nickel." Journal of Nuclear Materials 78.1 (1978): 143-155.

[49] Lewis, M. B., et al. "Improved techniques for heavy-ion simulation of neutron radiation damage." Nuclear Instruments and Methods 167.2 (1979): 233-247.

[50] Abromeit, C. "Aspects of simulation of neutron damage by ion irradiation." Journal of nuclear materials 216 (1994): 78-96.

[51] Was, G. S., et al. "Emulation of neutron irradiation effects with protons: validation of principle." Journal of nuclear materials 300.2 (2002): 198-216.

[52] Kirk, Marquis A., et al. "In situ transmission electron microscopy and ion irradiation of ferritic materials." Microsc. Res. Tech 72.3 (2009): 182-188.

[53] Etienne, A., et al. "Dislocation loop evolution under ion irradiation in austenitic stainless steels." Journal of Nuclear Materials 400.1 (2010): 56-63.

[54] Was, G. S., et al. "Emulation of reactor irradiation damage using ion beams." Scripta Materialia 88 (2014): 33-36.

[55]Uchic, Michael D., and Dennis M. Dimiduk. "A methodology to investigate size scale effects in crystalline plasticity using uniaxial compression testing." Materials Science and Engineering: A 400 (2005): 268-278.

[56] Hosemann, P., et al. "Nanoindentation on ion irradiated steels." Journal of Nuclear Materials 389.2 (2009): 239-247.

[57] Hosemann, P., et al. "An exploratory study to determine applicability of nano-hardness and micro-compression measurements for yield stress estimation." Journal of Nuclear Materials 375.1 (2008): 135-143.

[58] Hosemann, Peter, et al. "Issues to consider using nano indentation on shallow ion beam irradiated materials." Journal of Nuclear Materials 425.1 (2012): 136-139.

[59] Kiener, Daniel, et al. " Kiener, Daniel, Andrew M. Minor, Osman Anderoglu, Yongqiang Wang, Stuart A. Maloy, and Peter Hosemann. "Application of small-scale testing for investigation of ion-beam-irradiated materials." *Journal of Materials Research*27, no. 21 (2012): 2724-2736.

[60] Armstrong, D. E. J., et al. "Small-scale characterisation of irradiated nuclear materials: Part II nanoindentation and micro-cantilever testing of ion irradiated nuclear materials." Journal of Nuclear Materials 462 (2015): 374-381.

[61] Lupinacci, A., et al. "Characterization of ion beam irradiated 304 stainless steel utilizing nanoindentation and Laue microdiffraction." Journal of Nuclear Materials 458 (2015): 70-76.

[62] Oliver, Warren Carl, and George Mathews Pharr. "An improved technique for determining hardness and elastic modulus using load and displacement sensing indentation experiments." Journal of materials research 7.06 (1992): 1564-1583.

[63] Uchic, Michael D., Dennis M. Dimiduk, Jeffrey N. Florando, and William D. Nix. "Sample dimensions influence strength and crystal plasticity." *Science* 305, no. 5686 (2004): 986-989.

[64] *Keysight Technologies Continuous Stiffness Measurement (CSM) Option* literature.cdn.keysight.com/litweb/pdf/5990-4183EN.pdf.

[65] *Quasistatic Nanoindentation: An Overview*. www.hysitron.com/resources-support/education-training/nanoindentation.

[66] Oliver, Warren C., and Georges M. Pharr. "Measurement of hardness and elastic modulus by instrumented indentation: Advances in understanding and refinements to methodology." Journal of materials research 19.01 (2004): 3-20.

[67] K.L. Johnson: The correlation of indentation experiments. J. Mech. Phys. Solids 18, 115 (1970).

[68] D. Kiener, R. Pippan, C. Motz, and H.G.M. Kreuzer: Microstruc- tural evolution of the deformed volume beneath microindents in tungsten and copper. Acta Mater. 54, 2801 (2006).

[69] M. Rester, C. Motz, and R. Pippan: Microstructural investigation of the volume beneath nanoindentations in copper. Acta Mater. 55, 6427 (2007).

[70] Dimiduk, D. M., M. D. Uchic, and T. A. Parthasarathy. "Size-affected single-slip behavior of pure nickel microcrystals." *Acta Materialia* 53, no. 15 (2005): 4065-4077.

[71] Uchic, Michael D., Paul A. Shade, and Dennis M. Dimiduk. "Plasticity of micrometer-scale single crystals in compression." *Annual Review of Materials Research* 39 (2009): 361-386.

[72] Uchic MD, Dimiduk DM, Florando JN, Nix WD. 2003. Exploring specimen size effects in plastic defor- mation of Ni3(Al, Ta). *Mater. Res. Soc. Symp. Proc.* 753:BB1.4.1–6

[73] Greer, Julia R., Warren C. Oliver, and William D. Nix. "Size dependence of mechanical properties of gold at the micron scale in the absence of strain gradients." Acta Materialia 53, no. 6 (2005): 1821-1830.

[74] Greer JR, Nix WD. 2006. Nanoscale gold pillars strengthened through dislocation starvation. *Phys. Rev. B* 73:245410

[75] Zhang, Haitao, Brian E. Schuster, Qiuming Wei, and Kaliat T. Ramesh. "The design of accurate micro-compression experiments." Scripta Materialia 54, no. 2 (2006): 181-186.

[76] Pethica, J. B., R. Hutchings, and Wi C. Oliver. "Hardness measurement at penetration depths as small as 20 nm." *Philosophical Magazine A* 48.4 (1983): 593-606.

[77] Pharr, G. M., and W. C. Oliver. "Nanoindentation of silver-relations between hardness and dislocation structure." *Journal of Materials Research* 4.1 (1989): 94-101.

[78] Nix, William D. "Mechanical properties of thin films." *Metallurgical and Materials Transactions A* 20, no. 11 (1989): 2217-2245.

[79] De Guzman, Melissa Shell, Gabi Neubauer, Paul Flinn, and William D. Nix. "The role of indentation depth on the measured hardness of materials." *MRS Online Proceedings Library Archive* 308 (1993).

[80] De Guzman, Melissa Shell, Gabi Neubauer, Paul Flinn, and William D. Nix. "The role of indentation depth on the measured hardness of materials." MRS Online Proceedings Library Archive 308 (1993).

[81] Ma, Qing, and David R. Clarke. "Size dependent hardness of silver single crystals." Journal of Materials Research 10, no. 4 (1995): 853-863.

[82] Ma, Qing, and David R. Clarke. "Size dependent hardness of silver single crystals." *Journal of Materials Research* 10, no. 4 (1995): 853-863.

[83] Rittner, M. N., J. R. Weertman, J. A. Eastman, K. B. Yoder, and D. S. Stoned. "Mechanical behavior of nanocrystalline aluminum-zirconium." *Materials Science and Engineering: A* 237, no. 2 (1997): 185-190.

[84] Elmustafa, A. A., and D. S. Stone. "Indentation size effect in polycrystalline FCC metals." *Acta Materialia* 50, no. 14 (2002): 3641-3650.

[85] Voyiadjis, George Z., and Rick Peters. "Size effects in nanoindentation: an experimental and analytical study." *Acta Mechanica* 211.1 (2010): 131-153.

[86] Huang, Y., et al. "A model of size effects in nano-indentation." *Journal of the Mechanics and Physics of Solids* 54.8 (2006): 1668-1686.

[87] Nix, William D., and Huajian Gao. "Indentation size effects in crystalline materials: a law for strain gradient plasticity." *Journal of the Mechanics and Physics of Solids* 46, no. 3 (1998): 411-425.

[88] Gao, H., Y. Huang, W. D. Nix, and J. W. Hutchinson. "Mechanism-based strain gradient plasticity—I. Theory." *Journal of the Mechanics and Physics of Solids* 47, no. 6 (1999): 1239-1263.

[89] Huang, Y., H. Gao, W. D. Nix, and J. W. Hutchinson. "Mechanism-based strain gradient plasticity—II. Analysis." *Journal of the Mechanics and Physics of Solids* 48, no. 1 (2000): 99-128.

[90] Pharr, George M., Erik G. Herbert, and Yanfei Gao. "The indentation size effect: a critical examination of experimental observations and mechanistic interpretations." *Annual Review of Materials Research* 40 (2010): 271-292.

[91] Ashby, M. F. "The deformation of plastically non-homogeneous materials." *Philosophical Magazine* 21, no. 170 (1970): 399-424.

[92] Durst, Karsten, Björn Backes, and Mathias Göken. "Indentation size effect in metallic materials: correcting for the size of the plastic zone." *Scripta Materialia* 52, no. 11 (2005): 1093-1097.

[93] Durst, Karsten, Björn Backes, Oliver Franke, and Mathias Göken. "Indentation size effect in metallic materials: Modeling strength from pop-in to macroscopic hardness using geometrically necessary dislocations." *Acta Materialia* 54, no. 9 (2006): 2547-2555.

[94] Franke, Oliver, Jonathan C. Trenkle, and Christopher A. Schuh. "Temperature dependence of the indentation size effect." *Journal of Materials Research*25.7 (2010): 1225-1229.

[95] Hosemann, P., C. Shin, and D. Kiener. "Small scale mechanical testing of irradiated materials." *Journal of Materials Research* 30, no. 9 (2015): 1231-1245.

[96] Bei, Hongbin, Sanghoon Shim, Easo P. George, Michael K. Miller, E. G. Herbert, and George Mathews Pharr. "Compressive strengths of molybdenum alloy micro-pillars prepared using a new technique." *Scripta Materialia* 57, no. 5 (2007): 397-400.

[97] Bei, Hongbin, Sanghoon Shim, George Mathews Pharr, and Easo P. George. "Effects of pre-strain on the compressive stress–strain response of Mo-alloy single-crystal micropillars." Acta Materialia 56, no. 17 (2008): 4762-4770.

[98] Greer, Julia R., Christopher R. Weinberger, and Wei Cai. "Comparing the strength of fcc and bcc sub-micrometer pillars: Compression experiments and dislocation dynamics simulations." Materials Science and Engineering: A 493, no. 1 (2008): 21-25.

[99] Zaiser, Michael, Jan Schwerdtfeger, A. S. Schneider, C. P. Frick, Blythe Gore Clark, P. A. Gruber, and Eduard Arzt. "Strain bursts in plastically deforming molybdenum micro-and nanopillars." Philosophical Magazine 88, no. 30-32 (2008): 3861-3874.

[100] Schneider, A. S., B. G. Clark, C. P. Frick, P. A. Gruber, and E. Arzt. "Effect of orientation and loading rate on compression behavior of small-scale Mo pillars." *Materials Science and Engineering: A* 508, no. 1 (2009): 241-246.

[101] Kim, Ju-Young, and Julia R. Greer. "Tensile and compressive behavior of gold and molybdenum single crystals at the nano-scale." *Acta Materialia* 57, no. 17 (2009): 5245-5253.

[102] Schneider, A. S., D. Kaufmann, B. G. Clark, C. P. Frick, P. A. Gruber, R. Mönig, O. Kraft, and E. Arzt. "Correlation between critical temperature and strength of small-scale bcc pillars." *Physical review letters* 103, no. 10 (2009): 105501.

[103] Han, Seung Min, Tara Bozorg-Grayeli, James R. Groves, and William D. Nix. "Size effects on strength and plasticity of vanadium nanopillars." *Scripta Materialia* 63, no. 12 (2010): 1153-1156.

[104] Schneider, A. S., C. P. Frick, B. G. Clark, P. A. Gruber, and E. Arzt. "Influence of orientation on the size effect in bcc pillars with different critical temperatures." Materials Science and Engineering: A 528, no. 3 (2011): 1540-1547.

[105] Kaufmann, D., R. Mönig, C. A. Volkert, and O. Kraft. "Size dependent mechanical behaviour of tantalum." International Journal of Plasticity 27, no. 3 (2011): 470-478.

[106] Schneider, A. S., C. P. Frick, E. Arzt, W. J. Clegg, and S. Korte. "Influence of test temperature on the size effect in molybdenum small-scale compression pillars." *Philosophical Magazine Letters*93, no. 6 (2013): 331-338.

[107] Greer, Julia R., Warren C. Oliver, and William D. Nix. "Size dependence of mechanical properties of gold at the micron scale in the absence of strain gradients." *Acta Materialia* 53, no. 6 (2005): 1821-1830.

[108] Volkert, Cynthia Ann, and Erica T. Lilleodden. "Size effects in the deformation of sub-micron Au columns." *Philosophical Magazine*86, no. 33-35 (2006): 5567-5579.

[109] Kiener, Daniel, Christian Motz, Thomas Schöberl, Monika Jenko, and Gerhard Dehm. "Determination of mechanical properties of copper at the micron scale." *Advanced Engineering Materials* 8, no. 11 (2006): 1119-1125.

[110] Ng, K. S., and A. H. W. Ngan. "Stochastic nature of plasticity of aluminum micro-pillars." Acta Materialia 56, no. 8 (2008): 1712-1720.

[111] Brinckmann, Steffen, Ju-Young Kim, and Julia R. Greer. "Fundamental differences in mechanical behavior between two types of crystals at the nanoscale." *Physical review letters* 100, no. 15 (2008): 155502.

[112] Yang, Zhong, J. P. Li, J. X. Zhang, G. W. Lorimer, and J. A. M. S. E. L. Robson. "Review on research and development of magnesium alloys." *Acta Metallurgica Sinica (English Letters)* 21, no. 5 (2008): 313-328.

[113] Shan, Z. W., Raja K. Mishra, SA Syed Asif, Oden L. Warren, and Andrew M. Minor. "Mechanical annealing and source-limited deformation in submicrometre-diameter Ni crystals." *Nature materials* 7, no. 2 (2008): 115-119.

[114] Kiener, Daniel, Christian Motz, Gerhard Dehm, and Reinhard Pippan. "Overview on established and novel FIB based miniaturized mechanical testing using in-situ

[115] Parthasarathy, Triplicane A., Satish I. Rao, Dennis M. Dimiduk, Michael D. Uchic, and Dallas R. Trinkle. "Contribution to size effect of yield strength from the stochastics of dislocation source lengths in finite samples." *Scripta Materialia* 56, no. 4 (2007): 313-316.

[116] Sevillano, J. Gil, I. Ocaña Arizcorreta, and L. P. Kubin. "Intrinsic size effects in plasticity by dislocation glide." *Materials Science and Engineering: A* 309 (2001): 393-405.

[117] Pathak, Siddhartha, et al. "Importance of surface preparation on the nano-indentation stress- strain curves measured in metals." Journal of Materials Research 24.03 (2009): 1142-1155.

[118] Donnelly, Eve, et al. "Effects of surface roughness and maximum load on the mechanical properties of cancellous bone measured by nanoindentation." Journal of Biomedical Materials Research Part A 77.2 (2006): 426-435.

[119] PI 85L SEM PicoIndenter - Overview - Technology for Surface Analysis & Surface Measurement | Bruker." *Bruker.com*, www.bruker.com/products/surface-and-dimensional-analysis/nanomechanical-test-instruments/nanomechanical-test-instruments-for-microscopes/pi-85l-sem-picoindenter/overview.html.

[120] Ungar, T. S., et al. "Dislocations, grain size and planar faults in nanostructured copper determined by high resolution X-ray diffraction and a new procedure of peak profile analysis." Acta materialia 46.10 (1998): 3693-3699.

[121] Was, G. S., et al. "Resolution of the carbon contamination problem in ion irradiation experiments." Nuclear Instruments and Methods in Physics Research Section B: Beam Interactions with Materials and Atoms 412 (2017): 58-65.

[122] Ribárik, Gábor, and Tamás Ungár. "Characterization of the microstructure in random and textured polycrystals and single crystals by diffraction line profile analysis." Materials Science and Engineering: A 528.1 (2010): 112-121.

[123] Ungár, T., and A. Borbély. "The effect of dislocation contrast on x-ray line broadening: A new approach to line profile analysis." Applied Physics Letters 69.21 (1996): 3173-3175.

[124] Ungár, T., and Gy Tichy. "The Effect of Dislocation Contrast on X-Ray Line Profiles in Untextured Polycrystals." physica status solidi (a) 171.2 (1999): 425-434.

[125] Ungár, Tamás, et al. "Crystallite size distribution and dislocation structure determined by diffraction profile analysis: principles and practical application to cubic and hexagonal crystals." Journal of Applied Crystallography 34.3 (2001): 298-310.

[126] Seymour, T., et al. "Evolution of dislocation structure in neutron irradiated Zircaloy-2 studied by synchrotron x-ray diffraction peak profile analysis." Acta Materialia 126 (2017): 102-113.

[127] Ungár, T., et al. "The contrast factors of dislocations in cubic crystals: the dislocation model of strain anisotropy in practice." Journal of applied crystallography 32.5 (1999): 992-1002.

[128] Maloy, S. A., et al. "The mechanical properties of 316L/304L stainless steels, Alloy 718 and Mod 9Cr–1Mo after irradiation in a spallation environment." Journal of Nuclear Materials 296.1 (2001): 119-128.

[129] Pokor, C., et al. "Irradiation damage in 304 and 316 stainless steels: experimental investigation and modeling. Part II: Irradiation induced hardening." Journal of nuclear materials 326.1 (2004): 30-37.

[130] Hosemann, Peter. "Small-scale mechanical testing on nuclear materials: bridging the experimental length-scale gap." Scripta Materialia (2017).

[131] Long, B., Y. Dai, and N. Baluc. "Investigation of liquid LBE embrittlement effects on irradiated ferritic/martensitic steels by slow-strain-rate tensile tests." Journal of Nuclear Materials 431.1 (2012): 85-90.

[132] Lei, Jing, et al. "Study on the mechanical properties evolution of A508-3 steel under proton irradiation." Nuclear Instruments and Methods in Physics Research Section B: Beam Interactions with Materials and Atoms 338 (2014): 13-18.

[133] Milot, Timothy Steven. Establishing Correlations for Predicting Tensile Properties Based on the Shear Punch Test and Vickers Microhardness Data. Thesis. 2013. Print.

[134] Valiev, Ruslan Z., and Terence G. Langdon. "Principles of equal-channel angular pressing as a processing tool for grain refinement." Progress in materials science 51.7 (2006): 881-981.

[135] Bentley, James, and D. T. Hoelzer. "TEM characterization of tensile-tested 14YWT nanostructured ferritic alloys." Microscopy and Microanalysis 14.S2 (2008): 1416.

[136] He, Jianchao, et al. "Stability of nanoclusters in 14YWT oxide dispersion strengthened steel under heavy ion-irradiation by atom probe tomography." *Journal of Nuclear Materials* 455.1 (2014): 41-45.

[137] Hysitron Inc. "xSol High Temperature Stage. https://www.hysitron.com/media/1575/xsol800ou-r1f.pdf.

[138] Hangen, Ude, Chun-Liang Chen, and Asta Richter. "Mechanical Characterization of PM2000 Oxide-Dispersion-Strengthened Alloy by High Temperature Nanoindentation." *Advanced Engineering Materials* 17, no. 11 (2015): 1683-1690.

[139] Schoeppner, R. L., N. Abdolrahim, I. Salehinia, H. M. Zbib, and D. F. Bahr. "Elevated temperature dependence of hardness in tri-metallic nano-scale metallic multilayer systems." *Thin Solid Films* 571 (2014): 247-252.

[140] Cheng, Eric Jianfeng, Ying Li, Jeff Sakamoto, Shaobo Han, Haiping Sun, Jacob Noble, Hirokazu Katsui, and Takashi Goto. "Mechanical properties of individual phases of ZrB 2-ZrC eutectic composite measured by nanoindentation." *Journal of the European Ceramic Society* (2017).

[141] Broitman, Esteban, Lina Tengdelius, Ude D. Hangen, Jun Lu, Lars Hultman, and Hans Högberg. "High-temperature nanoindentation of epitaxial ZrB 2 thin films." *Scripta Materialia* 124 (2016): 117-120.

[142] Vanstreels, Kris, Houman Zahedmanesh, and Ude Hangen. "Thermal expansion coefficients of ultralow-k dielectric films by cube corner indentation tests at elevated temperatures." *Applied Physics Letters* 107, no. 23 (2015): 233101.

[143] Special Metals "The story of the "INCOLOY® alloys series, from 800 through 800H, 800HT®." http://www.specialmetals.com/assets/smc/documents/alloys/incoloy/incoloy-alloys-800h-800ht.pdf.

[144] Flom, Donald G., and Ranga Komanduri. "Some indentation and sliding experiments on single crystal and polycrystalline materials." *Wear* 252, no. 5 (2002): 401-429.

[145] Bouvier, S., and A. Needleman. "Effect of the number and orientation of active slip systems on plane strain single crystal indentation." *Modelling and Simulation in Materials Science and Engineering* 14, no. 7 (2006): 1105.

[146] Backes, B., Y. Y. Huang, M. Göken, and K. Durst. "The correlation between the internal material length scale and the microstructure in nanoindentation experiments and simulations using the conventional mechanism-based strain gradient plasticity theory." *journal of Materials Research* 24, no. 3 (2009): 1197-1207.

[147] Kreuzer, H. G. M., and R. Pippan. "Discrete dislocation simulation of nanoindentation: indentation size effect and the influence of slip band orientation." *Acta materialia* 55, no. 9 (2007): 3229-3235.

[148] Lucas, G. E. "The evolution of mechanical property change in irradiated austenitic stainless steels." *Journal of Nuclear Materials* 206, no. 2-3 (1993): 287-305.

[149] Busby, Jeremy T., M. C. Hash, and G. S. Was. "The relationship between hardness and yield stress in irradiated austenitic and ferritic steels." *Journal of Nuclear Materials* 336, no. 2 (2005): 267-278.

[150] Prasitthipayong, A., D. Frazer, A. Kareer, M.D. Abad, A. Garner, B. Joni, T. Ungar, G. Ribarik, M. Preuss, L. Balogh, S.J. Tumey, A.M. Minor and P. Hosemann. “Micro mechanical testing of candidate structural alloys for Gen-IV nuclear reactors” (Submitted).

[151] Backes, Bjoern, K. Durst, and M. Goeken. "Determination of plastic properties of polycrystalline metallic materials by nanoindentation: Experiments and finite element simulations." *Philosophical Magazine* 86, no. 33-35 (2006): 5541-5551.

[152] Kiener, D., P. Hosemann, S. A. Maloy, and A. M. Minor. "In situ nano-compression testing of irradiated copper." *Nature materials* 10, no. 8 (2011): 608.

[153] Durst, K., O. Franke, A. Böhner, and M. Göken. "Indentation size effect in Ni–Fe solid solutions." *Acta materialia* 55, no. 20 (2007): 6825-6833.

[154] Weaver, Jordan S., Siddhartha Pathak, Ashley Reichardt, Hi T. Vo, Stuart A. Maloy, Peter Hosemann, and Nathan A. Mara. "Spherical nanoindentation of proton irradiated 304 stainless steel: A comparison of small scale mechanical test techniques for measuring irradiation hardening." *Journal of Nuclear Materials* 493 (2017): 368-379.

[155] Jiao, Z., and G. S. Was. "Impact of localized deformation on IASCC in austenitic stainless steels." *Journal of Nuclear Materials* 408, no. 3 (2011): 246-256.

[156] McMurtrey, M. D., G. S. Was, B. Cui, I. Robertson, L. Smith, and D. Farkas. "Strain localization at dislocation channel–grain boundary intersections in irradiated stainless steel." *International Journal of Plasticity* 56 (2014): 219-231.

[157] Abad, Oscar Torrents, Jeffrey M. Wheeler, Johann Michler, Andreas S. Schneider, and Eduard Arzt. "Temperature-dependent size effects on the strength of Ta and W micropillars." *Acta Materialia* 103 (2016): 483-494.

[158] Frick, C. P., B. G. Clark, S. Orso, A. S. Schneider, and E. Arzt. "Size effect on strength and strain hardening of small-scale [111] nickel compression pillars." Materials Science and Engineering: A489, no. 1 (2008): 319-329.

[159] Ramos, Kyle J., Daniel E. Hooks, and David F. Bahr. "Direct observation of plasticity and quantitative hardness measurements in single crystal cyclotrimethylene trinitramine by nanoindentation." *Philosophical Magazine* 89, no. 27 (2009): 2381-2402.

[160] Raabe, D., D. Ma, and F. Roters. "Effects of initial orientation, sample geometry and friction on anisotropy and crystallographic orientation changes in single crystal microcompression deformation: A crystal plasticity finite element study." Acta Materialia 55, no. 13 (2007): 4567-4583.

[161] Reichardt, A., A. Lupinacci, D. Frazer, N. Bailey, H. Vo, C. Howard, Z. Jiao, A. M. Minor, P. Chou, and P. Hosemann. "Nanoindentation and in situ microcompression in different dose regimes of proton beam irradiated 304 SS." *Journal of Nuclear Materials* 486 (2017): 323-331.

[162] Minor, Andrew M., SA Syed Asif, Zhiwei Shan, Eric A. Stach, Edward Cyrankowski, Thomas J. Wyrobek, and Oden L. Warren. "A new view of the onset of plasticity during the nanoindentation of aluminium." Nature materials 5, no. 9 (2006): 697-702.

[163] Klingshirn, Claus, Johannes Fallert, Huijuan Zhou, and Heinz Kalt. "Comment on “Excitonic ultraviolett lasing in ZnO-based light emitting devices” Appl. Phys. Lett. 90, 131115 (2007)]." Applied Physics Letters (2007).

[164] Was, Gary S., and Peter L. Andresen. "Irradiation-assisted stress-corrosion cracking in austenitic alloys." JOM Journal of the Minerals, Metals and Materials Society 44, no. 4 (1992): 8-13.

[165] Byun, Thak Sang, and Naoyuki Hashimoto. "Strain hardening and long-range internal stress in the localized deformation of irradiated polycrystalline metals." Journal of nuclear materials 354, no. 1 (2006): 123-130.

[166] Soler, Rafael, Jeffrey M. Wheeler, Hyung-Jun Chang, Javier Segurado, Johann Michler, Javier Llorca, and Jon M. Molina-Aldareguia. "Understanding size effects on the strength of single crystals through high-temperature micropillar compression." *Acta Materialia* 81 (2014): 50-57.

[167] Rao, Satish I., D. M. Dimiduk, Triplicane A. Parthasarathy, M. D. Uchic, Meijie Tang, and Chris Woodward. "Athermal mechanisms of size-dependent crystal flow gleaned from three-dimensional discrete dislocation simulations." *Acta Materialia* 56, no. 13 (2008): 3245-3259.

[168] Wheeler, Jeffrey M., Christoph Kirchlechner, Jean-Sébastien Micha, Johann Michler, and Daniel Kiener. "The effect of size on the strength of FCC metals at elevated temperatures: annealed copper." *Philosophical Magazine* 96, no. 32-34 (2016): 3379-3395.

[169] Yabuuchi, Kiyohiro. 'Flash Polishing'. 2015. Presentation.